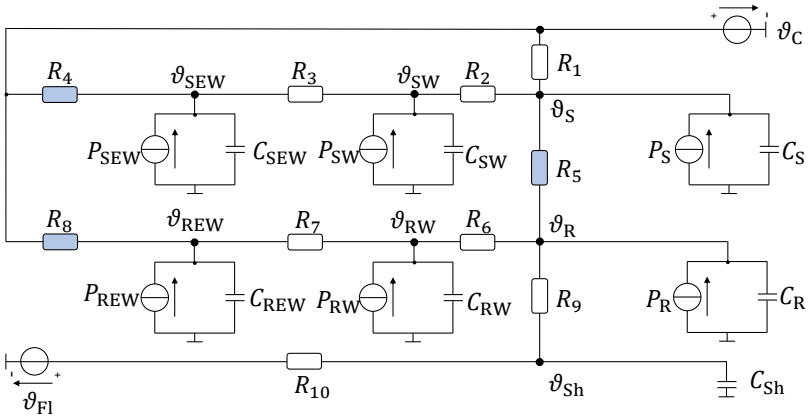
Eryang Wang

Model-based Temperature Monitoring and Thermal Management of Electrically Excited Synchronous Motors



Karlsruhe Institute of Technology

Elektrotechnisches Institut

Model-based Temperature Monitoring and Thermal Management of Electrically Excited Synchronous Motors

Zur Erlangung des akademischen Grades eines

DOKTORS DER INGENIEURWISSENSCHAFTEN (Dr.-Ing.)

von der KIT-Fakultät für Elektrotechnik und Informationstechnik des
Karlsruher Instituts für Technologie (KIT)
angenommene

DISSERTATION

von

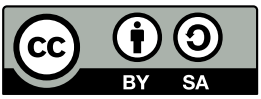
M.Sc. Eryang Wang
geboren in: Anhui, China

Tag der mündlichen Prüfung:	14.10.2026
Hauptreferent:	Prof. Dr.-Ing. Martin Doppelbauer
Korreferentin:	Prof. Dr.-Ing. Nejila Parspour (Universität Stuttgart)

Karlsruher Institut für Technologie (KIT)
Elektrotechnisches Institut (ETI)

Zur Erlangung des akademischen Grades eines Doktors der Ingenieurwissenschaften von der KIT-Fakultät für Elektrotechnik und Informationstechnik des Karlsruher Instituts für Technologie (KIT) angenommene Dissertation von M.Sc. Eryang Wang, geboren in Anhui, China

Tag der mündlichen Prüfung:	14.10.2026
Hauptreferent:	Prof. Dr.-Ing. Martin Doppelbauer
Korreferentin:	Prof. Dr.-Ing. Nejila Parspour (Universität Stuttgart)



This document - except for the figures 1.1, 2.1, 2.4, 2.5, 2.6, 2.7, 2.12, 2.13, 4.1, 4.2, 5.6, 6.1, 6.2, 6.3 - is licensed under a Creative Commons Attribution-ShareAlike 4.0 International License (CC BY-SA 4.0): https://creativecommons.org/licenses/by-sa/4.0/deed.en
DOI: 10.5445/IR/1000198358

Preface

This dissertation was completed during my time as a PhD student at Mahle. It is a collaboration PhD project between Mahle and ETI. The objective of this project was to develop a low-order temperature model for Electrically Excited Synchronous Motor (EESM), enabling real-time temperature monitoring to mitigate hot spot temperatures and effectively prevent motor overheating. This is an interesting topic, but it is also full of challenges. Therefore, I would like to express my sincere gratitude to all those who supported me throughout my PhD journey. Without your encouragement, assistance, and patience, this work would not have been possible.

First and foremost, I would like to thank Prof. Dr.-Ing Martin Doppelbauer for his continuous guidance and invaluable support. His advice and insight have significantly enhanced the quality of my research. Each discussion with him helped clarify and refine the direction of my work. Besides, his encouragement to attend both national and international conferences played a crucial role in broadening my academic perspective.

At Mahle, I am especially grateful to Dr. Philip Grabherr, Dr. Marco Warth and Dr. Peter Wieske for their expert supervision. Their constructive feedback, continuous support, and encouragement helped me navigate challenges and stay focused throughout my research.

Good ideas often come from effective exchanges. I am also thankful for the scientific exchanges with my colleagues at the institute, including Dr. Matthias Brodatzki, Dr. Jing Ou, Dr. Felix Hoffmann, Dr. Hongfei Lu and others. At Mahle, I would like to thank Dr. Christoph Schmuelling, Dr. Claas Kuerten, Leonard Lorenz, Michael Rehermann and many more who contributed to the progress of my work. Special thanks go to Juergen Mack and Carsten Koolmann for their support in setting up the test bench and measurement systems.

Last but not least, I wish to express my appreciation to my parents, my wife Yuan Zhou and our lovely son Philipp Zizhou Wang. Your support, patience and love gave me the strength to complete this dissertation.

7 October 2024 in Waiblingen
Eryang Wang

Kurzfassung

Der Aufstieg der Elektrofahrzeuge bringt sowohl Herausforderungen als auch Chancen für den Wandel der Automobilindustrie mit sich. In diesem Zusammenhang spielen elektrische Antriebe, elektronische Steuerungssysteme und Batterien eine zentrale Rolle. Diese Arbeit konzentriert sich auf die EESM als elektrisches Antriebssystem, mit besonderem Fokus auf die Online-Temperaturüberwachung und Strategien zum Thermomanagement. Die Forschung gliedert sich in drei Hauptteile.

Zunächst wird ein thermisches Netzwerkmodell niedriger Ordnung für die EESM entwickelt, in dem die Verlustmechanismen der Maschine sowie die thermischen Widerstände und Kapazitäten analytisch beschrieben werden. Zur Verbesserung der Modellgenauigkeit wird eine neuartige kombinierte statisch-dynamische Parameteridentifikation vorgestellt. In diesem Verfahren werden thermische Widerstände und Kapazitäten getrennt identifiziert, um gegenseitige Beeinflussungen während der Identifikation zu minimieren. Das resultierende thermische Modell wird anschließend experimentell durch Kreuzvalidierung verifiziert, was seine Effektivität bei der Abbildung des physikalischen Verhaltens der Maschine bestätigt.

Aufbauend auf dem Modell erfolgt eine systematische Analyse auf Systemebene, um die Stabilität und das dynamische Fehlerverhalten des thermischen Modells zu bewerten und einen Zustandsbeobachter zu integrieren. Das thermische Netzwerkmodell wird diskretisiert und in einen Kalman-Filter eingebunden. Dieser Beobachter verwendet die Temperatur der Stator-Wickelkopf sowie den Strom und die Spannung der Rotorwicklung zur Datenfusion. Die experimentellen Ergebnisse zeigen, dass das System beobachtbar ist und dass der Filter Messrauschen wirksam unterdrückt, wodurch eine zuverlässige Schätzung der inneren thermischen Zustände der Maschine ermöglicht wird.

Abschließend wird ein neues, modellbasiertes Thermomanagementkonzept auf Anwendungsebene vorgeschlagen. Im Gegensatz zu herkömmlichen Ansätzen

wie der Drehmomentbegrenzung zielt das vorgeschlagene Konzept darauf ab, die Temperaturen von Rotor und Stator aktiv auszugleichen. Als Kompromiss kann dies zu erhöhten Temperaturen in thermisch weniger kritischen Bereichen führen. Das Konzept wird durch Systemsimulationen validiert und zeigt ein verbessertes thermisches Verhalten sowie potenzielle Vorteile für die langfristige Zuverlässigkeit.

Abstract

The rise of electric vehicles has introduced both challenges and opportunities for the transformation of the automotive industry. In this context, electric drives, electronic control systems and batteries are essential. This work focuses on the EESM as the electric drive system, with particular attention to online temperature monitoring and thermal management strategies. The research is divided into three main parts.

Firstly, a low-order thermal network model is developed for the EESM, in which the machine's loss mechanisms, thermal resistances, and capacitances are analytically calculated. To improve model accuracy, a novel combined static-dynamic parameter identification approach is introduced. In this method, thermal resistances and capacities are identified separately to reduce mutual interference during the estimation process. The resulting thermal model is then validated through experimental cross-validation, confirming its effectiveness in representing the physical behavior of the machine.

Following model development, a system-level analysis is conducted to evaluate the thermal model's stability and dynamic error characteristics and to introduce state observer. The thermal network model is discretized and integrated into a Kalman filter. This observer utilizes the stator end-winding temperature and the rotor winding current and voltage as input for data fusion. Experimental results demonstrate that the system is observable and that the Kalman filter effectively reduces measurement noise, enabling reliable estimation of the machine's internal thermal states.

Finally, a new model- based thermal management concept is proposed on the application level. Differed from the conventional torque derating approaches as state of the art, the proposed concept seeks to actively balance the rotor and stator temperatures. As a trade-off, temperatures in thermally less critical regions may increase. The proposed control concept is validated through system-level

simulations, demonstrating improved thermal behavior and potential benefits for long-term reliability.

List of Symbols

Abbreviations

AC	Alternating Current
BEV	Battery Electric Vehicle
CFD	Computational Fluid Dynamics
DC	Direct Current
EESM	Electrically Excited Synchronous Motor
EV	Electric Vehicle
FEA	Finite Element Analysis
FOC	Field-Oriented Control
GaN	Gallium Nitride
ICE	Internal Combustion Engine
IGBT	Insulated Gate Bipolar Transistor
LPTN	Lumped Parameter Thermal Network
LPV	Linear Parameter-Varying Model
LSQ	Least Squares Method
LTI	Linear Time-Invariant System
LUT	Look-Up Table
MLC	Multilevel Converter
MPC	Model Predictive Control
MTPA	Maximum Torque Per Ampere
MTPV	Maximum Torque Per Voltage
PI	Proportional-Integral
PMSM	Permanent Magnet Synchronous Motor
PMTO	Permanet Magnet Temperature Observer
POPE	Position-Offset-based Parameter Estimation

PSO	Particle Swarm Optimization
PT1	First-order Lag
RNN	Recurrent Neural Network
RTS-95	Renault Test Standard 1995
SFTP-US06	US06 Supplemental FederalT Test Procedure
TEFC	Totally Enclosed Fan-Cooled
UKF	Unscented Kalman Filter
WLTP	Worldwide Harmonized Light Vehicles Test Procedure

Index of symbols

C_{d}	Air drag coefficient
A	Cross-sectional area of the component to transfer heat by conduction
F	Bearing load
B	Magnetic flux density
C_{REW}	Thermal capacity of rotor end winding
C_{RW}	Thermal capacity of rotor active winding
C_{R}	Thermal capacity of rotor iron
C_{SEW}	Thermal capacity of stator end winding
C_{SW}	Thermal capacity of stator active winding
C_{S}	Thermal capacity of stator iron
C_{Sh}	Thermal capacity of shaft
A_{c}	Vehicle corss section area
C	Thermal capacity
ε_{k}	Initial deviation
F_{a}	Motor traction force
F_{d}	Air drag force
F_{g}	Gravity force
F_{g}	Geometry factor of the airgap
F_{r}	Rolling friction force
g	Gravity acceleration
H	Magnetizing force
$\underline{I}$	Current space vector
γ	Road inclination angle

I	Effective value of current
J_{d}	Deviation indicator in the dynamic global parameter identification
J_{s}	Deviation indicator in the static global parameter identification
λ_{a}	Thermal conduction coefficient (axial)
λ_{r}	Thermal conduction coefficient (radial)
λ_{a}	Thermal conductivity of air gap
λ_{c}	Thermal conduction coefficient of conductor
λ_{p}	Thermal conduction coefficient of impregnation
$\lambda_{\mathrm{winding}}$	Equivalent thermal conduction coefficient of winding
L	Length of the cylinder
$i_{\mathrm{r,max}}$	Maximum rotor current
$i_{\mathrm{s,max}}$	Maximum stator phase current
$u_{\mathrm{s,max}}$	Maximum stator voltage
μ	Bearing friction coefficient
m_{k}	Measurement noise
p_{k}	Process noise
Nu	Nusselt number in the airgap
Ω	Angular rotor speed
P_{REW}	Power loss of rotor end winding
P_{SH}	Power loss of the shaft
P_{RW}	Power loss of rotor active winding
P_{R}	Power loss of rotor iron
P_{SEW}	Power loss of stator end winding
P_{SW}	Power loss of stator active winding
P_{S}	Power loss of stator iron
P_{loss}	Total motor losses
P_{rotor}	Total rotor losses
P_{stator}	Total stator losses
P_{bearing}	Bearing friction losses
P_{fe}	Iron losses
$P_{\mathrm{rotorwinding}}$	Copper losses of the rotor windings
$P_{\mathrm{statorwinding}}$	Copper losses of the stator windings
P_{windage}	Windage friction losses
P_{winding}	General winding losses
P	Power loss
Q_{rad}	Power of radiation

R_{10}	Thermal resistance between shaft and ambient
R_1	Thermal resistance between coolant and stator iron
R_2	Thermal resistance between stator iron and stator active winding
R_3	Thermal resistance between stator active winding and stator end winding
R_4	Thermal resistance between frame and stator end winding
R_5	Thermal resistance between stator iron and rotor iron
R_6	Thermal resistance between rotor iron and rotor active winding
R_7	Thermal resistance between rotor active winding and rotor end winding
R_8	Thermal resistance between rotor end winding and frame
R_9	Thermal resistance between rotor iron and shaft
υ_{rw}	Rotor active winding mass as a percentage of the whole rotor winding
υ_{rew}	Rotor end winding mass as a percentage of the whole rotor winding
R_{cond}	Equivalent thermal resistance of conduction
R_{conv}	Equivalent thermal resistance of convection
$R_{\mathrm{e,0}}$	Electrical resistance by the reference temperature
$R_{\mathrm{e,AC}}$	AC electrical resistance
$R_{\mathrm{e,DC}}$	DC electrical resistance
ϑ_1	Lower temperature in relay 1
ϑ_2	Upper temperature in relay 1
$R_{\mathrm{e,r}}$	Electrical resistance in the rotor winding
$R_{\mathrm{e,s}}$	Electrical phase resistance in the stator winding
R_{e}	General electrical resistance
u_{r}	Rotor voltage
β_{L}	Rotor angle posision
M_{dr}	Coupling inductance between the d-axis of the stator and rotor
Ψ_{r}	Rotor flux linkage
L_{r}	Rotor inductance
$R_{\mathrm{I,1a}}$	Axial thermal resistance from average temperature to the A side in the I-type thermal unit
$R_{\mathrm{I,1r}}$	Raidal thermal resistance from average temperature to the outer radius in the I-type thermal unit
$R_{\mathrm{I,2a}}$	Axial thermal resistance from average temperature to the B side in the I-type thermal unit

$R_{\mathrm{I,2r}}$	Raidal thermal resistance from average temperature to the inner radius in the I-type thermal unit
$R_{\mathrm{T,1a}}$	Axial thermal resistance from average temperature to the A side in the T-type thermal unit
$R_{\mathrm{T,1r}}$	Radial thermal resistance from average temperature to the outer radius in the T-type thermal unit
$R_{\mathrm{T,2a}}$	Axial thermal resistance from average temperature to the B side in the T-type thermal unit
$R_{\mathrm{T,2r}}$	Radial thermal resistance from average temperature to the inner radius in the T-type thermal unit
$R_{\mathrm{T,3a}}$	Axial interconnecting thermal resistance in the T-type thermal unit
$R_{\mathrm{T,3r}}$	Raidal theoretical interconnecting thermal resistance in the T-type thermal unit
R	Thermal resistance
σ	Stefan-Boltzmann constant
L_σ	Stator leakage inductance
Ψ_α	Stator flux linkage in αdirection
Ψ_{a}	Stator flux linkage in phase a direction
Ψ_β	Stator flux linkage in βdirection
Ψ_{b}	Stator flux linkage in phase b direction
Ψ_{c}	Stator flux linkage in phase c direction
Ψ_{d}	Stator flux linkage in the d axis
Ψ_{q}	Stator flux linkage in the q axis
L_{d}	Stator inductance in the d axis
L_{q}	Stator inductance in the q axis
L_{hd}	Stator main inductance in the d axis
L_{hq}	Stator main inductance in the q axis
A	system matrix of the thermal network state space representation
B	Input matrix of the thermal network state space representation
C_{s}	Output matrix of the thermal network during stational state
C_{t}	Output matrix of the thermal network during trasient state
C	Output matrix of the thermal network state space representation
D	Feedthrough matrix of the thermal network state space representation

K	Kalman gain
P	Covariance matrix of the estimated accuracy in the kalman filter
Q	Covariance matrix of the process noise in the kalman filter
R	Covariance matrix of the observation noise in the kalman filter
u	System input u of the thermal network state space representation
ϑ	State vaector in the thermal network state space representation
y	Output in the thermal network state space representation
Ta_{a}	Taylor number in the air gap
Φ	State-transition matrix
T	Torque
υ_{c}	Volume ratio of the conductors in the winding
ε	Material-specific emissivity
V	Volume
ρ_{a}	Air density
α	Copper temperature-depend coefficient
a	Inner radius of the air gap
b	Outer radius of the air gap
i_{α}	Current in the αaxis in the α-βcoordinate system
i_{β}	Current in the βaxis in the α-βcoordinate system
c	Specific thermal capacity
δ	Skin depth of the conductor
v_{diff}	Difference between the drive cycle speed and the vehicle speed
v_{ref}	Drive cycle speed
T_{ref}	Reference torque from the driver model block
r_{w}	Dynamic wheel radius
f	Electrical frequency
j	Vehicle gear ratio
h_{airgap}	Air gap heat convection transfer coefficient
$h_{\mathrm{endwinding}}$	End winding heat convection transfer coefficient
$\hat{i}_{\mathrm{s}}$	Peak value of the stator phase current
i_{d}	Stator current in d axis in the d/q coordinate system
i_{q}	Stator current in q axis in the d/q coordinate system
i_{r}	Current in the rotor winding
k_1	Curve fitting parameters for the end winding area
k_2	Curve fitting parameters for the end winding area
$k_{\mathrm{roughness}}$	Roughness coefficient
S	Sensitivity anaylsis varying factor

k	Time step k of the time-discrete system
k_{eddy}	Pre-factor of eddy current losses
k_{excess}	Pre-factor of excess losses
k_{h}	Pre-factor of hysteresis losses
k_{r}	Ratio of phase resistance in alternative and direct currents in the stator winding
w	Weighting factors for the LUT optimization
λ	Thermal conduction coefficient
l	Length of the component
T_{mot}	Required motor torque
m	Mass
n_{corner}	Motor corner speed
n_{max}	Maximal motor speed
n_{phase}	Number of phases
n	Motor speed
ω	Electrical angular frequency
p_{fe}	Specific iron losses
i_{a}	Current in phase a
i_{b}	Current in phase b
i_{c}	Current in phase c
u_{a}	Voltage in phase a
u_{b}	Voltage in phase b
u_{c}	Voltage in phase c
Q_{avg}	Average flowrate of the cooling water glycol
r_1	Outer radius of the cylinder
r_2	Inner radius of the cylinder
$r_{\text{m,a}}$	Mean annulus radius in the air gap
r_{m}	Average radius of the cylinder
C_{r}	Rolling friction coefficient
σ	Material conductivity
t_{s}	Sample time
t	Time
u_{d}	Voltage in d axis in the d/q coordinate system
u_{k}	d current coefficients for apporximation of iron losses
υ	Kinematic viscosity of the airgap
u_{q}	Voltage in q axis in the d/q coordinate system
u_0	Vacuum permeability

ϑ_0	Node referece temperature
ϑ_1	Outer surface temperature
ϑ_2	Inner surface temperature
ϑ_{air}	Ambient air temperature
$\vartheta_{\text{A,m}}$	Average temperature on the A side
ϑ_{A}	Ambient temperature
$\vartheta_{\text{B,m}}$	Average temperature on the B side
ϑ_{Fl}	Ambient flange temperature
ϑ_{REW}	Rotor end winding temperature
ϑ_{RW}	Rotor active winding temperature
ϑ_{R}	Rotor iron temperature
ϑ_{SEW}	Stator end winding temperature
ϑ_{SW}	Stator active winding temperature
ϑ_{Sh}	Shaft temperature
ϑ_{S}	Stator iron temperature
ϑ_{C}	Coolant temperature
ϑ_{m}	Node average temperature
ϑ_{s}	Steady-state temperature
ϑ_{t}	Transient temperature
ϑ	Themral network node temperature
m_{veh}	Vehicle mass
v_{veh}	Vehicle speed
v_{k}	q current coefficients for apporximation of iron losses
u_α	Voltage in the αaxis in the α-βcoordinate system
u_β	Voltage in the βaxis in the α-βcoordinate system
v_{ref}	Reference speed
w_{k}	Rotor current coefficients for apporximation of iron losses
z_{p}	Number of pol pairs

Contents

Preface i

Kurzfassung iii

Abstract v

List of Symbols vii

1 Introduction 1
- 1.1 Motivation . . . 1
- 1.2 State of the art . . . 3
- 1.3 Classification of this work to the state of the art . . . 7
- 1.4 Outline of the thesis . . . 7

2 Thermal modeling of EESM using Lumped Parameter Thermal Network (LPTN) approach 9
- 2.1 Fundamentals of thermal modeling in the electrical machines . . . 10
  - 2.1.1 Heat transfer theory . . . 10
  - 2.1.2 Losses in the electrical machine . . . 13
- 2.2 EESM thermal network based on LPTN method . . . 19
  - 2.2.1 Topology . . . 19
  - 2.2.2 Heat transfer modeling in EESM thermal network . . . 23
  - 2.2.3 Loss modeling in the EESM thermal network . . . 26
  - 2.2.4 Mathematical description of the EESM thermal network 32

3 Experimental setup and measurements 33
- 3.1 Test bench and reference motor . . . 33
- 3.2 Sensor locations and temperature measurements . . . 34

3.3 Thermal driving cycle tests 44

4 Model parameter identification and validation 47
4.1 Local and global identification of the LPV system 49
4.2 Combined static-dynamic identification 50
4.3 Training results 53
4.4 Thermal analysis with LPTN thermal network 55
4.5 Cross validation with thermal cycles 56

5 Kalman filter as online EESM thermal state observer 61
5.1 State space equations 62
5.2 Concepts of EESM thermal network as Kalman filter 65
5.2.1 Model errors analysis 65
5.2.2 Model discretization 72
5.2.3 Kalman filter introduction 74
5.2.4 EESM Kalman filter concepts and validations 76

6 Model-based thermal management for EESM 87
6.1 EESM control theory 88
6.1.1 Coordinate system transformation 88
6.1.2 EESM torque control 92
6.2 Thermal management for EESM to avoid overheating 93
6.2.1 Generation of currents LUTs with different weighting . . 94
6.2.2 Control strategy with integrated thermal network 96
6.3 Validation with system simulation 99
6.3.1 Validation results with SFTP-US06 drive cycle 103
6.3.2 Validation results with RTS-95 drive cycle 110

7 Summary and outlook 113
7.1 Summary 113
7.2 Outlook 114

A Appendix 117

List of Figures 123

List of Tables 127

Bibliography 129

Chapter 1

Introduction

1.1 Motivation

Due to the increasing levels of air pollution in urban areas and the rising greenhouse gas emissions, Internal Combustion Engine (ICE) vehicles are losing their dominance in the automotive market as a drive system. Conversely, the electrification of the automotive industry is gaining more attention [1]. The growing market preference for Electric Vehicle (EV) has driven the intensive research into electric motor technologies.
In Germany, a total of 1,342,013 new vehicles with alternative propulsion systems (electric vehicles, hybrid, fuel cell, gas) were registered in 2024, equivalent to 47.6% of the total vehicles [2]. Of these, 572,672 new vehicles, representing 20.3% of the total, were equipped with electric drives, comprising Battery Electric Vehicle (BEV), plug-in hybrids and fuel cell vehicles. To date, the Permanent Magnet Synchronous Motor (PMSM) has been the predominant motor type in EV drives, largely due to its high efficiency and power density [3]. For instance, in 2022, PMSM accounted for over 80% of the electric motor market for EV [2, 3].
However, PMSM present a critical drawback: their reliance on rare earth materials such as neodymium and dysprosium. These materials are not only costly but also sourced through environmentally harmful and geographically constrained supply chains [3]. Rare earth mining can lead to serious ecological issues, including soil acidification and contamination of groundwater through wastewater, as well as the generation of radioactive and heavy metal waste [3].

As a result of these concerns, the EESM, an alternative motor type for EV drives, is gaining increased attention. In EESM, magnetic fields are generated by rotor-side excitation windings rather than permanent magnets. Although promising, EESM pose distinct challenges. The limited installation space in EVs necessitates high power density, which introduces significant thermal constraints. The rotor-side current excitation inherently leads to additional copper losses compared to PMSM, resulting in reduced efficiency and elevated rotor temperatures. For automotive applications, it is essential to maintain motor operation within safe temperature thresholds, as overheating may lead to irreversible thermal damage, such as insulation degradation [4].

To address this concerns, reliable temperature monitoring and effective thermal management are crucial. Motor temperature monitoring generally falls into two categories: sensor-based and model-based approaches [5]. Sensor-based methods offer precise temperature monitoring at the measured points. However, the installation of sensors in some critical parts is technically complex and economically impractical, for example in the rotating rotor parts [E1, 6]. Moreover, sensor failure can lead to total failure of the monitoring system. Due to these limitations, model-based temperature estimation has received increasing attention in recent years [E1, 6–9].

Several challenges exist in model-based monitoring. Firstly, building an accurate thermal model that estimate the thermal behavior of the motor is challenging. With Finite Element Analysis (FEA) or Computational Fluid Dynamics (CFD) approaches, the temperature field of the electrical machine can be calculated and the hot spots can be identified. However, this type of model-based temperature monitoring is computationally intensive. For real-time applications, analytical thermal modeling is preferred due to its lower computational burden. Analytically derived thermal networks can simplify complex 3D geometries while preserving acceptable accuracy. These thermal networks can be classified according to their level of discretization (i.e., the number of nodes) into dark grey-box LPTN (2-5 nodes), light grey-box LPTN (5-15 nodes) and white-box LPTN (high number of nodes) [8]. For the white-box LPTN, the temperature field within the electrical machine can also, to a certain degree comparison to FEA, be calculated and represented. Commercial software, such as Motor-CAD, are already available. However, in terms of white-box LPTN, many model parameters only appear physically reasonable but are difficult to verify and accurately determine. While thermal capacitances can be partially estimated, the determination of thermal resistances remains highly challenging. Moreover, due to the large number of parameters involved, parameter identification becomes considerably difficult, as it requires a correspondingly large amount of experi-

mental data for training. The increased number of parameters introduces further uncertainty into the identification process, making the parameter identification of white-box LPTN difficult to achieve a unique parameter convergence. In contrast, for dark grey-box LPTN and light grey-box LPTN, the number of parameters is limited. Such models can be enhanced using parameter identification techniques, trained with empirical data from test benches. The balance between accurate estimation and complexity of the model structure is one of the key factors for the model-based temperature monitoring.
Another limitation in terms of model-based monitoring is that most thermal models assume fault-free motor operation. In real-world applications, motors may encounter abnormal conditions or develop faults, which model-based methods alone cannot detect without real-time feedback. To overcome this, integrating thermal networks with Kalman filters has been proposed [10, 11]. Kalman filters allow for dynamic state estimation, improving robustness to uncertainties and unmodeled behavior.
In this thesis, a thermal management concept using a thermal network was investigated via system-level simulation. As the state of the art, the EESM works with optimized global minimum losses. When operating temperatures approach critical limits, torque derating is applied to reduce thermal load. However, this approach does not consider the local temperature difference within the motor. For instance, the stator may remain relatively cool while the rotor overheats, or the opposite could occur. By studying an EESM equipped with water jacket cooling, it was found that a significant temperature gradient exists between the stator and rotor due to the high thermal resistance of the air gap. Accordingly, a new model-based thermal management was studied to actively balance the thermal state between the stator and the rotor parts. Instead of immediately derating when temperatures rise, the algorithm adjusts operating conditions to equalize the thermal load between the rotor and stator. This strategy better exploits the EESM's thermal capacity and delays or even avoids performance-reducing torque derating.

1.2 State of the art

Research on thermal network modeling of electrical machines can be traced back to the 1950s. This section summarizes key developments in thermal modeling, the use of thermal models as temperature observers, and model-based thermal management strategies.

In the 1950s, Kotnik [12] proposed the concept of an equivalent thermal circuit with eight nodes for induction motors. The losses in each node and the thermal resistances between them were calculated analytically. However, the absence of thermal capacitances meant that only steady-state temperatures could be computed. In 1991, Mellor [13] advanced the field by proposing a LPTN for a Totally Enclosed Fan-Cooled (TEFC) motor. This model was capable of estimating both steady-state and transient temperatures. Notably, Mellor was among the first to suggest using thermal networks for real-time temperature estimation, enabling motor protection and duty-cycle evaluation [14].
In the 2000s, Boglietti [15] proposed a simplified thermal model for induction motors. He provided detailed methods for calculating essential thermal resistances, such as across the air-gap or between end windings and internal air. Additionally, he simplified Mellor's method for conduction resistance calculation, improving the efficiency and clarity of thermal network structures. During this time, several researchers have made significant contributions to addressing specific challenges in motor thermal modeling. Staton [16] introduced a layered winding model to better represent the thermal behavior of windings in the stator slot. Schubert [17] investigated heat transfer coefficients at the end winding and bearing covers of asynchronous machines.
Current research on LPTN modeling is divided in two primary directions. One focuses on high-resolution thermal models that capture the full temperature field of the motor. These models typically contain a large number of thermal nodes, making them computationally intensive. The other direction emphasizes simplified models for real-time applications, with fewer nodes and lower computational complexity. Based on the level of abstraction and node number, LPTN are generally classified into three categories [8, 18]:

- Dark grey-box LPTN (2-5 nodes): These models are highly abstract, incorporating only dominant heat transfer paths. They require minimal knowledge of physical heat transfer mechanisms, with most parameters identified through experimental data [8, 9, 19–25]. For instance, Huber [19] developed a low-order thermal network with critical thermal parameters stored in a Look-Up Table (LUT). Boseniuk [24] identified key thermal resistances in a PMSM using test bench measurements. Feng [9] and Wallscheid [8] also proposed low-order thermal networks for online temperature estimation, combining empirical formulas and parameter identification.

- Light grey-box LPTN (5-15 nodes): These models balance simplicity and accuracy. Initial parameters are derived from motor geometry and material

properties, then refined using experimental data [1, E1, 13, 26–32]. Epskamp [1] used this approach to assess motor performance under different cooling conditions. Kipp [31] applied RC circuit principles to develop a theoretical thermal model for permanent magnet motors. Sciascera [32] showed a seven-node thermal network of the PMSM, mainly aiming to estimate the winding temperatures. Based on this seven-node thermal network, she further simplified it to a three-node thermal network for faster calculation.

- White-Box LPTN (high number of nodes): These models are derived entirely from detailed motor geometry and material characteristics. They offer high-resolution temperature field estimation, including hot-spot detection. However, they are difficult to parameterize and computationally expensive [33–40]. Qi [37] used a space-resolved LPTN for automated thermal model generation. Gronwald [38] evaluated cooling concepts during the early motor design phase. Oechslen [39] applied white-box models to analyze high-performance machines. Hoffmann [40] applied white-box LPTN approach to model a PMSM with shaft-side oil spray cooling.

Beyond traditional LPTNs, other thermal modeling technologies have been investigated. Kirchgaessner [6] applied Recurrent Neural Network (RNN) trained with experimental data. Zhu [41] used the genetic programming to predict hot spots in railway traction transformers. Liang [42] combined LPTNs with analytical solutions of Poisson's equation for slot winding hot-spot estimation. The start-up company Newtwen [43] introduced a software toolbox that automatically converts CAD models into reduced-order thermal networks.
Besides evaluating the model accuracy, its application in observer design is currently under investigation. Kalman filter integration has enhanced the robustness of thermal estimation and failure detection. Schumann [44] applied an Unscented Kalman Filter (UKF) to estimate temperatures of a fluid-cooled automotive Insulated Gate Bipolar Transistor (IGBT). Phuc [45] used a dual Kalman filter referencing stator winding temperatures to estimate rotor temperatures. Saheba [10] and Wallscheid [11] implemented Kalman filters using measured stator or frame temperatures to improve model accuracy. Zhu [18] also implemented an Kalman Filter, with an integrated thermal network, aiming to estimate the motor temperature online.
Estimated temperatures can be used for thermal management. Conventional approaches rely on pre-defined thermal limits based on input current [47]. Some derating strategies adjust torque based on overload current, speed, and Direct Current (DC) link voltage [46], as shown in Fig. 1.1. In this approach, the

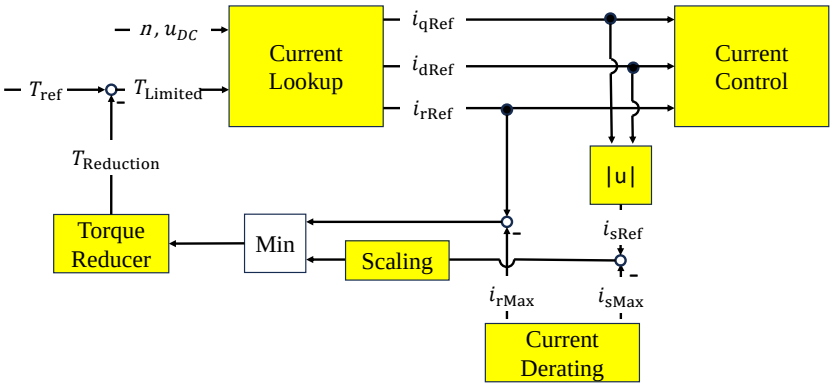


Figure 1.1: State of the art about torque derating [46]

reduced torque was used depending on the overload torque, the motor speed and the DC link voltage by overloading. Microprocessor-based thermal relays have been proposed to shut down motors when critical temperatures are reached [48]. While effective in avoiding overheating, such shutdowns can be problematic during emergencies where limited torque is still needed, such as moving a vehicle to a safe location. Notably, these approaches ignore the influence of the current motor temperatures: as highlighted by Qi [37], a motor operating at a lower temperature ("cold") has more performance potential than one already near its thermal limit ("hot"). To address, Qi [37] proposed Model Predictive Control (MPC) with integrated thermal networks to enable proactive derating and prevent full shutdown. He also introduced overload control strategies based on thermal capacity utilization for induction motors [49]. Lemmens [50] enhanced PMSM performance by dynamically adjusting switching frequency and current limits based on thermal feedback. Wallscheid [51] applied MPC for motor derating, validating the method through vehicle simulation studies.

1.3 Classification of this work to the state of the art

Based on the literature on thermal network modeling presented in Section 1.2, the author observed that parameter identification is essential for low-order thermal network. In state-of-the-art approaches, thermal resistances and thermal capacities are typically identified together using temperature measurements obtained from the test bench. In this thesis, a novel combined static–dynamic global identification approach is proposed, which allows the thermal resistances and capacitances to be identified separately [E1]. This separation effectively reduces mutual interference during the identification process and improves parameter estimation quality. The accuracy of the resulting thermal model has been validated using experimental data.
With reference to the thermal observer studies discussed in Section 1.2, it is noted that existing thermal observers are primarily applied to PMSMs, and the stator end-winding temperature is most commonly used as the reference input. In this thesis, a new thermal observer concept is proposed for EESMs, which integrates temperature signals from both the stator and rotor sides [E2]. The proposed observer demonstrates improved observability and filtering performance, as verified by experimental results.
Regarding thermal management strategies reviewed in Section 1.2, it is found that traditional approaches typically reduce motor temperature under thermally critical conditions via torque derating. In this thesis, a new model-based thermal management strategy is introduced, which reduces local hot spot temperatures by actively balancing the thermal load between more and less critical motor components [E3]. The proposed control algorithm has been validated through system-level simulations. It should be emphasized that while the proposed strategy does not eliminate the need for torque derating under continuous overloading, it significantly delays or even prevents derating during transient overload conditions by mitigating hot spot temperatures. This enables improved motor performance and thermal utilization.

1.4 Outline of the thesis

The overall structure of this thesis is outlined in Fig. 1.2. The main content is organized into three research levels: the component level, the system level and the application level.

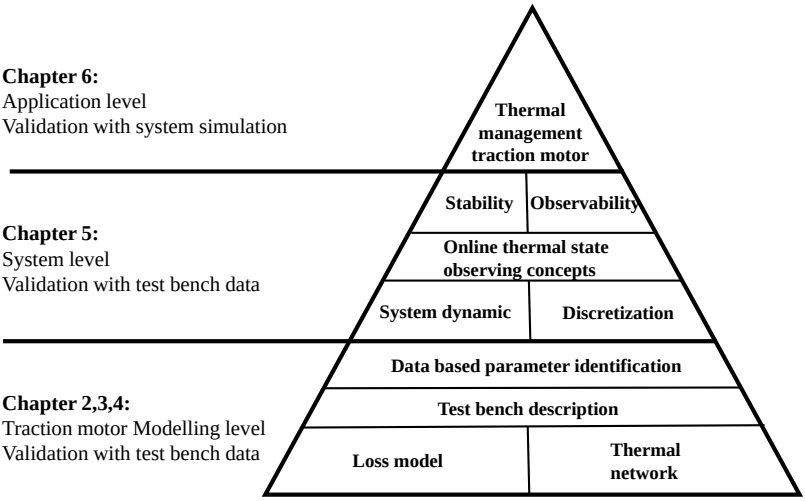


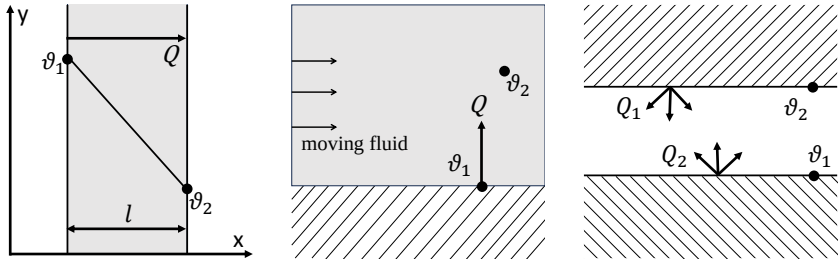
Figure 1.2: Outline of the thesis

At the component level, the focus lies on developing a low-order thermal network model for the EESM. This includes the modeling of loss model and the thermal network model. Using experimental data obtained from a test bench, parameter identification techniques are employed to optimize the estimated thermal model. The final thermal network model is validated through cross-validation against measured data.
At the system level, the dynamic behavior of the thermal network model is analyzed. This includes the evaluation of model stability and error dynamics. Subsequently, the model is discretized from time-continuous model to time-discrete model, enabling its integration into thermal state observers. Based on the discretized model, two Kalman filter-based observer concepts are investigated in detail for thermal state estimation.
At the application level, a novel thermal management strategy is proposed using the developed thermal model. This strategy aims to actively balance the temperature between thermally critical and non-critical regions of the motor. As a result, local hot spot temperatures can be effectively reduced, enhancing thermal utilization and overall motor performance.

Chapter 2

Thermal modeling of EESM using LPTN approach

In general, two principal approaches are employed for thermal modeling of electrical machines: FEA and analytical methods [7]. While FEA offers high accuracy in estimating temperature distributions and enables detailed visualization of the motor's temperature field [52], it necessitates a greater computational burden, resulting in a longer calculation time. Given the constraints on the computational capacity of the microprocessor, the analytical approach is the preferred method for online temperature estimation. Among the analytical approaches, the LPTN method is recognized as a typical one for thermal modeling of electrical machines. In the framework of LPTN, the motor is abstractly divided into a number of nodes. Each node represents the losses and the thermal capacities of the corresponding component. The thermal resistances between these nodes are analytically calculated in accordance with the motor's geometry, with the appropriate simplifications applied to balance model accuracy and complexity.
This chapter presents the thermal modeling of an EESM using the LPTN approach. First the fundamentals of heat transfer theory and the loss generation in electrical machines are introduced. Following this, an overview of the EESM thermal network and the corresponding simplifications is outlined. Based on the established theoretical fundamentals, the thermal resistances and heat losses within the EESM are then derived.



(a) Heat transfer in a solid or stationary fluid (conduction)

(b) Heat conduction from a surface to a moving fluid (convection)

(c) Heat transfer by radiation between two surfaces (radiation)

Figure 2.1: Types of heat transfer with ϑ_1 higher as ϑ_2 in each subfigures [53]

2.1 Fundamentals of thermal modeling in the electrical machines

Heat transfer and motor losses build the foundation of thermal modeling in electrical machines. This section introduces the basic principles of heat transfer theory and motor losses.

2.1.1 Heat transfer theory

Heat transfer can be divided into three main types: conduction, convection and radiation, as illustrated in Fig. 2.1.

Heat conduction

Heat conduction occurs as a result of a temperature gradient. Fig. 2.1 (a) illustrates an simplified solid flat, where heat flow is assumed to occur solely along the x-direction, thus forming a one-dimensional thermal model. Given that ϑ_1 on the left side of the thermal flat is higher than ϑ_2 on the right side, it follows that the heat Q flows from ϑ_1 towards ϑ_2. Under steady conditions, where the heat flow Q remains constant over time, the temperature distribution reaches a stationary state. The one-dimensional steady-state heat conduction is given by:

$$\lambda \cdot \frac{\partial^2 \vartheta}{\partial x^2} = 0 \tag{2.1}$$

where λ represents the thermal conductivity of the material. $\partial\vartheta$ denotes the infinite temperature along the x-axis, while ∂x denotes the infinite distance along the solid flat, as illustrated in Fig. 2.1 (a). With appropriate boundary conditions, (2.1) can be solved as:

$$\vartheta_x = \frac{\vartheta_2 - \vartheta_1}{l} \cdot x + \vartheta_1 \tag{2.2}$$

where x represents the position along the heat path, and ϑ_x denotes the corresponding local temperature. This results in a linear temperature gradient, as illustrated in Fig. 2.1 (a). The thermal resistance of conduction is given by:

$$R_{\text{cond}} = \frac{l}{\lambda \cdot A} \tag{2.3}$$

where l is the thickness of the solid flat, A is the cross-sectional, and λ is the thermal conductivity of the solid flat.

Heat convection

As illustrated in Fig. 2.1 (b), the transfer of heat between a solid wall and a flowing fluid occurs via convection. Given that the temperature ϑ_1 at the surface of the solid wall is higher than the temperature ϑ_2 of the moving fluid, the heat flows from the solid wall to the moving fluid. The most significant impact of convection is the temperature gradient between the solid wall and the flowing fluid, as well as the boundary layer of the fluid, which is influenced by the flow speed [53]. Convection can be further subdivided into free convection and forced convection. In free convection, the flow is driven by a temperature gradient and the associated density differences in the fluid. In contrast, forced convection is driven by an external pressure difference. The equivalent thermal resistance of convection R_{conv} is defined as:

$$R_{\text{conv}} = \frac{1}{h \cdot A} \tag{2.4}$$

where A is the contact area and h represents the film coefficient. The film coefficient h depends on the fluid velocity, fluid properties, and surface roughness [37]. Depending on the specific application and the degree of simplification involved,

the estimation approaches for the film coefficient h can be analytical, empirical or obtained directly from the measurements.

Heat radiation

Radiative heat transfer occurs via electromagnetic waves and does not require a material medium [53]. As illustrated in Fig. 2.1 (c), two solid walls with temperatures ϑ_1 and ϑ_2 are positioned between two vacuum spaces, with no material carrier present. Both walls transfer heat, designated as Q_1 and Q_2, to each other. According to the Stefan-Boltzmann law, radiative heat transfer can be calculated as [37]:

$$Q_{\text{rad}} = \sigma \cdot \varepsilon \cdot A(\vartheta_2^4 - \vartheta_1^4) \tag{2.5}$$

where ε represents the material-specific emissivity, A denotes the effective radiation surface area between the two solid components. σ is defined as Stefan-Boltzmann constant as:

$$\sigma = (5.6696 \pm 0.0075) \cdot 10^{-8} W \cdot m^{-2} \cdot K^{-4} \tag{2.6}$$

Due to the small magnitude of σ, radiation is typically negligible at low temperature differences but becomes significant when the temperature gradient is large.

Combination of heat transfer

In practical applications, heat transfer generally involves a combination of conduction, convection and radiation. Depending on the application and operating conditions, one or more of these mechanisms may be neglected without significant loss of accuracy [53]. Fig. 2.2 shows the heat transfer paths in the cross section of the in this work studied EESM. Heat generated in the iron core and copper windings is dissipated through different regions using various mechanisms. For example, between the motor frame and the ambient, heat is transferred by both conduction and radiation. However, literature suggests that radiation from the motor frame is only significant in natural convection-cooled systems [37, 54]. Since the motor under study uses water-jacket cooling, radiative heat transfer can be neglected.

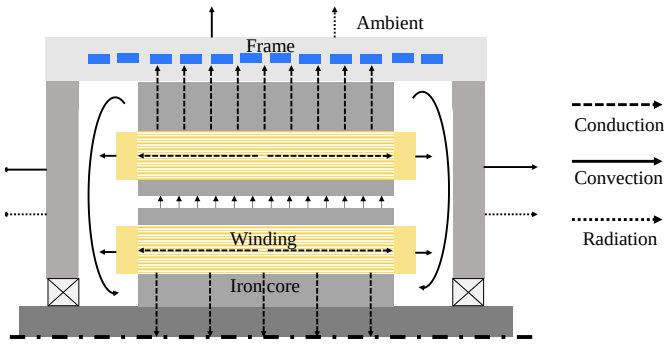


Figure 2.2: Major heat transfers in the EESM cross section

2.1.2 Losses in the electrical machine

In addition to heat transfer theory, motor losses are also a fundamental component of thermal modeling in electrical machines. The main types of power losses include the following categories [55].

- Resistive losses
- Iron losses
- Additional losses
- Mechanical losses

Fig. 2.3 illustrates the typical distribution of losses of the EESM. On the stator side, there are resistive losses $P_{\text{cu,s}}$ and iron losses $P_{\text{fe,s}}$. Within the air-gap, there are windage losses P_{windage} due to friction between the air and the outer contour of the rotor. On the rotor side, there are resistive losses $P_{\text{cu,r}}$ and iron losses $P_{\text{fe,r}}$. Additionally, bearing friction contributes to losses P_{bearing} at the shaft interface. The following subsections introduce these loss mechanisms in detail.

Resistive losses

Resistive (copper) losses in the windings are calculated as:

$$\begin{aligned} P_{\text{winding}} &= n_{\text{phase}} \cdot I^2 \cdot R_{\text{e,AC}} \\ R_{\text{e,AC}} &= R_{\text{e,DC}} \cdot k_{\text{r}} \end{aligned} \tag{2.7}$$

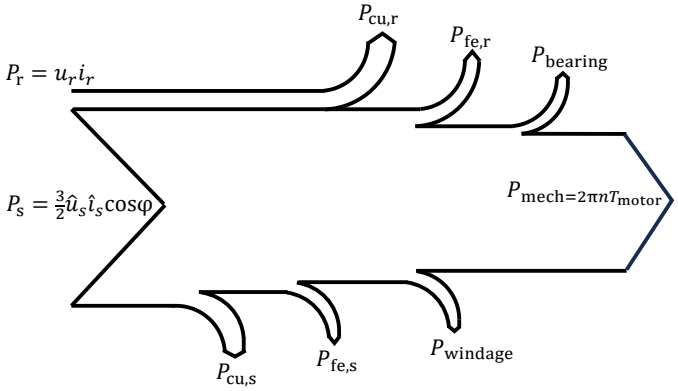


Figure 2.3: Schematic loss diagram for EESM

where n_{phase} is the number of phases, I is the effective current, $R_{\text{e,AC}}$ is the Alternating Current (AC) resistance and $R_{\text{e,DC}}$ is the DC resistance. The pre-factor k_{r} takes into account the influence of skin and proximity effect of the winding [55, 56]. The phenomenon of the skin and proximity effect is explained below with a simplified scenario.

Skin Effect

Fig. 2.4 shows the current distribution in a 2 mm-radius round conductor under different frequencies (50 Hz to 100 Hz). As the current frequency increases, current increasingly concentrates at the surface, forming a non-uniform distribution. At 100 kHz current is almost entirely at the outer edge (red region), with negligible density at the center (blue region). Fig. 2.4(b) is the quantitative demonstration of the current distribution at different frequencies. At 50 Hz, the current density along the radius of the conductor remains almost the same, indicating that the influence of the skin effect is low. In contrast, at 100 kHz, the current density along the radius of the conductor increases over-proportionally, indicating a strong influence of the skin effect. For quantitative estimation of the

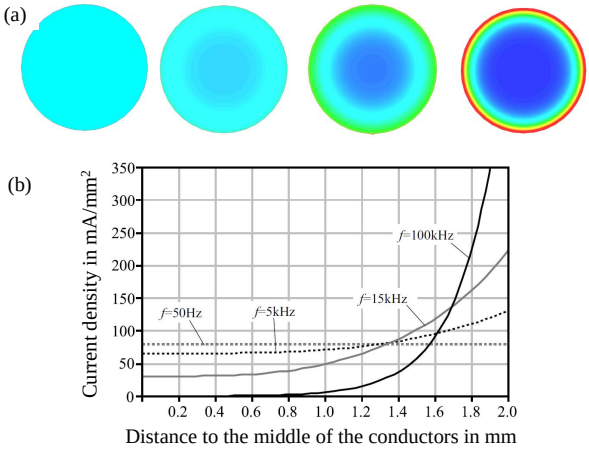


Figure 2.4: Current distribution under skin effect [57]

skin effect, the following equation is used to calculate the equivalent skin depth of the conductor under skin effect [57]:

$$\sigma = \frac{1}{\sqrt{\pi u_0 \delta f}} \tag{2.8}$$

where u_0 is vacuum permeability, δ is the material conductivity, and f is the current frequency.

Proximity Effect

Fig. 2.5 shows the current distribution under the influence of the proximity effect. The conductor is a round copper conductor with a radius of 2 mm. The conductor is in an alternating magnetic field, coming from the adjacent conductors on either side at a distance of 5 mm. It is worth mentioning that the adjacent conductors are not shown in the figure. The current following in the adjacent conductors varies from 50 Hz to 100 Hz. It can be seen qualitatively in Fig. 2.5(a) and quantitatively in Fig. 2.5(b), that the current density at the edge of the conductor increases rapidly with the increasing current frequency. Unlike the skin effect in Fig. 2.4, where the high current density area is a circular distribution along the edge of

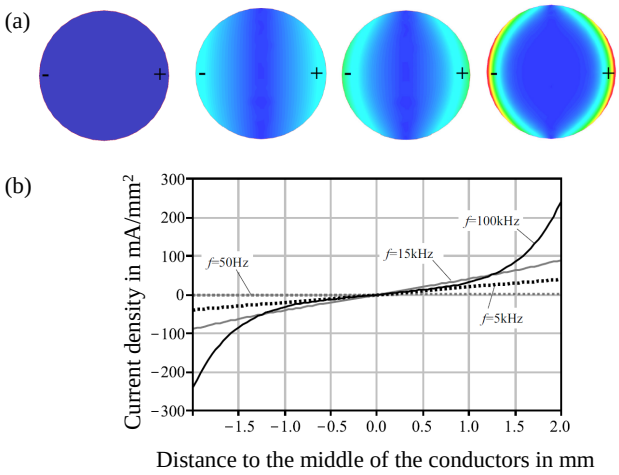


Figure 2.5: Current distribution under proximity effect [57]

the conductor, the high current density area of the conductor under the proximity effect is only on the right and left edges of the conductor.

Iron losses

In addition to copper losses, iron losses are another major losses in electrical machines. (2.9), known as the Bertotti equation, shows the different components of the iron losses:

$$p_{\mathrm{fe}} = \underbrace{k_{\mathrm{h}} \cdot f \cdot B^2}_{\text{hysteresis loss}} + \underbrace{k_{\mathrm{eddy}} \cdot f^2 \cdot B^2}_{\text{eddy current loss}} + \underbrace{k_{\mathrm{excess}} \cdot f^{1.5} \cdot B^{1.5}}_{\text{excess loss}} \tag{2.9}$$

In (2.9), the first term is the hysteresis loss, the second term is the eddy current loss and the third term is the excess loss. The hysteresis losses are due to the hysteresis phenomenon of the ferromagnetic materials as stator and rotor iron core. Fig. 2.6 shows the hysteresis curves of the electrical sheets M800-65A and M460-65A. With the alternating magnetizing force H, the magnetic flux density B shows the phenomenon of hysteresis with the coercivity. The hysteresis leads

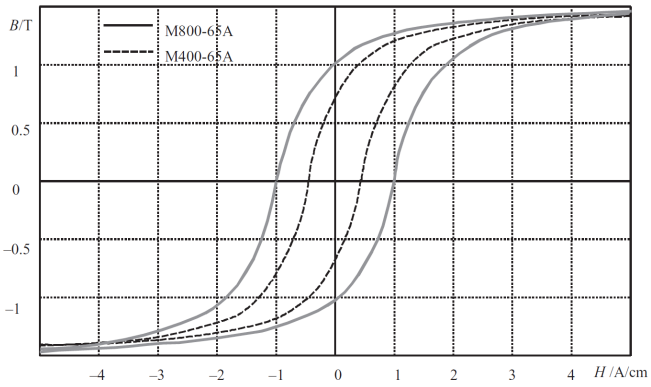


Figure 2.6: Approximate hysteresis curves of electrical sheets of M400-65A and M800-65A from Surahammars Bruk AB [55]

to the hysteresis losses as heat generation in the electrical machines. The hysteresis losses are linearly proportional to the frequency and increase with the square of the magnetic flux density. Together with the pre-factor k_{h}, the hysteresis losses can be calculated as $k_{\mathrm{h}} \cdot f \cdot B^2$ in (2.9).
The eddy current losses are related to the eddy current flowing through the electrical sheet. Fig. 2.7 shows a section of an electrical sheet under an alternating magnetic flied of flux density B. According to Faraday's law of electromagnetic induction, eddy current is induced in the electrical sheet. In Fig. 2.7, the eddy current flows across the cross-section of the electrical sheet. The eddy current losses are proportional to the square of the frequency and also proportional to the square of the magnetic flux density. With the pre-factor k_{eddy}, the eddy current losses can be estimated as $k_{\mathrm{eddy}} \cdot f^2 \cdot B^2$ in (2.9).
The excess losses in the Bertotti equation are caused by the internal movement of the domain walls between different magnetic domains [58]. The excess losses are used to improve the representation of the physical processes within the electrical steel under an alternating magnetic field [58]. With the pre-factor k_{excess}, the eddy current losses can be estimated as $k_{\mathrm{excess}} \cdot f^{1.5} \cdot B^{1.5}$ in (2.9).

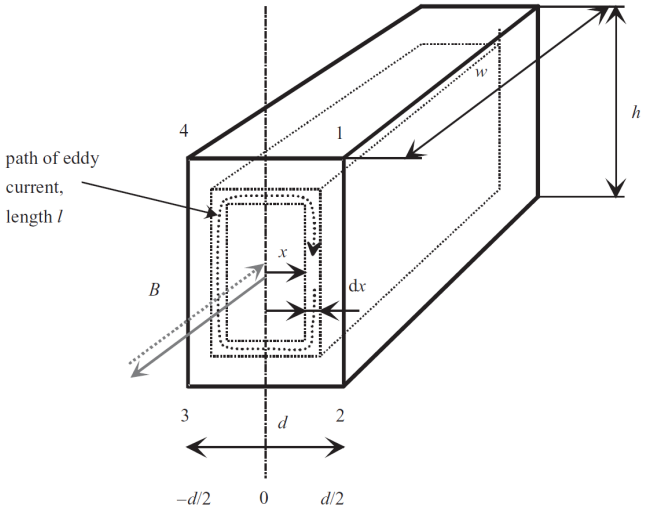


Figure 2.7: Schematic illustration of the eddy current in a electrical sheet [55]

Mechanical losses

Mechanical losses in electrical machines primarily consist of bearing friction losses and windage losses. Fig. 2.8 shows the schematic locations of the bearing friction losses and windage losses in the air-gap.
Bearing losses depend on shaft speed, bearing type, lubricant properties, bearing geometry and bearing load [55]. The guideline for calculation of bearing losses is usually provided by the manufactures, which is also shown briefly as follows [59]:

$$P_{\text{bearing}} = 0.5 \cdot \Omega \mu F D_{\text{bearing}} \tag{2.10}$$

where Ω is the angular rotor speed, μ is the friction coefficient, F is the bearing load and D_{bearing} is the inner diameter of the bearing.
Windage losses are due to friction between the rotor outer surface and the the air-gap. Windage losses can be calculated as follows [55, 60]:

$$P_{\text{windage}} = \frac{1}{32} \cdot k_{\text{roughness}} C_M \pi \rho \Omega^3 D_r^4 l_r \tag{2.11}$$

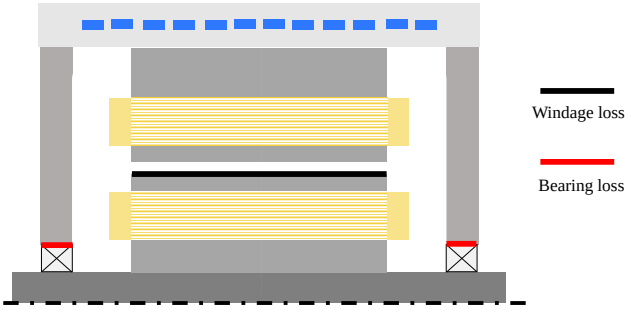


Figure 2.8: Major mechanical losses in the EESM cross section

where $k_{\text{roughness}}$ is the roughness coefficient, C_M is the torque coefficient, ρ is the coolant density, Ω is the rotor angular velocity, D_r is the rotor outer diameter and l_r is the rotor length.
Comparing of (2.10) and (2.11) reveals that the bearing losses are linearly proportional to the rotor angular velocity and the windage losses scale cubically to the rotor angular velocity, indicating the dominant role of windage at high operating speeds [55].

2.2 EESM thermal network based on LPTN method

The investigated motor is a 36-slot/6-pole EESM, the cross-section of which is shown schematically in Fig. 2.9. The motor has water jacket cooling on the stator side. Based on this reference motor, the corresponding thermal network topology is discussed in the following section.

2.2.1 Topology

Fig. 2.10 shows the thermal network of the EESM. It consists of five types of elements: thermal heat sinks at the system boundaries, node temperatures, power losses, thermal capacities and thermal resistances between nodes. Thermal resistances are further categorized by heat transfer mechanism: white elements

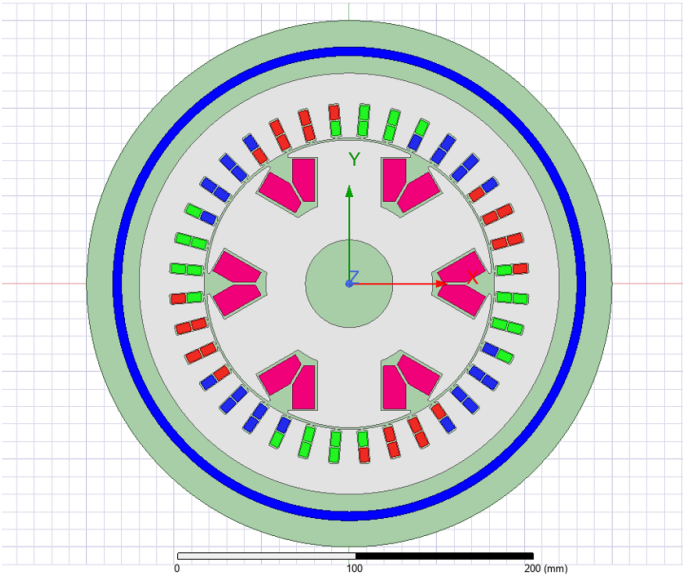


Figure 2.9: Schematic EESM cross section

indicate conduction, while blue elements indicate convection. The thermal network consist of seven nodes and can be classified as a light grey-box LPTN [8]. In Tab. 2.1, thermal resistances labeled from R_1 to R_{10} are also summarized with their physical interpretations.
Since a low-order thermal network represents a simplified abstraction of the actual motor, the estimation of these thermal resistances is due to complex motor geometry challenging. Therefore, simplifications are necessary. Fig. 2.11 schematically illustrates the motor's cross-section with heat transfer paths and corresponding node abbreviations. The adopted simplifications are summarized as follows:

- Unlike the PMSM thermal network, which typically includes only one rotor-side node (assuming rotor iron temperature equals rotor magnet temperature) [8, 9], the EESM network includes three rotor-side nodes (rotor iron, rotor active winding and rotor end winding) to account for the temperature gradient [E1].

Table 2.1: Thermal resistances in the network

Symbol	Heat transfer	Description
R_1	Conductive	Between frame and stator iron
R_2	Conductive	Between stator iron and stator active winding
R_3	Conductive	Between stator active winding and stator end winding
R_4	Convective	Between end caps and stator end winding
R_5	Convective	Between stator iron and rotor iron
R_6	Conductive	Between rotor iron and rotor active winding
R_7	Conductive	Between rotor active winding and rotor end winding
R_8	Convective	Between rotor end winding and end caps
R_9	Conductive	Between rotor iron and shaft
R_{10}	Conductive	Between shaft and flange

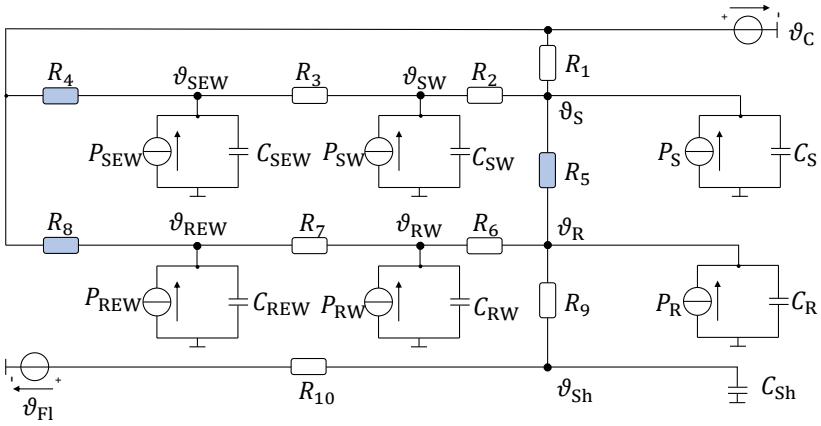


Figure 2.10: EESM thermal network [E1]

- Due to the high cooling flow rate in this study (see Chapter 3 as test set up), the motor frame is assumed to maintain the same temperature as the cooling water. Similarly, the cooling water temperature is assumed to be uniform along the flow path.

- The stator yoke and the stator teeth are modeled as a single thermal node. Likewise, the rotor yoke and the rotor teeth are modeled as a single thermal node.
- Due to the motor symmetry, the front and rear sections are modeled identically in the axial direction.
- Only the axial and radial heat flows are considered, while circumferential heat transfer is neglected.
- Only major losses affecting node temperatures, as shown in Fig. 2.10, are included. Mechanical losses including bearing losses and windage losses are not incorporated into the thermal network model. Although, according to [61], bearing losses have a significant influence on the temperature of the bearings components. Experiments conducted in [S1] — namely, measurements of the node temperatures in the proposed thermal network model with the motor unpowered and operated at different rotational speeds — indicate that the mechanical losses induced by motor rotation, i.e., bearing losses and windage losses, have a negligible effect on these nodes.
- According to sensitivity analysis, only dominant heat paths as shown in Fig. 2.11 are considered, other heat paths are neglected, such as the heat transfer path between the stator active winding and the rotor iron.
- Heat radiation becomes significant in natural cooled machines [54]. However, since the electrical machine is studied is actively cooled via stator water jacket, heat radiation is neglected in this study [37].

With these simplifications, the node temperatures of the EESM can be calculated using the associated loss model and thermal transfer theory, which are discussed in the subsequent sections.

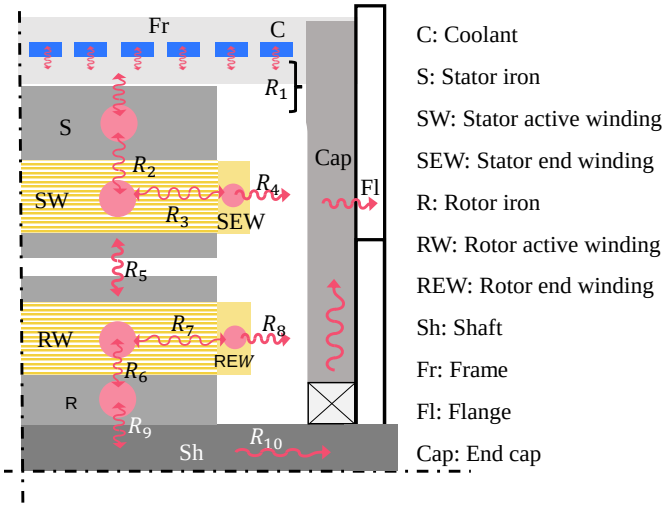


Figure 2.11: EESM cross section with important thermal paths as overview

2.2.2 Heat transfer modeling in EESM thermal network

Conduction heat transfer model unit for EESM

In the low-order thermal network, the stator and rotor geometries can be simplified as assemblies of hollow cylindrical components [15]. Fig. 2.12 illustrates the basic unit of a hollow cylinder. Thermal resistances in both radial and axial directions can be analytically estimated. In the figure, r_1 and r_2 denote the outer and inner radiuses of the cylinder, respectively, and L represents the motor's active length. Surface temperatures ϑ_1 and ϑ_2 correspond to the outer and inner surfaces, while ϑ_m represents the average radial temperature at the midpoint. Additionally, $\vartheta_\mathrm{A,m}$ and $\vartheta_\mathrm{B,m}$ indicate the average axial temperatures at either side of the cylinder.
This hollow cylindrical unit can be modeled thermally with two basic thermal models, which is depicted in Fig. 2.13 as T-type on the left side and I-types on the right side [62]. The calculating equations for radial and axial thermal resistances in the figure are given in (A.1) - (A.4) in the appendix. The T-type and I-type thermal model units differ in the level of simplification. While the I-type model

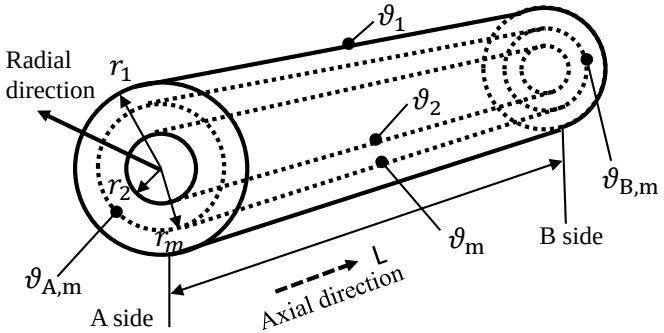


Figure 2.12: Hollow cylindrical shape as basic thermal unit [13]

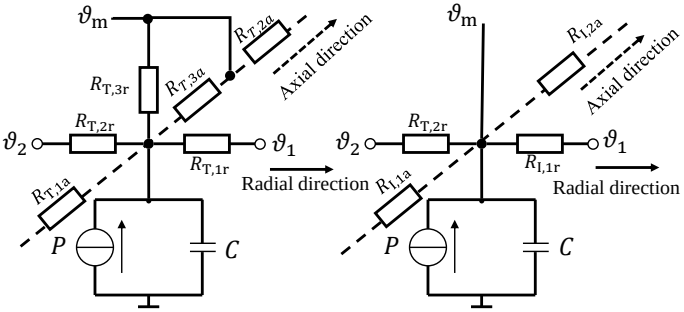


Figure 2.13: Basic thermal network unit in the electrical machine with LPTN approach. Left: T-type thermal network unit according to Mellor and Turner model [13]; Right: I-type thermal network unit according to Bolietti [15, 62]

tends to overestimate the average node temperature, the T-type model include the negative thermal resistances ($R_{\mathrm{T,3r}}$ and $R_{\mathrm{T,3a}}$), which serve as mathematical constructs to compensate for the overestimated temperature values [37]. These negative thermal resistances $R_{\mathrm{T,3r}}$ and $R_{\mathrm{T,3a}}$ lack physical meaning and are used purely for correction. Despite the T-Type model providing a more accurate estimation, according to [15] , the discrepancy in temperature estimation between the two model units remains within an acceptable range. The I-Type model unit

is adopted in this study due to its simplicity and the avoidance of non-physical parameters.
For modeling the thermal resistance of the windings, the equivalent thermal conductivity is computed using the Hashin-Shtrikman formulation [63].

$$\lambda_{\text{winding}} = \lambda_{\text{p}} \frac{(1+\upsilon_{\text{c}})\lambda_{\text{c}} + (1-\upsilon_{\text{c}})\lambda_{\text{p}}}{(1-\upsilon_{\text{c}})\lambda_{\text{c}} + (1+\upsilon_{\text{c}})\lambda_{\text{p}}} \tag{2.12}$$

where λ_{winding} represents the equivalent winding thermal conductivity. The indices p and c refer to the impregnation and conductor materials, respectively, while υ denotes the volume fraction of each material.

Convection heat transfer in the EESM network

The analytical estimation of convective heat transfer in electrical machines is challenging, as convection is a complex and nonlinear physical phenomenon. As a result, most calculations rely on empirical formulas derived from experimental measurements.
In this study, the equivalent thermal resistances associated with the air-gap and end-cap regions are estimated primarily based on the models reported in the literature.
Air-gap convection is characterized using the dimensionless Taylor number, which is defined as:

$$Ta_{\text{a}} = \frac{\Omega {r_{\text{m,a}}}^{0.5} (b-a)^{1.5}}{\upsilon} \tag{2.13}$$

where Ω is the angular velocity, $r_{\text{m,a}} = (a+b)/2$ is the mean annulus radius, υ is the is the kinematic viscosity, and a, b are the inner and outer radii of the air-gap, respectively. The flow regimes in the air-gap are identified using the ratio ${Ta_{\text{a}}}^2/{F_{\text{g}}}^2$, where F_{g} is the geometry factor, typically simplified to 1 in electrical machine applications [64, 65]. Based on this ratio, the Nusselt number Nu can be approximated by the following empirical relationships [66–68]:

$$\begin{aligned}
&{Ta_{\text{a}}}^2/{F_{\text{g}}}^2 < 1700 && Nu = \frac{2[(b-a)/a]}{\ln[1+(b-a)/a]} \\
&1700 < {Ta_{\text{a}}}^2/{F_{\text{g}}}^2 < 10^4 && Nu = 0.128 \cdot ({Ta_{\text{a}}}^2/{F_{\text{g}}}^2)^{0.367} \\
&10^4 < {Ta_{\text{a}}}^2/{F_{\text{g}}}^2 < 10^7 && Nu = 0.409 \cdot ({Ta_{\text{a}}}^2/{F_{\text{g}}}^2)^{0.241}
\end{aligned} \tag{2.14}$$

The convective heat transfer coefficient in the air-gap is then determined as:

$$h_{\text{airgap}} = \frac{Nu \cdot \lambda_{\text{a}}}{2(b-a)} \tag{2.15}$$

where h_{airgap} represents the air-gap heat convection transfer coefficient, and λ_{a} is the thermal conductivity of air.
To estimate heat transfer between the end-winding and the surrounding air in the endcap region, a simplified film coefficient is employed [13]. The heat transfer coefficient is used. The heat transfer coefficient is approximated as:

$$h_{\text{endwinding}} = k_1(k_2 v_{\text{ref}} + 1) \tag{2.16}$$

where $k_1 = 15.5$, $k_2 = 0.29$ are empirically determined curve-fitting parameters [69], and v_{ref} is the reference velocity of the airflow.

Thermal capacities in the EESM network

With the thermal resistances obtained, steady-state node temperatures can be computed. For transient thermal analysis, the thermal capacities of the nodes can be calculated as:

$$C_i = m_i \cdot c_i \tag{2.17}$$

where C is the heat capacity, c is the specific heat capacity and m is the mass of each node.

2.2.3 Loss modeling in the EESM thermal network

Losses serve as the input of the thermal network, therefore, precise estimation is crucial for accurate temperature estimation. This section presents the calculation of copper losses and the iron losses. As discussed in Section 2.2.1, secondary losses such as friction and windage are neglected in this work.

Winding losses calculation

Given that the EESM contains both stator and rotor windings, the copper losses for the stator and rotor are calculated as:

$$P_{\text{statorwinding}} = 1.5 \cdot k_{\text{r}} \cdot R_{\text{e,s}} \cdot ({i_{\text{d}}}^2 + {i_{\text{q}}}^2) \tag{2.18}$$

$$P_{\text{rotorwinding}} = R_{\text{e,r}} \cdot {i_{\text{r}}}^2 \tag{2.19}$$

where i_{d} and i_{q} denote the stator current components in the rotor-flux-oriented synchronous d–q coordinate system. $R_{\text{e,s}}$ and $R_{\text{e,r}}$ denote the stator and rotor DC resistances, respectively. The correction factor k_{r} accounts for the increase in AC resistance due to skin and proximity effects, and is frequency-dependent [55]. The approach for computing k_{r} is discussed in the following subsection.

Skin and proximity effects on k_{r}

Skin and proximity effects significantly increase the effective resistance of the windings under AC operation. To account both effects, the frequency-dependent pre-factor k_{r} is introduced [55, 56], defined as:

$$\begin{aligned} \xi &= h \cdot \sqrt{\frac{f}{50}} \cdot \sqrt{\frac{b}{a}} \cdot \sqrt{\frac{\gamma}{50}} \\ \varphi(\xi) &= \xi \frac{sh(2\xi) + sin(2\xi)}{ch(2\xi) - cos(2\xi)} \\ \Psi(\xi) &= 2\xi \frac{sh(\xi) - sin(\xi)}{ch(\xi) + cos(\xi)} \\ k_{\text{r}} &= \varphi(\xi) + \frac{N_n^2 - 1}{3} \Psi(\xi) \end{aligned} \tag{2.20}$$

where f is the current frequency, h, b are the height and width of the conductor, a is the width of the slot, γ is the conductor's material conductivity and N_{n} is the number of conductors in the slot height.
In order to validate the reliability of the analytical model, FEA can be employed in which each individual conductor within a slot is explicitly modeled. To reduce unnecessary computational effort, within the simulation software Ansys Maxwell, only one slot were modeled with wire conductors in detail, which is shown in Fig. 2.14. Based on the symmetry of the electrical machine, the skin and proximity effects of the whole active winding were estimated.

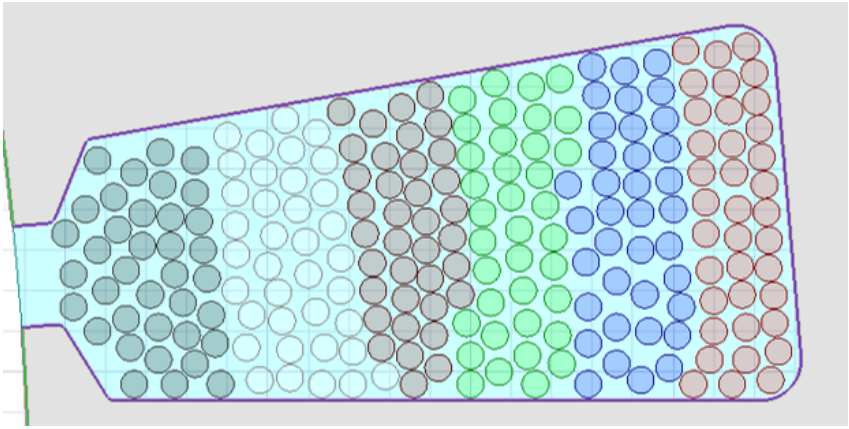


Figure 2.14: Skin and proximity effect modelling

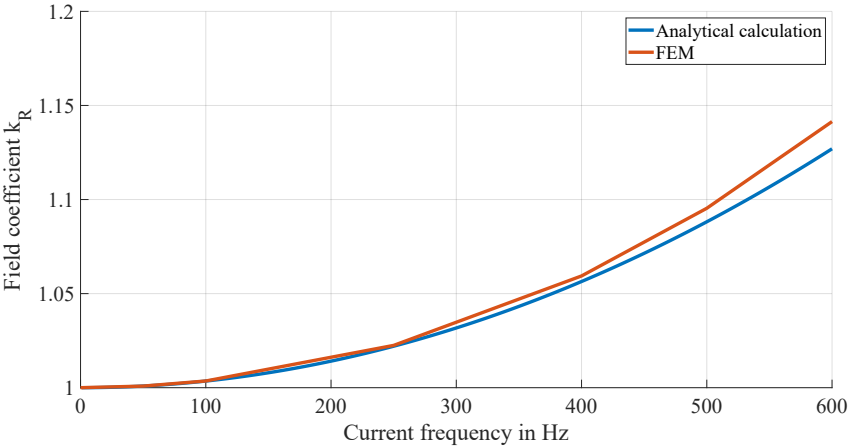


Figure 2.15: Comparison between the analytical and FEM estimation of skin and proximity effect

Fig. 2.15 compares the analytically computed k_r with results from FEA using Ansys Maxwell. The blue curve denotes the analytical calculation based on

(2.20), while the red curve presents the estimation from the FEA results from Ansys Maxwell. The analytical model slightly underestimates the losses at higher frequencies, but the deviation remains within an acceptable margin (e.g., 0.015 at 600 Hz). Therefore, the analytical formulas in (2.20) are used in this work.

Temperature dependency of the winding resistance

Since the winding resistance is temperature-dependent, this dependency must also be incorporated into the thermal network. The corresponding relationship can be expressed as:

$$R_{\mathrm{e}} = R_{\mathrm{e},0} \cdot [1 + \alpha \cdot (\vartheta - \vartheta_0)] \tag{2.21}$$

where R_{e} is temperature-adjusted resistance, $R_{\mathrm{e},0}$ is the reference resistance, α is the temperature coefficient of copper, ϑ_0 and ϑ are the reference and current temperatures.

Iron losses calculation

Iron losses constitute another major heat source and are modeled using a combination of FEA-based data and analytical approximation. The total iron loss P_{fe} consisting of hysteresis loss and eddy current loss is calculated as:

$$P_{\mathrm{fe}} = \underbrace{V \cdot B^2 \cdot k_{\mathrm{h}} \cdot f}_{\text{hysteresis loss}} + \underbrace{V \cdot B^2 \cdot k_{\mathrm{eddy}} \cdot f^2}_{\text{eddy current loss}} + \underbrace{V \cdot B^{1.5} \cdot k_{\mathrm{excess}} \cdot f^{1.5}}_{\text{excess loss}} \tag{2.22}$$

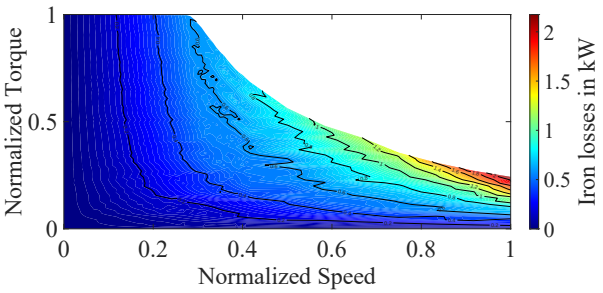
where V is the core volume, k_{h} and k_{eddy} and k_{excess} are the material properties of the laminated core, B is the magnetic flux density (from FEA) and f is the current frequency. For the used iron material, the factor k_{excess} is assumed to be 0. Since B is not easily computed analytically, a polynomial approximation model is employed based on FEA results:

$$P_{\mathrm{fe}} = V \cdot (\sum_{k=1}^{n} u_{\mathrm{k}} \cdot {i_{\mathrm{d}}}^k + \sum_{k=1}^{n} v_{\mathrm{k}} \cdot {i_{\mathrm{q}}}^k + \sum_{k=1}^{n} w_{\mathrm{k}} \cdot {i_{\mathrm{r}}}^k)^2 \cdot (k_{\mathrm{h}} f + k_{\mathrm{eddy}} f^2) \tag{2.23}$$

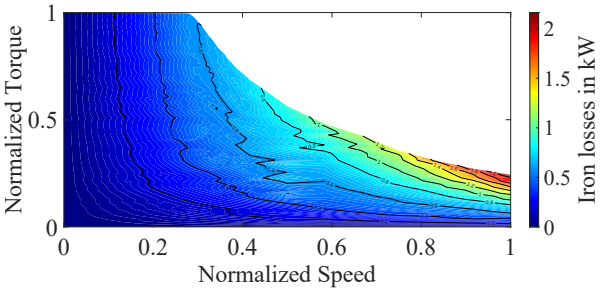
where the coefficients u_{k}, v_{k} and w_{k} are derived using the Least Squares Method (LSQ) fitting method to minimize the difference between the analytical model and FEA outputs:

$$f(u_{\mathrm{k}},v_{\mathrm{k}},w_{\mathrm{k}}) = \min_{u_{\mathrm{k}},v_{\mathrm{k}},w_{\mathrm{k}}} \sum_{k=1}^{n} (P_{\mathrm{Fe,FEA}} - P_{\mathrm{Fe,equation}})^2 \tag{2.24}$$

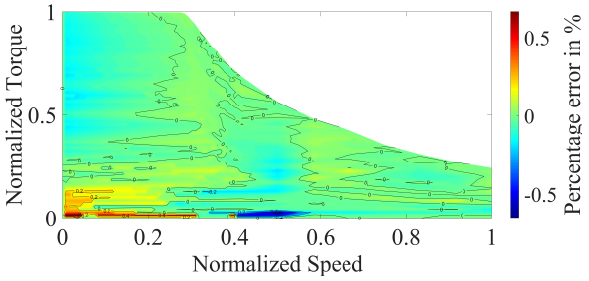
For practical implementation, a fourth-order polynomial ($k = 4$) in (2.23) is used with separate coefficients for two normalized speed intervals: $n \leq 0.5$ and $0.5 < n \leq 1$, as shown in Fig. 2.16:
Fig. 2.16 illustrates a comparison between the analytical and FEA results for stator iron losses. Specifically, Fig. 2.16 (a) is the estimated stator iron losses from FEA and Fig. 2.16 (b) is the stator iron losses estimated using (2.23). Fig. 2.16 (c) shows the percentage error compared to the FEA results. Although noticeable discrepancies appear in the low-loss region (0–50 W), their influence on the overall thermal behavior is negligible. In other regions, the analytical model exhibits strong agreement with the FEA simulations.



(a) Stator iron losses with FEA method



(b) Stator iron losses with iron loss model-based polynomial approximation



(c) Percentage deviation

Figure 2.16: Iron losses approximation between FEA method and polynomial approximation

2.2.4 Mathematical description of the EESM thermal network

Based on the principle of heat balance, the temperature variation at each thermal node is calculated by the thermal gradient between adjacent nodes and the internally generated losses, which can be described by the following general differential equation:

$$C_i \cdot \frac{d\vartheta}{dt} = \frac{1}{R_{ji}}(\vartheta_j - \vartheta_i) + P_i \tag{2.25}$$

where C_i is the thermal capacity of node i, ϑ_j and ϑ_i are the temperatures of node i and its adjacent node j. R_{ji} is the thermal resistance between nodes i and j, and P_i denote the losses generated at node i. According to the thermal network topology shown in in Fig. 2.10, the corresponding system of differential equations for the EESM thermal network can be written as:

$$C_{\mathrm{S}} \cdot \frac{d\vartheta_{\mathrm{S}}}{dt} = \frac{\vartheta_{\mathrm{C}} - \vartheta_{\mathrm{S}}}{R_1} + \frac{\vartheta_{\mathrm{SW}} - \vartheta_{\mathrm{S}}}{R_2} + \frac{\vartheta_{\mathrm{R}} - \vartheta_{\mathrm{S}}}{R_3} + P_{\mathrm{S}} \tag{2.26}$$

$$C_{\mathrm{SW}} \cdot \frac{d\vartheta_{\mathrm{SW}}}{dt} = \frac{\vartheta_{\mathrm{S}} - \vartheta_{\mathrm{SW}}}{R_2} + \frac{\vartheta_{\mathrm{SEW}} - \vartheta_{\mathrm{SW}}}{R_2} + P_{\mathrm{SW}} \tag{2.27}$$

$$C_{\mathrm{SEW}} \cdot \frac{d\vartheta_{\mathrm{SEW}}}{dt} = \frac{\vartheta_{\mathrm{C}} - \vartheta_{\mathrm{SEW}}}{R_4} + \frac{\vartheta_{\mathrm{SW}} - \vartheta_{\mathrm{SEW}}}{R_3} + P_{\mathrm{SEW}} \tag{2.28}$$

$$C_{\mathrm{R}} \cdot \frac{d\vartheta_{\mathrm{R}}}{dt} = \frac{\vartheta_{\mathrm{S}} - \vartheta_{\mathrm{R}}}{R_5} + \frac{\vartheta_{\mathrm{RW}} - \vartheta_{\mathrm{R}}}{R_6} + \frac{\vartheta_{\mathrm{Sh}} - \vartheta_{\mathrm{R}}}{R_9} + P_{\mathrm{R}} \tag{2.29}$$

$$C_{\mathrm{RW}} \cdot \frac{d\vartheta_{\mathrm{RW}}}{dt} = \frac{\vartheta_{\mathrm{R}} - \vartheta_{\mathrm{RW}}}{R_6} + \frac{\vartheta_{\mathrm{REW}} - \vartheta_{\mathrm{RW}}}{R_7} + P_{\mathrm{RW}} \tag{2.30}$$

$$C_{\mathrm{REW}} \cdot \frac{d\vartheta_{\mathrm{REW}}}{dt} = \frac{\vartheta_{\mathrm{RW}} - \vartheta_{\mathrm{REW}}}{R_7} + \frac{\vartheta_{\mathrm{C}} - \vartheta_{\mathrm{REW}}}{R_8} + P_{\mathrm{REW}} \tag{2.31}$$

$$C_{\mathrm{Sh}} \cdot \frac{d\vartheta_{\mathrm{Sh}}}{dt} = \frac{\vartheta_{\mathrm{R}} - \vartheta_{\mathrm{Sh}}}{R_9} + \frac{\vartheta_{\mathrm{A}} - \vartheta_{\mathrm{Sh}}}{R_{10}} + P_{\mathrm{SH}} \tag{2.32}$$

The differential equation system comprises seven differential equations, corresponding to the seven nodes of the low-order thermal network of the studied EESM. The subscripts S, SW, SEW, R, RW, REW and Sh represent the abbreviations of stator iron, stator active winding, stator end winding, rotor iron, rotor active winding, rotor end winding and shaft, respectively. The resistances R_1 to R_{10} represent the heat transfer paths between adjacent nodes or between nodes and the system boundary, as defined in Tab. 2.1. Using equations from (2.26) to (2.32), the transient temperature distribution of the EESM can be evaluated.

Chapter 3

Experimental setup and measurements

3.1 Test bench and reference motor

To collect the data required for parameter identification and to validate the thermal network model, the test bench is built as shown in Fig. 3.1. The reference motor is a 36-slot, 6-pol EESM with stator-side water jacket cooling. The inlet and outlet cooling channels are also marked in the figure.
On the stator side, temperatures were measured using Type T thermocouples, while on the rotor side, Type K thermocouples with higher temperature range were employed with supposed higher rotor winding temperatures. The rotor-side temperature signals were transmitted wirelessly to the control board via Bluetooth. To measure the boundary conditions, the coolant temperatures at the stator inlet and outlet were also recorded using Type T thermocouples, and the flange temperature was monitored using a Type K thermocouple. During all experiments, temperature values were recorded at 1-second intervals. The measurement intervals and signal tolerances are summarized in Tab. 3.1.

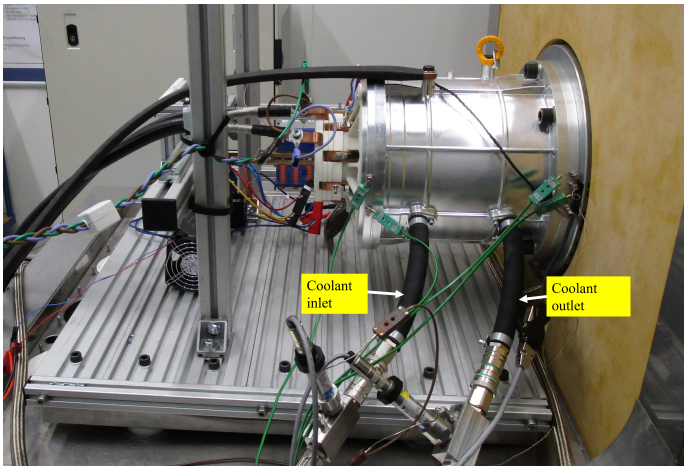


Figure 3.1: EESM test bench

Table 3.1: Technical data of the using thermocouples [70]

Type	Measurement interval	Standard limits of error
K	$-200\,°C$ to $1250\,°C$	greater of $2.2\,°C$ or 0.75%
T	$-250\,°C$ to $300\,°C$	greater of $1\,°C$ or 0.75%

3.2 Sensor locations and temperature measurements

The cross-section of the reference EESM and the sensor locations are shown in Fig. 3.2, while the corresponding sensor types are summarized in Tab. 3.2. On the stator side, the temperatures of the U-, V-, and W-phase windings were individually measured. The active winding temperatures at phase U, V, W are shown in Fig. 3.2 as $\vartheta_{\mathrm{SW,U}}$, $\vartheta_{\mathrm{SW,V}}$ and $\vartheta_{\mathrm{SW,W}}$, respectively. The stator end windings are further categorized into the A side (located on the same side as the winding bus bar) and the B side (opposite to the bus bar). For example, the temperatures of phase U at the locations of the A side, B side and active winding are shown in Fig. 3.2 as $\vartheta_{\mathrm{SEW,U,A}}$, $\vartheta_{\mathrm{SEW,U,B}}$ and $\vartheta_{\mathrm{SW,U}}$, respectively.

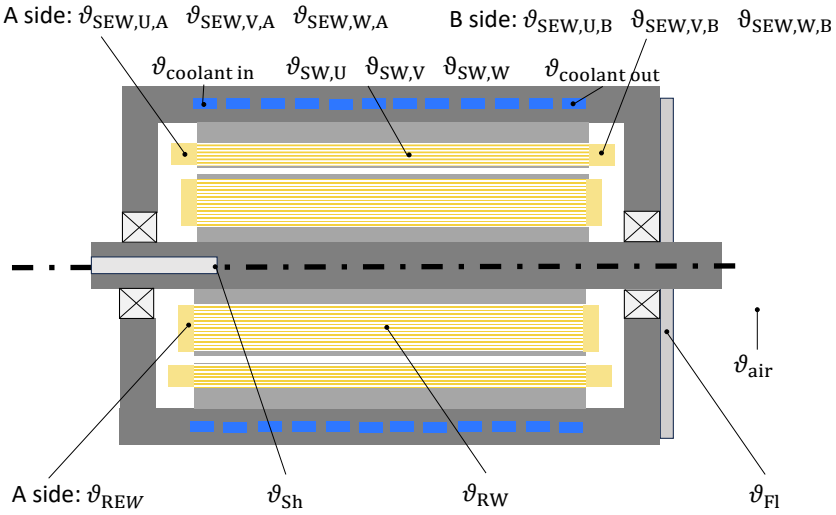


Figure 3.2: Schematic illustrated sensor locations

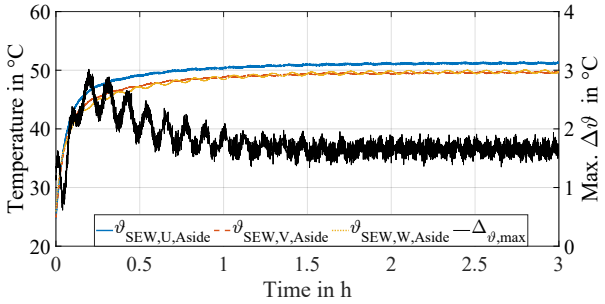
On the rotor side, the temperatures of the rotor active winding and the rotor end winding were measured. A end winding temperature sensor was installed, positioned on the side same to the bus bar. Moreover, the temperature inside the rotor shaft was measured to evaluate the thermal flow along the axial direction. In Fig. 3.2, temperatures of the rotor active winding, rotor end winding and inner shaft are illustrated as ϑ_{RW}, ϑ_{REW} and ϑ_{Sh}.
For thermal boundary conditions, the inlet and outlet temperatures of the water jacket, the ambient air temperature, and the temperature of the flange in direct contact with the housing were measured. Furthermore, the coolant flow rate inside the water jacket was also measured to assess the effective cooling performance. In Fig. 3.2, the inlet- and outlet temperatures of the cooling water jacket, the flange temperatures and the ambient air temperatures are shown as $\vartheta_{\mathrm{coolant\ in}}$, $\vartheta_{\mathrm{coolant\ out}}$, ϑ_{Fl} and ϑ_{air}, respectively.

Table 3.2: Motor temperature sensor locations and types

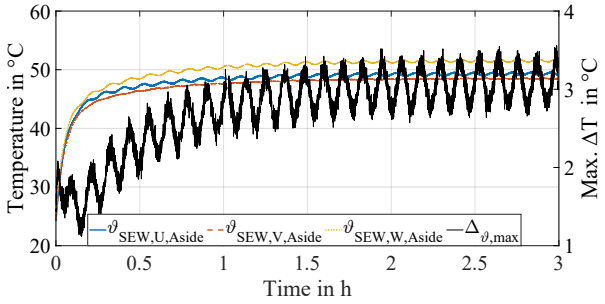
Sensor location	Description	Sensor Type
$\vartheta_{\mathrm{SW,U}}$	active winding temperature at phase U	Type T
$\vartheta_{\mathrm{SW,V}}$	active winding temperature at phase V	Type T
$\vartheta_{\mathrm{SW,W}}$	active winding temperature at phase W	Type T
$\vartheta_{\mathrm{SEW,U,A}}$	end winding temperature at phase U at A side	Type T
$\vartheta_{\mathrm{SEW,V,A}}$	end winding temperature at phase V at A side	Type T
$\vartheta_{\mathrm{SEW,W,A}}$	end winding temperature at phase W at A side	Type T
$\vartheta_{\mathrm{SEW,U,B}}$	end winding temperature at phase U at B side	Type T
$\vartheta_{\mathrm{SEW,V,B}}$	end winding temperature at phase V at B side	Type T
$\vartheta_{\mathrm{SEW,W,B}}$	end winding temperature at phase W at B side	Type T
ϑ_{RW}	rotor active winding temperature	Type K
ϑ_{REW}	rotor end winding temperature at A side	Type K
ϑ_{Sh}	inner shaft temperature	Type K
$\vartheta_{\mathrm{coolant\ in}}$	coolant inlet temperature	Type T
$\vartheta_{\mathrm{coolant\ out}}$	coolant outlet temperature	Type T
ϑ_{air}	ambient air temperature	Type K
ϑ_{Fl}	ambient flange temperature	Type K

Stator and rotor component measurements

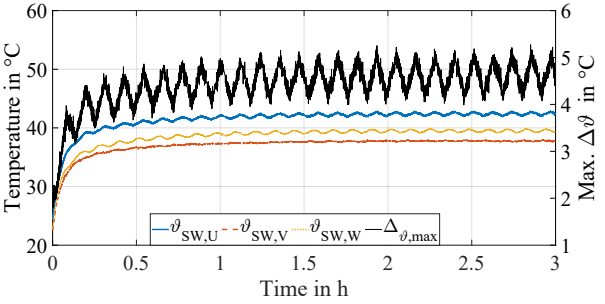
In Fig. 3.3, the motor winding temperatures were shown. The test duration was three hours. The blue, red, and yellow curves represent the temperatures of phases U, V, and W, respectively, referenced to the left y-axis. The black curve indicates the maximum temperature difference among the three phases, referenced to the right y-axis.
First, Fig. 3.3 (a) illustrates the temperatures of the stator end windings on the A-side for phases U, V, and W. Due to manufacturing tolerances, perfect symmetry among the three phases cannot be guaranteed. In addition, the placement of temperature sensors cannot be ensured to be identical for all phases. These factors lead to the measurement deviation. As shown in Fig. 3.3 (a), the temperature deviation initially increases to approximately $3\,^{\circ}$C, then decreases, and finally stabilizes with fluctuations below $2\,^{\circ}$C. A similar behavior can be observed in Fig. 3.3 (b), which presents the three-phase temperatures of the stator end windings on the B-side.
In Fig. 3.3 (c), the three-phase temperatures measured in the active winding are shown. Compared to the end-winding measurements, the phase temperature difference as black curve increases continuously during the experiment and reaches approximately $5\,^{\circ}$C, which is significantly higher than that observed in the end windings. This behavior can be attributed to the higher temperature gradient in the active winding region. Although the temperature sensors were supposed to be placed at the center of the stator slots, unavoidable positioning deviations during installation lead to this increased discrepancies among the three-phase temperature measurements.
It is worth noting that the measured temperatures exhibit a periodic fluctuation pattern, with varying amplitudes among the different phases. This behavior is presumed to be influenced by temperature variations in the cooling water of the water jacket. Furthermore, due to manufacturing tolerances in the prototype, the cooling performance is not entirely identical across the three phases, which leads to the observed phase-dependent periodic variations in the temperature profiles.



(a) Stator phase end winding temperatures in A side



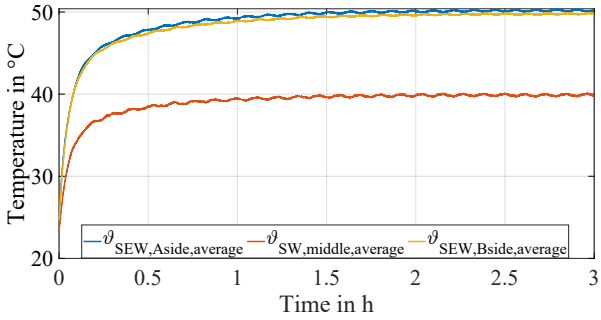
(b) Stator phase end winding temperatures in B side



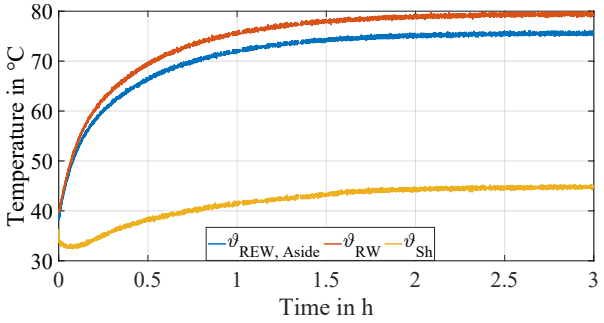
(c) Stator phase temperatures in the active winding

Figure 3.3: Stator phase winding temperature measurements at operating point 70 Nm and 3000 1/min

Fig. 3.4 illustrates the measured temperatures of the stator and rotor components of the electrical machine at the operating point of of 70 Nm and 3000 1/min. Fig. 3.4 (a) presents the measured and averaged winding temperatures at the stator side, including the end winding on the A-side and B-side, as well as the active winding. These temperatures are represented by the blue, red, and yellow curves, respectively. It can be observed that the temperatures of the A-side and B-side stator end windings are nearly identical. This confirms that the axial symmetry of the machine, which can be reasonably used to simplify the corresponding thermal network model.
Furthermore, it is evident in Fig. 3.4 (a) that the temperature of the stator active winding is significantly lower than that of the end windings. This behavior can be explained by the fact that the stator does not rotate; therefore, the convective heat transfer between the stator end windings and the surrounding air is relatively weak compared to that of the rotor windings. As a result, heat generated in the stator end windings cannot be efficiently dissipated through the end space. In contrast, the stator active winding is within the stator core, allowing heat to be more effectively conducted from the active winding into the stator iron, then through the housing, and finally dissipated via the water jacket. Consequently, the end windings exhibit a higher temperature than the active winding in the stator.
Fig. 3.4 (b) shows the measured temperatures of the rotor-side components. In this figure, the blue, red, and yellow curves represent the temperatures of the rotor end winding, active winding, and inner shaft, respectively. Unlike the stator windings, the rotor active winding exhibits a higher temperature than the rotor end winding, indicating a different dominant heat flow direction: from rotor active winding to the rotor end winding and via heat convection to the end space. This phenomenon can be attributed to the high rotational speed of the rotor windings, which significantly enhances convective heat transfer between the rotor end windings and the end space. As a result, heat is more likely to be dissipated from the rotor end windings directly into the end space rather than flowing through the active winding and across the air gap toward the stator.
By comparing the temperatures of the rotor active winding and the inner shaft, an additional heat transfer path can be identified: heat flows from the rotor windings through the rotor iron and subsequently into the shaft. From the shaft, heat is conducted through the bearings to the end region and then dissipated to the ambient environment.



(a) Stator component average temperatures



(b) Rotor component temperatures

Figure 3.4: Motor component temperature measurements at operating point 70 Nm and 3000 1/min

Summary and simplification

Overall, it can be concluded that three-phase asymmetry introduced by the manufacturing process of the motor prototype, together with deviations in the placement of temperature sensors, results in measurable temperature differences among the U-, V-, and W-phase stator windings. Nevertheless, the overall deviation is within $5\,^{\circ}\mathrm{C}$. The worst case observed in Fig. 3.3 is the U-phase, with $5\,^{\circ}\mathrm{C}$ higher temperature as the V- and W-phase. To ensure consistency in subsequent model parameter identification based on experimental data as well as in cross-validation, the temperature of the U-phase stator winding as the most critical phase temperature is uniformly adopted as the reference of the measured stator winding temperatures.
In addition, Fig. 3.4 confirms the thermal consistency of the stator end winding between the A-side and the B-side. Therefore, in the subsequent studies, the end-winding temperature measured on the A-side is consistently used as reference of the measured stator end winding temperatures.

Boundary condition measurements

The boundary conditions used during the tests are illustrated in Fig. 3.5 by operating point $70\,\mathrm{Nm}$ and $3000\,1/\mathrm{min}$. Specifically, Fig. 3.5 (a) shows the ambient temperature, including the air temperature ϑ_{air} and the flange temperature ϑ_{Fl}. From this figure, it can be observed that the initial temperature of the flange is slightly lower than the ambient room temperature due to the cooling temperature of the water jacket. However, as the experiment progressed, the flange temperature exceeded the ambient temperature. Besides, since the motor was tested in an enclosed room (see Fig. 3.1), the heat generated during operation also affected the ambient temperature. As a result, the room temperature showed a gradual increase throughout the test.
The coolant system was configured with a target cooling flow rate of $8\,\mathrm{L/min}$ and a target inlet temperature of $20\,^{\circ}\mathrm{C}$. The actual cooling flow rate are shown in Fig. 3.5 (b). Minor fluctuations in flow rate were observed throughout the experiment. The average and maximum fluctuation values were calculated as follows:

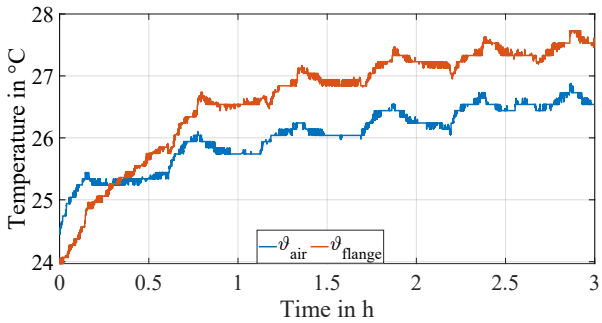
$$\begin{aligned} Q_{\mathrm{avg}} &= 7.9\,\mathrm{L/min} \\ \Delta Q &= 0.093\,\mathrm{L/min} \end{aligned} \tag{3.1}$$

Comparison with the target value confirms that the actual average flow rate was very close to the set flow rate, with a deviation of only $0.1\,\mathrm{L/min}$. The maximum

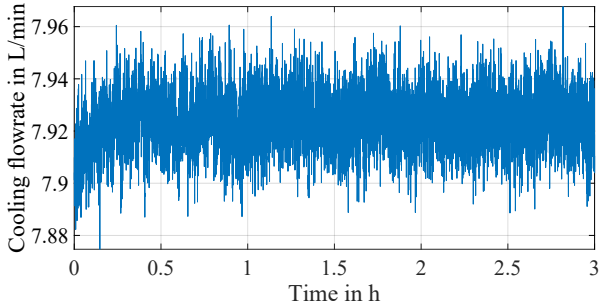
fluctuation during the whole test remained within $0.093\,\mathrm{L/min}$, indicating that the cooling performance of the water-glycol mixture was stable and reliable.
Fig. 3.5 (c) displays the measured inlet and outlet temperatures of the coolant. Due to heat dissipation from the electrical machine, the outlet temperature is higher than the inlet temperature. The average temperatures and their difference were determined as:

$$\begin{aligned} \vartheta_{\text{inlet,avg}} &= 20.3\,^{\circ}\mathrm{C} \\ \vartheta_{\text{outlet,avg}} &= 22.2\,^{\circ}\mathrm{C} \end{aligned} \tag{3.2}$$

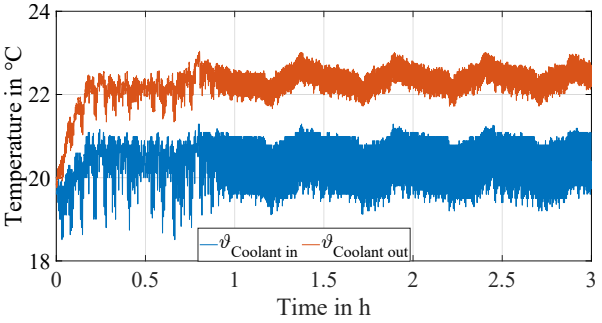
Given the high coolant flow rate, the temperature gradient along the cooling channel was considered negligible. Consequently, the inlet temperature was used as the cooling boundary condition in the subsequent thermal network modeling.



(a) Flange temperature profile



(b) Coolant flowrate profile



(c) Coolant inlet and outlet temperatures profile

Figure 3.5: Boundary conditions of the static test at speed 3000 1/min, torque 70 Nm

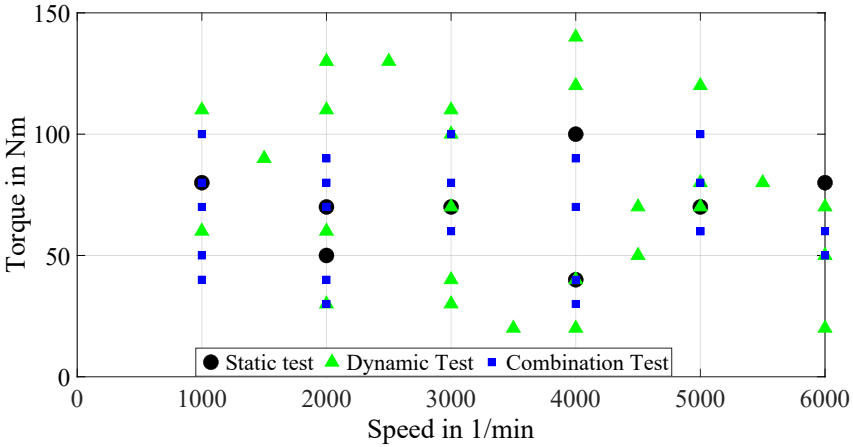


Figure 3.6: Summary of the operating points according to test types

3.3 Thermal driving cycle tests

The test bench shown above was used to perform various driving cycles to evaluate the thermal behavior of the electrical machine. The operating points that have already been tested are summarized in Fig. 3.6. In this figure, black circles denote the operating points of the static test, green triangles denote those of the dynamic test, and blue squares denote those of the combination test. In Fig. 3.7, one operating point will be arbitrarily selected for each test type to illustrate the corresponding component temperature profiles.

Static test in Fig. 3.7 (a)

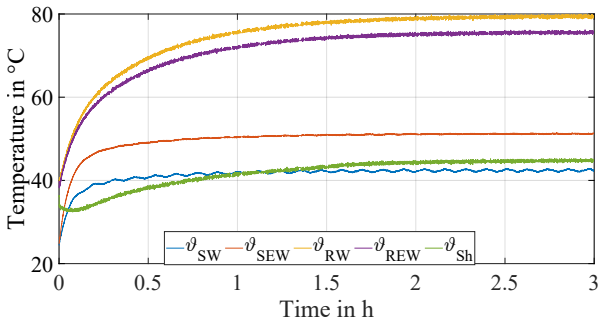
The static test was designed to assess the steady-state thermal behavior of the machine. The test duration was set to a constant speed and torque for three hours to ensure that the electric motor reached steady-state. As shown in Fig. 3.7 (a) as an example, the motor was set to 3000 1/min and 70 Nm, with inlet cooling temperature of 20 °C. The component temperatures initially increased continuously and then stabilized. These final values are referred to as the steady-state temperatures, which were defined as conditions where the temperature variation $\Delta\vartheta$ changed within 2 K pro minute.

Dynamic Test in Fig. 3.7 (b)

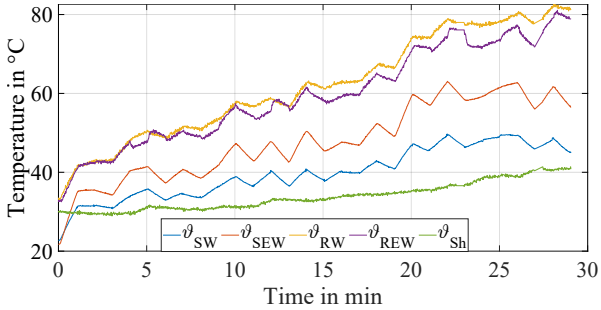
The dynamic test was conducted to investigate the transient temperatures of the electric motor. In the dynamic test, the operating point was changed every one minute. The dynamic tests showed the dynamic behaviour of the electrical machine and the goal was to validate the ability of the thermal network to accurately represent the machine's dynamic thermal behavior. The total test duration of the dynamic test was 29 mins.

Combination Test in Fig. 3.7 (c)

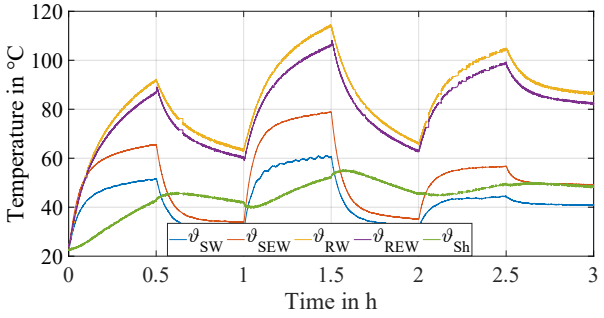
The combination test served to evaluate both steady-state and dynamic performance. In this test, the operating points were altered every 30 minutes. Although component temperatures exhibited convergence behavior at each stage, they did not reach full steady-state due to limited duration. This test aimed to validate the thermal model under more realistic and mixed operational conditions, encompassing both steady and transient thermal responses.



(a) Static test



(b) Dynamic test



(c) Combination test

Figure 3.7: Different types of tests with measured motor component temperatures

Chapter 4

Model parameter identification and validation

To describe thermal behavior of the electrical machine, two main approaches are commonly employed: the theoretical approach, which is based on the derivation of physical principles, and the empirical approach, which relies on empirical mathematical fitting models derived from experimental data [71]. Each method has its own advantages and limitations. The theoretical approach yields universal, parameterized models. However, due to incomplete measurements, some unknown parameters may not be taken into account, potentially leading to deviations. In contrast, the empirical approach ensures closer alignment with reality through direct measurement, but in the absence of explicit analytical formulas, extensive experimental data are required to train the model.
The parameter identification approach proposed in this thesis integrates both analytical and empirical approaches. Initially, a physically based model is built using the analytical method. Subsequently, by analysing system input and output measurements, the analytical model is refined through parameter identification. Parameter identification can be categorized in two types: direct and indirect parameter identification. As illustrated in Fig. 4.1, direct parameter identification involves estimating parameters directly by analyzing the system's input and output. This approach is typically applied to relatively simple systems. For instance, by examining the voltage (input) and current (output) across a resistor, the resistance value can be directly determined. In contrast, Fig. 4.2 presents the general principle of indirect parameter identification, where parameters are estimated indirectly through additional computational steps, because the

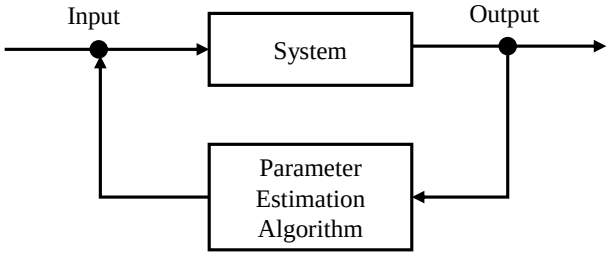


Figure 4.1: Direct parameter identification [71]

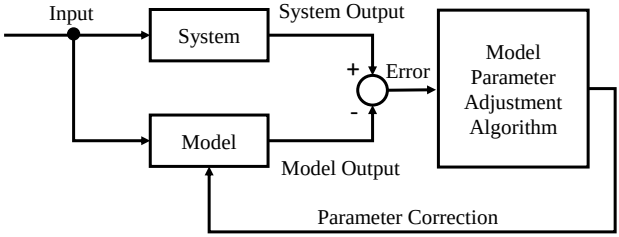


Figure 4.2: Indirect parameter identification [71]

model parameters are difficult to access or measure straightforwardly. Instead, model parameters are inferred indirectly by comparing the measured physical outputs. Indirect parameter identification is typically employed for complex systems, where direct estimation of parameter is challenging or not possible.
The identification procedure employed in this work can be classified as an indirect parameter identification. The inputs to the system are the motor currents and the speed, while the outputs are the motor temperatures. The parameters to be estimated are the thermal resistances and the thermal capacities within the thermal network. According to [72], this indirect parameter identification can be performed following the procedure outlined below:

- Definition of the model structure and identification method

- Collecting the test data
- Definition of the cost function and the quality criterion
- Cross-validation

Based on the above procedure, the model structure is discussed in this section. First, a novel static-dynamic parameter identification method is introduced, along with the definition of cost function and quality criterion. Subsequently, the results of the parameter identification are presented. Based on these results, a basic thermal analysis of the reference motor is carried out. Finally, the optimized thermal network is experimentally validated through cross-validation.

4.1 Local and global identification of the LPV system

Two main approaches for parameter identification for electrical machines's thermal network have been discussed in the literature: the local parameter identification and the global parameter identification [8, 9, 19, 73, 74]. In the local parameter identification, the Linear Parameter-Varying Model (LPV) system is treated as a quasi-LTI system at each operating point. For instance, in [19], the the thermal network's parameters were identified based on measured temperatures at specific operating points and the identified results were combined into a LUT. This method ensures high model accuracy around the identified operating points [9]. However, it leads to inconsistency and reduced robustness across the full operating range [8, 75]. In contrast, the global parameter identification first describes the varying parameters through empirical formulas, and the parameters of these formulas are then identified during the parameter identification process. By using the empirical expressions instead of LUT, this method achieves greater consistency and robustness. In [8], Wallscheid first introduced the global parameter identification to model the thermal network of the PMSM.
In this thesis, a global parameter identification approach is adopted to identify the speed-dependent thermal resistances of the EESM. Following the method proposed in [8], the speed-dependent convection thermal resistances (R_4, R_5 and R_8) are modeled as natural exponential function with an offset:

$$R_i(n) = a_i + b_i \cdot e^{-E_i \cdot \frac{n}{n_{\max}}} \tag{4.1}$$

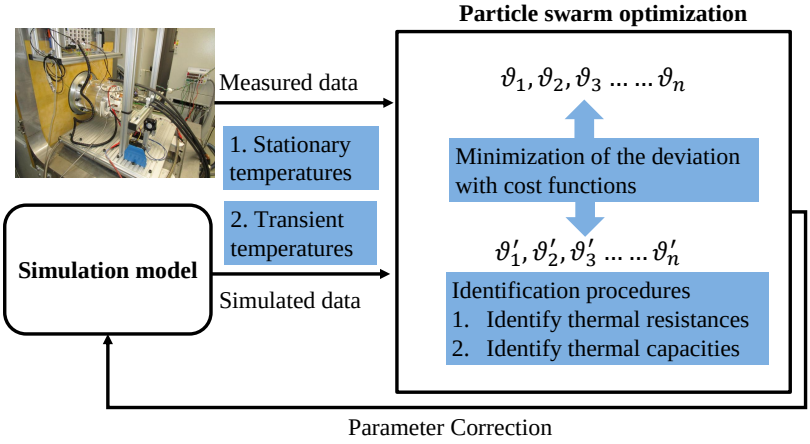


Figure 4.3: Principle of combined static-dynamic identification with particle swarm optimization

where a_i is the natural convection and $b_i \cdot e^{-E_i \cdot \frac{n}{n_{\max}}}$ is the forced convection related to the rotor speed. n is the current motor speed and n_{max} is the maximum motor speed. The initial values of a_i, b_i and E_i are estimated according to the analytical formulas presented in chapter 2.2.2.

4.2 Combined static-dynamic identification

The global parameter identification proposed by [8] is an inverse method based on measured node temperatures. However, both thermal resistance and thermal capacity influence the node temperatures, making it difficult to identify.
To address this issue, this thesis introduces a combined static-dynamic identification approach, allowing for the separate identification of thermal resistances and thermal capacities. The principle of this combined static-dynamic global identification is illustrated in Fig. 4.3. Particle Swarm Optimization (PSO) was employed as the model parameter identification algorithm, and identification was implemented in the MATLAB environment. The identification procedure is divided into two stages: static identification and dynamic identification.

Static identification

In the context of static identification, the parameters of the thermal resistances can be identified first. The principle of static identification is based on the following equation:

$$\frac{1}{R_{ji}}(\vartheta_{\mathrm{s},j} - \vartheta_{\mathrm{s},i}) + P_i = 0 \;\; i,j = 1,2,...7 \tag{4.2}$$

where R_{ji} represents the thermal resistance between nodes i and j. ϑ_{s} denotes the steady-state temperature of the node, and P_i is the power loss of the node. Equation (4.2) is derived from (2.32) under the assumption $d\vartheta/dt = 0$, which reflects the steady-state condition. Setting $d\vartheta/dt = 0$ allows (4.2) to describe the thermal steady-state behaviour of the electrical machine. At steady-state, the node temperatures are independent of the thermal capacities. As a result, the thermal resistances can be estimated without the influence of the thermal capacities. The cost function for global static identification is defined as follows:

$$J_{\mathrm{s}} = \sum_{z=1}^{a}\sum_{i=1}^{b} w_i(\frac{\vartheta_{s,m} - \vartheta_{s,e}}{\vartheta_{s,e}})^2 \tag{4.3}$$

where $\vartheta_{\mathrm{s,m}}$ is the measured steady-state temperature. $\vartheta_{\mathrm{s,e}}$ is the estimated steady-state temperature. w_i is the weighting factor for each component, which is set to 1 in this study, meaning that all nodes are treated equally during the optimization. b is number of components, and a is the number of static thermal cycles. The indicator J_{s} represents the deviation between the measured data and the model estimation during the static parameter identification process.
The following operating points in Tab. 4.1 are used for the static identification. For each operating point, the test is conducted for a duration of three hours to ensure that the temperatures of the corresponding components reach steady-state conditions. The steady-state temperatures of these components are then recorded and used for model static identification. The test points are also illustrated in Fig. 3.6 as static test.

Table 4.1: Operating points used for the model static identification

Number	Speed in /min	Torque in Nm
1	2000	70
2	4000	100
3	1000	80
4	3000	70
5	5000	70
6	6000	80
7	2000	50
8	4000	40

Dynamic identification

In terms of the dynamic identification, thermal capacities can be identified during a transient thermal cycle. The principle of dynamic identification is based on the following equation:

$$\frac{1}{R_{ji}}(\vartheta_{\mathrm{t},j} - \vartheta_{\mathrm{t},i}) + P_i = C_i \cdot \frac{d\vartheta_{\mathrm{t}}}{dt} \quad i,j = 1,2,...7 \tag{4.4}$$

where ϑ_{t} represents the transient node temperature. Given the identified thermal resistance R_{ji} identified through static global identification, the primary objective of dynamic global identification is to determine the thermal capacities C_i. For dynamic identification, the cost function is defined as follows:

$$J_{\mathrm{d}} = \sum_{k=1}^{x}\sum_{i=1}^{y} w_i(\frac{\vartheta_{t,m} - \vartheta_{t,e}}{\vartheta_{t,e}})^2 \tag{4.5}$$

where $\vartheta_{\mathrm{t,m}}$ denotes the measured transient temperatures, and $\vartheta_{\mathrm{t,e}}$ represents the estimated transient temperatures. w_i is the weighting factor for each component, which is also set to 1 during the optimization. y is the number of the components, and x is the number of measured data points within the transient cycle. The indicator J_{d} quantifies the deviation between the measured data and the model estimation during the dynamic parameter identification process.
For the dynamic identification process, the transient temperatures of the operating point 3000 1/min and 70 Nm as shown in in Fig. 3.7 (a) were used.

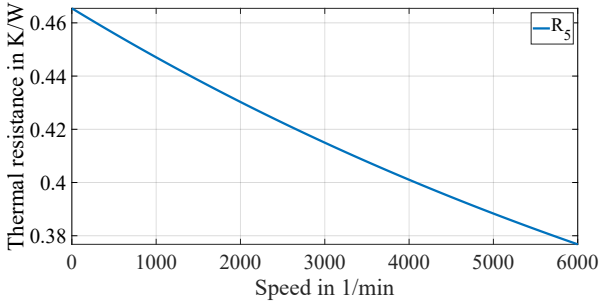
Table 4.2: Conductive thermal resistances and thermal capacities

Symbol	Thermal resistance in K/W	Symbol	Thermal capacity in J/K
R_1	0.017	C_{S}	9117
R_2	0.026	C_{SW}	3628
R_3	0.122	C_{SEW}	1102
R_6	0.119	C_{R}	6894
R_7	0.058	C_{RW}	885
R_9	0.293	C_{REW}	166
R_{10}	0.265	C_{Sh}	2522

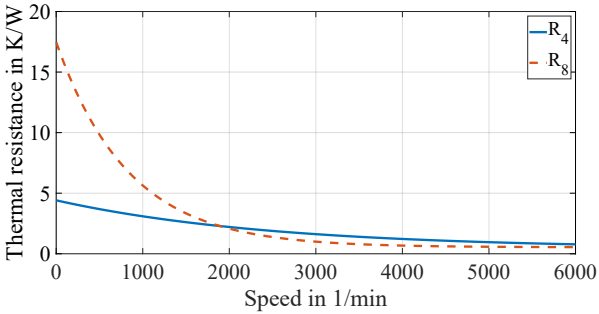
4.3 Training results

Using the combined static-dynamic parameter identification introduced above, the thermal resistances and capacities in the EESM can be determined. The conductive thermal resistances and thermal capacities are summarized in Tab. 4.2.

The equivalent convective thermal resistances R_4, R_5 and R_8 are shown in Fig. 4.4 (a) and Fig. 4.4 (b). Fig. 4.4 (a) illustrates the equivalent thermal resistance R_5 of the air gap, which decreases as the rotor speed increases. This trend occurs because the airflow in the air gap transitions from laminar to turbulent convection with increasing rotor speed [76]. Fig. 4.4 (b) shows the equivalent thermal resistance between the end windings and the end space, which also decrease with increasing rotor speed. This is due to the rotor's rotation promoting airflow circulation in the end space, thereby enhancing convective heat dissipation in the end space of the motor [69].



(a) Thermal resistance of the air-gap



(b) Thermal resistance between the end windings and the end space

Figure 4.4: Convective thermal resistance

4.4 Thermal analysis with LPTN thermal network

The thermal behavior of the EESM can also be analyzed using the LPTN network. Fig. 4.5 shows the schematic thermal flow of the EESM under steady-state conditions at an operating point of $3000\,1/\text{min}$ and $70\,\text{Nm}$ as an example. Each box in Fig. 4.5 represents a node of the EESM thermal network, as previously illustrated in Fig. 2.10. The copper and iron losses, calculated in the LPTN network at steady-state, are also presented. Arrows between the nodes indicate the direction of heat flow, with the calculated heat flow values shown along the arrows. Fig. 4.5 demonstrates that the majority of losses are dissipated through the stator iron to the water jacket cooling system. Minimal heat dissipation occurs through the end space area to the housing or through the shaft to the flange.
An interesting observation is the opposing heat flow directions between the stator winding and the rotor winding. Specifically, $76\,\text{W}$ of losses are transferred from the stator end winding to the stator active winding, whereas $32\,\text{W}$ of losses are transferred from the rotor active winding to the rotor end winding. This behavior is due to the rotor's rotation, which enhances convective heat transfer from the rotor end winding to the surrounding air, resulting in a lower temperature at the rotor end winding compared to the rotor active winding. In contrast, the stator winding remains stationary, limiting convective heat transfer from the stator coils to the surrounding end space. As a result, heat transfer predominantly occurs via conduction from the stator active winding to the stator core, causing the stator end winding to exhibit a higher temperature than the stator active winding.
Using the LPTN thermal network, the sensitivity analysis of the thermal resistances was also carried out. As an example, the influence of the stator end space resistance R_4 and the air gap resistance R_5 on the node temperatures is discussed. Fig. 4.6 shows the sensitivity analysis for R_4/S, R_4 and $R_4 * S$. R_4 denotes the thermal resistance between the end caps and the stator end winding, and S is a variation factor, setting to $S = 2$ in this case. It can be observed that variations in R_4 primarily influence the the network component locally, i.e. the stator end winding. Fig. 4.7 presents the sensitivity analysis with respect to variations of the thermal resistance R_5, where R_5 represents the air gap thermal resistance. It can be seen that all components from the rotor side are sensitive to changes in R_5.

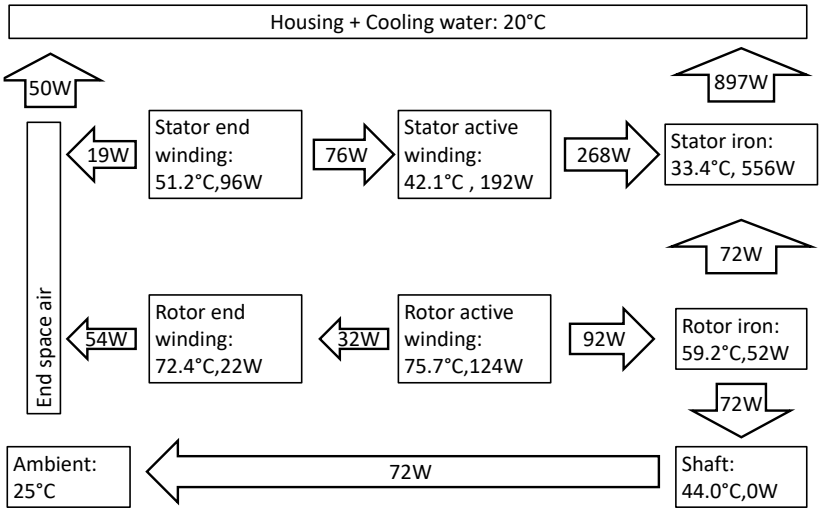


Figure 4.5: Thermal flow at steady-state by working point 3000 1/min and 70 Nm

4.5 Cross validation with thermal cycles

Using the identified parameters, the thermal network was validated against different dynamic drive cycles. Fig. 4.8 and Fig. 4.9 present four cross validation tests. The selected operating points differed from the training data to ensure proper cross validation. Two types of tests were conducted. In combination tests (see also in Chapter. 3.3), the operating points were switched every 0.5 hour. To validate the more dynamic behaviour of the electrical machine, a dynamic test (see also in Chapter. 3.3) was conducted, as illustrated in the right column of Fig. 4.9. In this case, the operating points were switched every 1 minute, in order to better observe the machine's dynamic thermal behaviour.
In figures (Fig. 4.8 and Fig. 4.9), the measured data are shown as solid blue curves, while the thermal network estimations are represented by dashed red lines. Both the measured and estimated temperature curves are plotted against the left axis. The deviation between the measured and estimated temperatures is shown as solid black curves plotted against the right axis.

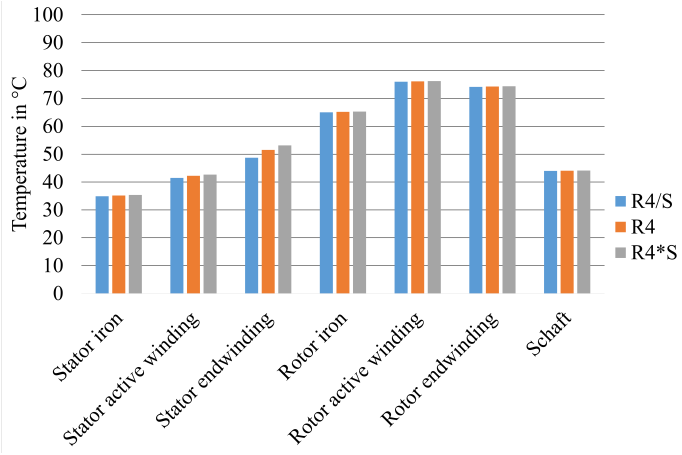


Figure 4.6: Sensitivity analysis of the stator end space resistance with $S = 2$ based on the steady temperatures at 3000 1/min and 70 Nm

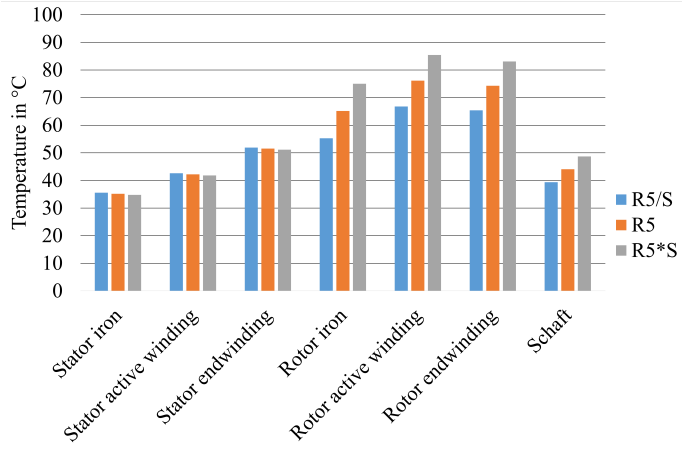
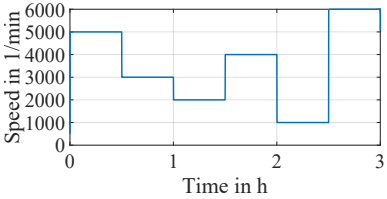
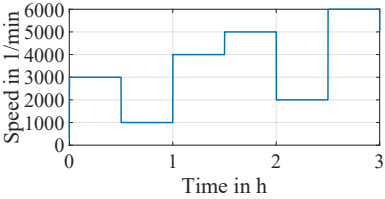


Figure 4.7: Sensitivity analysis of the air gap resistance with $S = 2$ based on the steady temperatures at 3000 1/min and 70 Nm

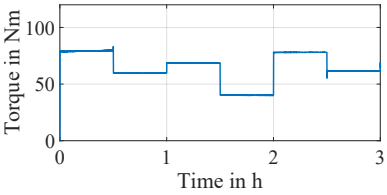
All the tests were performed with an inlet cooling water temperature of 20 °C. The measured temperatures were recorded at a sampling rate of 1 sample pro second. The figures also display the measured rotor speed, torque and a selection of node temperatures. The black solid curves clearly indicate the deviations between the estimations and the measurements. It can be observed that, across all dynamic drive tests, the deviations between the measured and estimated temperatures remain within +/- 10 K.
It should be noted that the tests presented here are only part of the validation efforts carried out. Nevertheless, the results demonstrate the accuracy of the thermal network in predicting the thermal behaviour of the studied EESM. Across all the validation tests, the deviation between the motor and the thermal network estimation maintained within +/- 10 K.



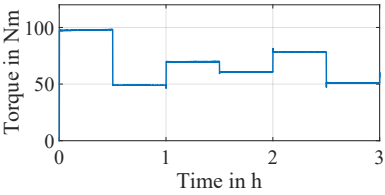
(a) Measured speed in dynamic cycle 1



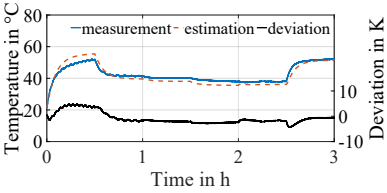
(b) Measured speed in dynamic cycle 2



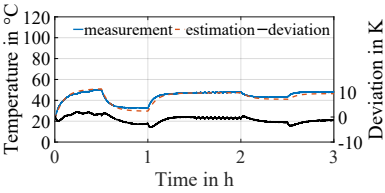
(c) Measured torque in dynamic cycle 1



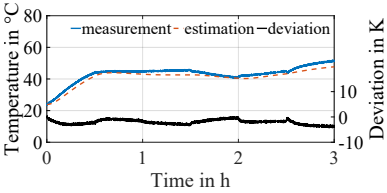
(d) Measured torque in dynamic cycle 2



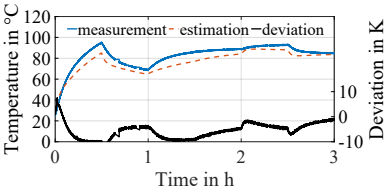
(e) Temperature of stator active winding in dynamic cycle 1



(f) Temperature of stator active winding in dynamic cycle 2

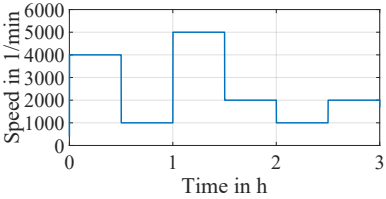


(g) Temperature of shaft in dynamic cycle 1

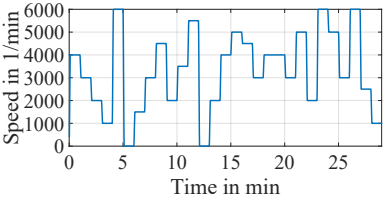


(h) Temperature of rotor active winding in dynamic cycle 2

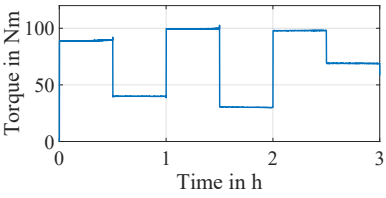
Figure 4.8: Temperature profiles in dynamic drive cycles with 20 °C inlet cooling water temperature. Drive cycle profiles of dynamic cycle 1 on the left column, dynamic cycle 2 on the right column. The measured data in solid blue line, the estimation temperature in dotted red line, the temperature deviation in solid black line



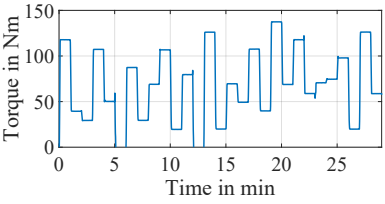
(a) Measured speed in dynamic cycle 3



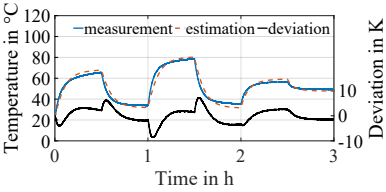
(b) Measured speed in dynamic cycle 4



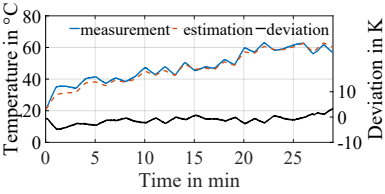
(c) Measured torque in dynamic cycle 3



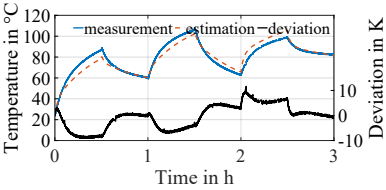
(d) Measured torque in dynamic cycle 4



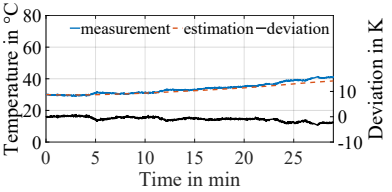
(e) Temperature of stator end winding in dynamic cycle 3



(f) Temperature of stator end winding in dynamic cycle 4



(g) Temperature of rotor end winding in dynamic cycle 3



(h) Temperature of shaft in dynamic cycle 4

Figure 4.9: Temperature profiles in dynamic drive cycles with 20 °C inlet cooling water temperature. Drive cycle profiles of dynamic cycle 3 on the left column, dynamic cycle 4 on the right column. The measured data in solid blue line, the estimation temperature in dotted red line, the temperature deviation in solid black line

Chapter 5

Kalman filter as online EESM thermal state observer

Using the thermal network, the node temperatures of the electrical machine can be estimated based on currents and rotor speed. However, various errors exist in the real motor that are not be fully accounted by the model, including parameter errors of the resistances and capacities, loss error estimation, measurement deviations, initial temperature deviations. Due to these errors, significant deviations between the model and the real motor can occur. Therefore, a state observer is required for temperature monitoring to connect the thermal network with the real motor, so that the unknown errors can be compensated with reference signals.
In this chapter, the errors between the real EESM and the thermal network have been analyzed based on the measurement data. To address these errors, a Kalman filter was implemented as a thermal state observer. First, the thermal network model was represented into standard state-space equations. Subsequently, the general solutions to the state-space equations were derived and implemented. Potential errors during the online model-based temperature estimation were analyzed. In order to minimise these errors, two Kalman filter concepts for the EESM were investigated. In the first concept, the Kalman filter utilized the stator end winding temperature as a reference signal. In the second concept, a data fusion method in the context of Kalman filter was applied, where both the signals from the stator and rotor were used as reference signals. The two Kalman filter

concepts for model error compensation were analyzed and compared based on experimental data.

5.1 State space equations

The differential equation (2.32) in Chapter 2 describes the node temperatures in the EESM thermal network. This equation can be reformulated as a state-space representation as follows:

$$\dot{\vartheta} = A \cdot \vartheta + B \cdot u \tag{5.1}$$

$$y = C \cdot \vartheta + D \cdot u \tag{5.2}$$

where ϑ is the state vector of the system. The variables u and y denote the system's input and output, respectively. A, B, C and D represent the system matrix, input matrix, output matrix and feedthrough matrix of the state-space model.
The input u, as defined in (5.3), comprises the node power losses. The system matrix A, provided in (A.5) in the appendix, includes the thermal resistances and capacities. The input matrix B, shown in (5.4), reflects the thermal capacities of the nodes. The output matrix C determines which outputs are observable through measurement. Based on the Kalman filter design concepts, different output matrices C were implemented, as shown in (5.5). The feedthrough matrix D, defined in (5.6), indicates that input u has no direct effect on the output y.

$$u = \begin{bmatrix} P_{\mathrm{S}} + \dfrac{\vartheta_{\mathrm{C}}}{R_1} \\ P_{\mathrm{SW}} \\ P_{\mathrm{SEW}} + \dfrac{\vartheta_{\mathrm{C}}}{R_4} \\ P_{\mathrm{R}} \\ P_{\mathrm{RW}} \\ P_{\mathrm{REW}} + \dfrac{\vartheta_{\mathrm{C}}}{R_8} \\ P_{\mathrm{SH}} + \dfrac{\vartheta_{\mathrm{A}}}{R_{10}} \end{bmatrix} \tag{5.3}$$

$$B = \begin{bmatrix} \frac{1}{C_{\mathrm{S}}} & 0 & 0 & 0 & 0 & 0 & 0 \\ 0 & \frac{1}{C_{\mathrm{SW}}} & 0 & 0 & 0 & 0 & 0 \\ 0 & 0 & \frac{1}{C_{\mathrm{SEW}}} & 0 & 0 & 0 & 0 \\ 0 & 0 & 0 & \frac{1}{C_{\mathrm{R}}} & 0 & 0 & 0 \\ 0 & 0 & 0 & 0 & \frac{1}{C_{\mathrm{RW}}} & 0 & 0 \\ 0 & 0 & 0 & 0 & 0 & \frac{1}{C_{\mathrm{REW}}} & 0 \\ 0 & 0 & 0 & 0 & 0 & 0 & \frac{1}{C_{\mathrm{Sh}}} \end{bmatrix} \tag{5.4}$$

$$C_t = \begin{bmatrix} 0 \\ 0 \\ 1 \\ 0 \\ 0 \\ 0 \\ 0 \end{bmatrix} \; or \; C_s = \begin{bmatrix} 0 \\ 0 \\ 1 \\ 0 \\ \upsilon_{\mathrm{rw}} \\ \upsilon_{\mathrm{rew}} \\ 0 \end{bmatrix} \tag{5.5}$$

$$D = 0 \tag{5.6}$$

In Fig. 5.1, the correlation between thermal network and the initial required torque is illustrated. For a given required torque, the corresponding currents (i_{d}, i_{q} and i_{r}) are obtained via a LUT, which was calculated offline before. Based on this selected currents, the associated copper and iron losses are calculated. These losses are then used as input u to the thermal network model.
The LUT employed in this study is generated offline by determining the current combination that minimizes losses at each operating point defined by torque and speed. It is evident that both the LUT block, which maps torque to current, and the losses block, which maps current to copper and iron losses, exhibit nonlinear characteristics.
However, for the thermal network in the system boundary as shown in Fig. 5.1, when the losses are directly treated as input u, the system can be regarded as a LPV system. Because certain thermal resistances in the system matrix A are speed dependent and may vary over time. Moreover, under constant speed conditions, the system can also be approximated as a Linear Time-Invariant System

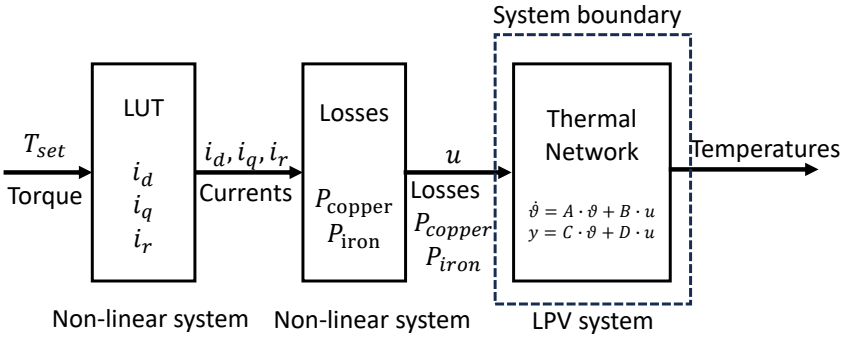


Figure 5.1: Correlation of the thermal network system to required torque

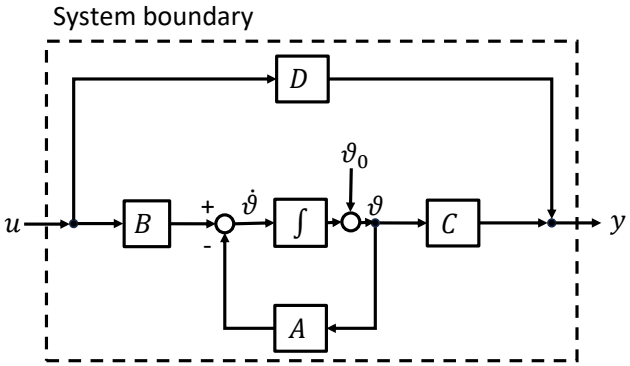


Figure 5.2: Block diagram of the EESM network

(LTI) system, allowing the use of classical LTI-based analysis methods. Fig. 5.2 illustrates the block diagram of the thermal network as state-space representation. Here, the state vector ϑ represents node temperatures, with ϑ_0 denoting the initial temperature, and y being the measurable signal obtained from sensors.

The general solution to (5.1) at time t can be written as [77]:

$$\vartheta(t) = \underbrace{e^{At} \cdot \vartheta_0}_{\text{Zero-input response}} + \underbrace{\int_0^t e^{A(t-\tau)} B \cdot u d\tau}_{\text{zero-state response}} \tag{5.7}$$

where the first term $e^{At} \cdot \vartheta_0$ in (5.7) corresponds to the zero-input response, which represents the node temperatures without input losses. It characterizes the change of the system's initial energy over time. Physically, this can be intuitively understood as the natural dissipation of energy, such as the self-cooling process of a motor without currents input. The second term in (5.7) represents the zero-state response, which describes the system's behavior due to the currents input u. As evident from (5.7), the general solution of the state-space equation is the linear superposition of the zero-input and the zero-state responses, both of which are influenced by the state-transition matrix e^{At}. In certain literature such as [77, 78], the state-transition matrix is also expressed in a simplified from as:

$$\Phi(t) = e^{At} \tag{5.8}$$

with this simplified expression, (5.7) can be rewritten as:

$$\vartheta(t) = \Phi(t) \cdot \vartheta_0 + \int_0^t \Phi(A(t-\tau)) B \cdot u d\tau \tag{5.9}$$

5.2 Concepts of EESM thermal network as Kalman filter

5.2.1 Model errors analysis

In terms of model-based online temperature monitoring, discrepancies between the real motor and model estimation can be attributed to the following factors [78]:

- Process noise p_k: Process noise accounts for deviations, or uncertainties of the real system that are not captured by the model [79, 80]. Since a model cannot perfectly represent a physical system without deviations, process noise

p_k is introduced to represent the uncertainty between the model and the true physical system [79]. It can be mathematically described as:

$$\text{Process noise} : p_\mathrm{k} \sim \mathcal{N}(0,Q) \tag{5.10}$$

where Q is the covariance of the process noise. Setting the process noise involves a trade-off between reliance on the model and reliance on measurements. If Q is set too low, the Kalman filter underestimates rapid changes detected by the sensors, limiting the impact of the feedback on model adjustment. Conversely, if Q is set too high, the filter becomes overly sensitive to measurement noise [79].

- Measurement noise m_k: Measurement noise arises when using sensor data to correct the model's predictions. It allows the Kalman filter to balance between trusting the new measurement and the current model prediction. m_k can be mathematically expressed as:

$$\text{Measurement noise} : m_\mathrm{k} \sim \mathcal{N}(0,R) \tag{5.11}$$

where R is the covariance of the measurement noise. A high R value indicates significant measurement noise, causing the Kalman filter to rely more on the model than on the measurement, and leading to slower response to deviations [79]. The relative values of R and Q determine whether the Kalman filter tends to model estimation or measurement data.

- Initial deviation ε_k: in the absence of sufficient sensor information, the initial state of the system is unknown. The model must assume an initial state, leading to a discrepancy between the assumed and real initial states, defined as the initial deviation:

$$\varepsilon_\mathrm{k} = \hat{\vartheta_0} - \vartheta_0 \tag{5.12}$$

The effects of these errors are analyzed in the subsequent sections by comparing model estimations with a selected test operating point of $3000\,1/\mathrm{min}$ and $70\,\mathrm{N\,m}$.

Process noise and measurement noise

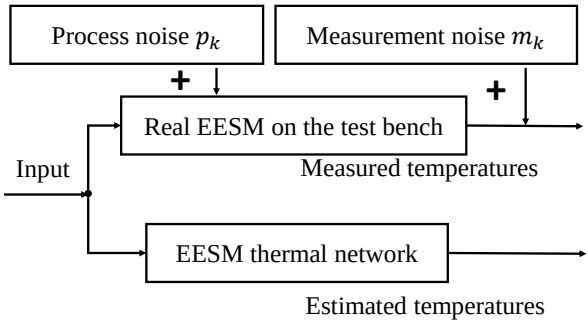
Fig. 5.3 illustrating the impact of process noise and measurement noise on the model estimation by illustrating the stator active winding temperature and rotor active winding temperature from the model and from measurement.
Fig. 5.3 (a) presents a block diagram that schematically depicts the effects of process noise and measurement noise on the model. To minimize the influence of

initial deviation, the thermal network was initialized with the same initial temperatures as the real motor. In the model, process noise aggregates numerous real-world factors that are not explicitly considered, while measurement noise accounts for deviations introduced by sensor inaccuracies. The stator active winding temperature in Fig. 5.3 (b) and the rotor active winding temperature in Fig. 5.3 (c) were selected for comparison. In these figures, the measured temperatures from the test bench are shown as solid blue lines, while the estimated temperatures from the model are shown by the dotted red lines. The deviation between the measured and estimated temperatures is represented by black sloid lines.

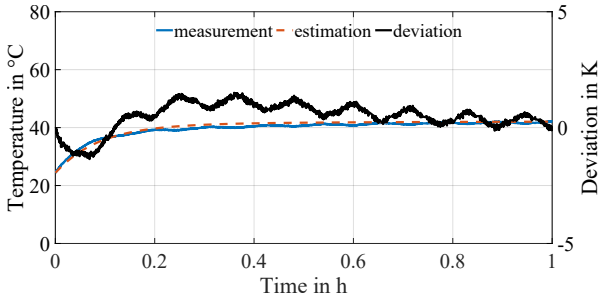
As indicated by the black curves in Fig. 5.3 (b) and Fig. 5.3 (c), the deviation between the model predictions and the measured results can be categorized into two types. The first type is measurement noise, which originates from the inaccuracies of the sensors. In Fig. 5.3 (b) and Fig. 5.3 (c), the measurement noise exhibits higher frequency components. In Fig. 5.3 (b), the fluctuation of the measurement error generated by the Type T thermal sensor from the stator side is $0.2\,\mathrm{K}$. Comparatively, fluctuation in Fig. 5.3 (c) of the Type K thermal sensor produces a larger fluctuation of $1\,\mathrm{K}$ from the rotor side.

The second type of deviation is process noise, which essentially arises from model imperfections. These imperfections may result from inaccurate parameter estimation or from unmodeled effects that are not captured in the model. In Fig. 5.3 (b), it can be observed that the black error curve exhibits a sinusoidal oscillation with an amplitude of approximately $2\,\mathrm{K}$. In Fig. 5.3 (c), regarding the temperature prediction, the model initially overestimates the temperature of the rotor active winding within the time interval of 0 to $0.1\,\mathrm{h}$, and subsequently underestimates it. The resulting error remains within approximately ($3\,\mathrm{K}$). These deviations are attributed to process noise.

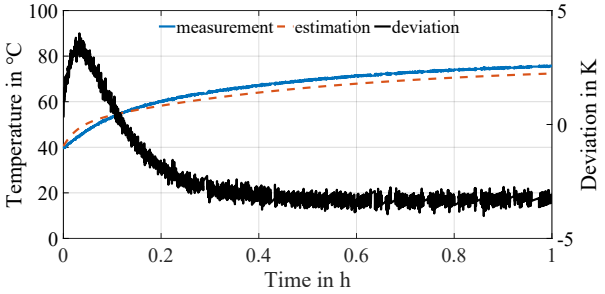
These preliminary estimations of measurement noise and process noise are subsequently used to initialize the measurement noise and process noise covariance matrices (R and Q) in the Kalman Filter.



(a) Block diagram of the comparison



(b) Stator active winding temperature



(c) Rotor active winding temperature

Figure 5.3: Comparison between thermal network and real motor under process and measurement noise at operating point 3000 rpm and 70 N m

Initial deviation

The presence of an unknown initial temperature of online temperature monitoring can lead to discrepancies between model estimations and real measurements. Although it is often assumed that the nodes's initial temperatures are identical to the ambient temperatures, this assumption may not always be true. For instance, consider a scenario where a motor operates for several hours and is then switched off for a short period. When restart, the motor's temperature may differ from the ambient temperature. Taking the initial deviation ε_k into account, the temperature estimation under initial deviation can be mathematically expressed as:

$$\hat{\vartheta}(t) = \Phi(t) \cdot (\vartheta_0 + \varepsilon_\mathrm{k}) + \int_0^t \Phi(A(t-\tau))B \cdot u d\tau \tag{5.13}$$

Consequently, the resulting temperature deviation $\Delta\vartheta$ caused by the initial deviation is derived as:

$$\begin{aligned} \Delta\vartheta &= \hat{\vartheta}(t) - \vartheta(t) \\ \Delta\vartheta &= \Phi(t) \cdot \varepsilon_\mathrm{k} \end{aligned} \tag{5.14}$$

Equation (5.14) indicates that the impact of initial errors on temperature prediction depends on two factors: the magnitude of the initial error ε_k and the system's state-transient matrix Φ. Given a specified initial deviation ε_k, system's convergence properties can be analyzed through the eigenvalues of the state-transition matrix Φ. As simplification, the thermal network, as a LPV system, can be treated as a quasi-LTI system under constant speed conditions. And the eigenvalues of the thermal network were computed at representative speed.

Tab. 5.1 summarizes the eigenvalues of the state-transition matrix Φ at representative speeds of $0.5 * n_\mathrm{corner}$, n_corner, 0.5*n_max and n_max, where n_corner denotes the corner speed and n_max represents the maximum speed of the reference motor.

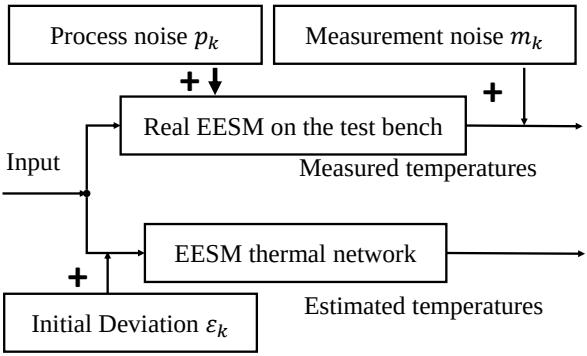
According to Tab. 5.1, all eigenvalues are negative at the selected speeds, confirming that the system is stable. Thus, the temperature deviation due to initial deviation will eventually converge to zero at steady-state. However, the minimal eigenvalues indicate a relatively low converge rate.

As illustrated in Fig. 5.4 (a), an initial deviation of 20 K was introduced to study its influence. The measured temperatures from the test bench are plotted as solid blue lines, while the estimated temperatures from the model are shown as dotted red lines. The deviation between measured and estimated temperature is shown as black solid lines. As seen in both Fig. 5.4 (b) and Fig. 5.4 (c), the temperature deviations converge toward zero over time, confirming the analyti-

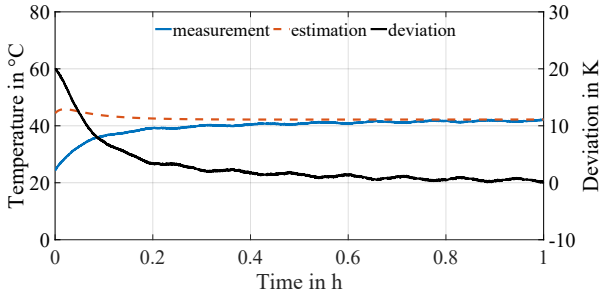
Table 5.1: Eigenvalues of the state-transition matrix Φ at varied speed

0.5*n_{corner}	n_{corner}	0.5*n_{max}	n_{max}
-0.12623	-0.12972	-0.13387	-0.13409
-0.01938	-0.01940	-0.01946	-0.01955
-0.00879	-0.01016	-0.01087	-0.01092
-0.00953	-0.00893	-0.00932	-0.00990
-0.00049	-0.00058	-0.00068	-0.00072
-0.00329	-0.00337	-0.00355	-0.00378
-0.00307	-0.00308	-0.00310	-0.00311

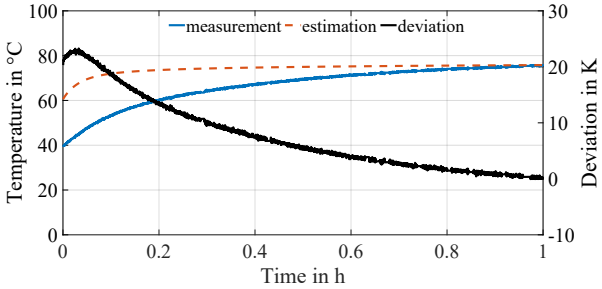
cal conclusions. However, the convergence rate towards zero is slow, requiring approximately one hour for the deviation to convergence completely.
In summary, the analysis of process noise p_{k}, measurement noise m_{k}, and initial deviation ε_{k} shows that each source of error affects the temperature estimation to varying degrees. Measurement noise introduces fluctuations of the measured temperature, whereas process noise lead to deviations between the estimated and the measured temperatures. Although the initial deviation can be eliminated at steady-state, the large inertia of the EESM system (indicated by minimal matrix eigenvalues of the transition matrix Φ) results in a slow convergence speed. Consequently, the integration of additional feedback signals is essential to improve the model's accuracy and to facilitate the detection of abnormal motor conditions. These feedback signals can be incorporated into the Kalman filter to enhance the thermal state estimation of the reference EESM.



(a) Block diagram of the EESM temperature estimation with initial deviation



(b) Stator active winding temperature



(c) Rotor active winding temperature

Figure 5.4: Comparison between thermal network and real motor under initial deviation at operating point 3000 rpm and 70 N m

5.2.2 Model discretization

To implement the EESM thermal network within the Kalman filter framework, the thermal network muss be discretized into a time-discrete system. Various discretization methods can be employed, such as the Euler method [81] or the Runge-Kutta method [82]. In the Euler method, the slope of the linear increase is used to approximate the derivative at time step k, and it can be mathematically expressed as:

$$\dot{\vartheta} \approx \frac{1}{t_\mathrm{s}}(\vartheta[k+1] - \vartheta[k]) \tag{5.15}$$

where t_s describes the sampling time, $\vartheta[k]$ and $\vartheta[k+1]$ represent state vectors of temperatures at time steps k and time step $k+1$, respectively. Consequently, the time-continuous system describes in (5.2) can be discretized using the Euler method as follows:

$$\begin{aligned} \frac{1}{t_\mathrm{s}}(\vartheta[k+1] - \vartheta[k]) &= A\vartheta[k] + Bu[k] \\ \vartheta[k+1] &= (I + At_\mathrm{s})\vartheta[k] + t_\mathrm{s}Bu[k] \end{aligned} \tag{5.16}$$

As shown in (5.16), the Euler method is a computationally inexpensive discretization method. It approximates the derivative at time step k based on the slope of the state vector. However, one limitation of the Euler method is the potential oversimplification of time-continuous systems, which can impact model accuracy. To address this, a more accurate discretization method, the fourth-order Runge-Kutta method, is also considered for comparison. In the fourth-order Runge-Kutta method, the time interval t_s from time k to time $k+1$ is divided into four equal sub-intervals, each corresponding to derivatives k_1, k_2, k_3 and k_4 as shown in (5.17). This method improves the accuracy of the discretised system by separately calculating the derivatives at different points within the time interval. However, this increased accuracy comes at the cost of greater computational complexity. Therefore, a trade off between the computational effort and the acceptable model accuracy must be carefully evaluated.

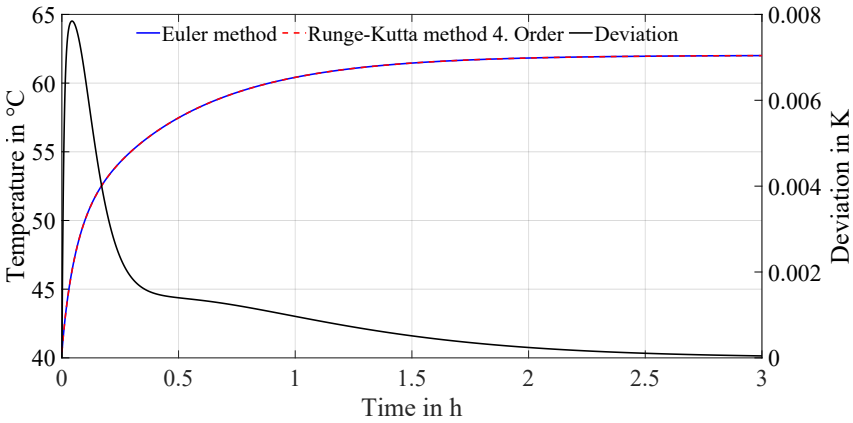


Figure 5.5: Comparison between time continuous thermal network with Euler and Runge-Kutta method 4. Order, rotor active winding temperature by the operating point 70 Nm and 3000 1/min as demonstration

$$
\begin{aligned}
&f : A(n) \cdot \vartheta + B(n) \cdot u(\vartheta_r, n, I) \\
&\vartheta[k+1] = \vartheta + \frac{t_\mathrm{s}}{6}(k_1 + 2k_2 + 2k_3 + k_4) \\
&k_1 = f(t_k + \vartheta_k) \\
&k_2 = f(t_k + \frac{t_\mathrm{s}}{2}, \vartheta_k + \frac{t_\mathrm{s}}{2}k_1) \\
&k_3 = f(t_k + \frac{t_\mathrm{s}}{2}, \vartheta_k + \frac{t_\mathrm{s}}{2}k_2) \\
&k_4 = f(t_k + t_\mathrm{s}, \vartheta_k + t_\mathrm{s}k_3)
\end{aligned}
\tag{5.17}
$$

As illustrated in Fig. 5.5, a comparison is made between the node temperature calculated using Euler and Runge-Kutta methods at the operating point 3000 1/min and 70 Nm. The results indicate that the deviation between the two methods exhibits oscillations during the transient phase before converging towards 0 K in the steady-state region. The range of deviation is minimal, varying between 0 K and 0.008 K. Given that the Euler method demands lower computational effort while maintaining an acceptable level of accuracy, it is selected to discretize the time-continuous thermal network of EESM. Following discretiza-

tion, time continuous thermal network in (5.2) can be discretized as:

$$\begin{aligned} \vartheta[k+1] &= A_d \cdot \vartheta[k] + B_d \cdot u[k] \\ y[k+1] &= C \cdot \vartheta[k] + D \cdot u[k] \end{aligned} \tag{5.18}$$

where $\vartheta[k+1]$ and $\vartheta[k]$ are the state vectors in time step $k+1$ and time step k, respectively, and $u[k]$ and $y[k]$ denote the system input and output at time step k. Matrices A_d, B_d and C represent the discrete system matrix, input matrix and output matrix, respectively. D is zero, as explained in section 5.1. The discretized thermal network will be used for the Kalman filter.

5.2.3 Kalman filter introduction

The Kalman filter is based on a time-discrete system derived from a time-continuous model. By considering the evolution of each measurement over time and incorporating noise distributions at each time step, the Kalman filter provides a more accurate estimation of unknown variables compared to approaches that rely solely on individual measurements [83]. This advanced filtering technique is named after Rudolf Kalman, the principal inventor, who published his article in 1960 [84]. Through his research, the Kalman filter enabled accurate estimation of system states from noisy and partially redundant measurements. A key advantage of the Kalman filter over other stochastic estimation methods is its iterative structure, which makes it particularly well-suited for real-time applications [83]. The block diagram of the classic Kalman filter is shown in Fig. 5.6. The core component of the filter is the discretized thermal network, highlighted in blue region, whose mathematical description is given in (5.18). The overall structure of the Kalman filter, including model estimation and measurements from the physical system, is depicted in the grey area. Utilizing the Kalman gain K, the measurement signal is fed back into the system to reduce the deviation between the model and the real physical process.
In terms of signal processing, the Kalman filter operates in two main steps. The first step is prediction, described as follows:

Prediction

$$\hat{\vartheta}[k+1]^- = A_d \cdot \hat{\vartheta}[k] + B_d \cdot u[k] \tag{5.19}$$

$$\hat{P}[k+1]^- = A_d \cdot \hat{P}[k] \cdot A_d^T + Q[k] \tag{5.20}$$

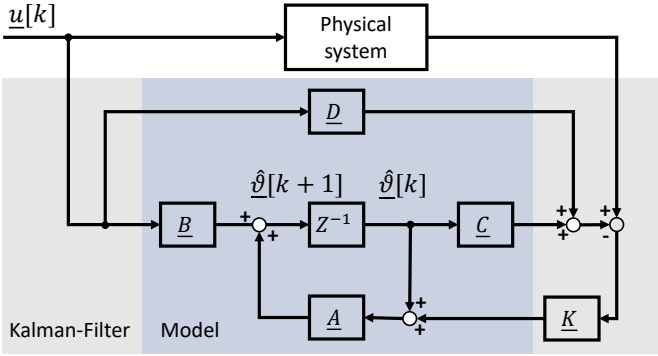


Figure 5.6: Block diagram of classic Kalman filter [83]

where the covariance matrix P represents the expected estimation uncertainty, and Q denotes the process noise covariance of the dynamic system. During the prediction step, the state of the system from time step k to $k+1$ is estimated. The second step is update, given by:

Update

$$K[k+1] = \hat{P}[k+1]^{-} C^{T} \left\{ C \cdot \hat{P}[k+1]^{-} C^{T} + R[k] \right\}^{-1} \tag{5.21}$$

$$\hat{\vartheta}[k+1] = \hat{\vartheta}[k+1]^{-} + K[k+1] \left\{ y[k+1] - C \cdot \hat{\vartheta}[k+1]^{-} \right\} \tag{5.22}$$

$$\hat{P}[k+1] = \{\underline{I} - K[k+1] \cdot C\} \cdot \hat{P}[k+1]^{-} \tag{5.23}$$

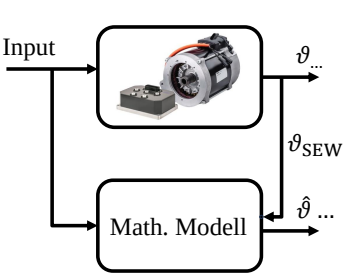
where K is the Kalman gain. C is the output matrix, R is the measurement covariance matrix, and I is the identity matrix. During the update phase, the predicted state is corrected based on the latest measurement, and the state covariance matrix P is updated accordingly.
In addition to the classic Kalman filter, there are extended variants such as the adaptive Kalman filter and the non-linear Kalman filter. However, as the classic Kalman filter already fulfils the requirements of the system, extended versions are not adopted in this thesis in order to minimize computational complexity.

5.2.4 EESM Kalman filter concepts and validations

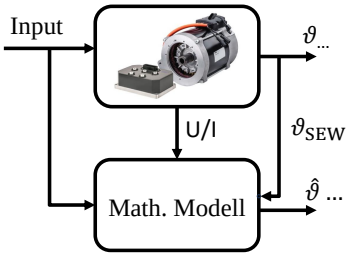
The feedback signals for the Kalman filter can be obtained from two sources: direct measurement or indirect online parameter estimation. Direct measurement offers a straightforward and robust means of obtaining component temperatures. However, it requires additional sensor installations, which can be costly and challenging, particularly when targeting critical areas such as rotating rotor parts. Alternatively, indirect online parameter estimation methods can be used to estimate electrical machine parameters. These methods include current and voltage injection [85, 86], high frequency signal injection [87, 88] or Position-Offset-based Parameter Estimation (POPE) [89], as summarized in [90].
Based on these feedback signals, a Kalman filter estimating motor thermal state can be implemented. In [91], motor frame temperature was utilised as feedback temperature to minimise the initial deviation between the PMSM model and the real machine. However, the significant temperature gradient between the motor frame and internal components (such as the stator active winding) can be a drawback, especially in motors equipped with water-jacket cooling systems. In [92], a combined direct and indirect temperature estimation approach for PMSM was studied. A temperature sensor integrated into the stator slot winding allows direct measurement of the active winding temperature, while rotor magnet temperatures are estimated using an online parameter identification approach based on the Permanet Magnet Temperature Observer (PMTO) method [92–96]. In this configuration, the Kalman filter enables PMSM temperature monitoring by fusing direct and indirect temperature estimations.
In this study, two Kalman filter concepts were investigated for EESM temperature monitoring, as illustrated in Fig. 5.7. Fig. 5.7 (a) presents concept A, where the Kalman filter utilizes the feedback signal of the stator end winding temperature ϑ_{SEW}. The corresponding output matrix C_t is defined as:

$$C_t = \begin{bmatrix} 0 \\ 0 \\ 1 \\ 0 \\ 0 \\ 0 \\ 0 \end{bmatrix} \tag{5.24}$$

where the value "1" in the third position indicates that the stator end winding temperature is measurable.



(a) Kalman filter concept A with feedback of stator end winding temperature



(b) Kalman filter concept B with feedback of stator end winding temperature and rotor voltage and current

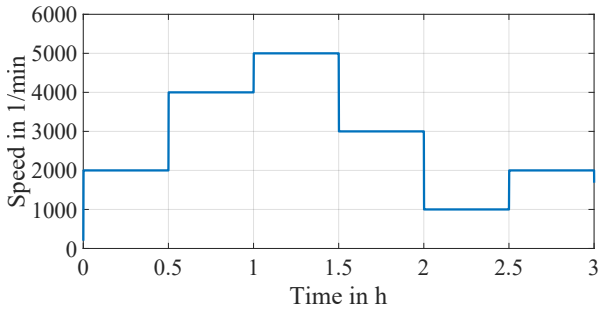
Figure 5.7: Concepts of Kalman filter for EESM [E2]

Fig. 5.7 (b) illustrates concept B, which integrates two types of feedback signals: the stator end winding temperature ϑ_{SEW} from the stator side, and the rotor winding voltage and current signals from the rotor side. The corresponding output matrix C_s is defined as:

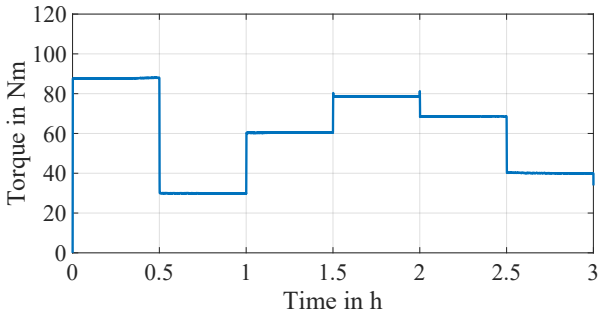
$$C_s = \begin{bmatrix} 0 \\ 0 \\ 1 \\ 0 \\ \upsilon_{\text{rw}} \\ \upsilon_{\text{rew}} \\ 0 \end{bmatrix} \tag{5.25}$$

where the third column with "1" corresponds to the stator end winding measurement, while the fifth and sixth columns represent the mass ratio of the rotor active winding (υ_{rw}) and rotor end winding (υ_{rew}) to the overall rotor winding. Through a linear mass relationship, the temperatures of the rotor active winding and the rotor end winding can also be derived from the measured data using the Kalman filter. The relationship can be mathematically expressed as:

$$\vartheta_{r,avg} = \vartheta_{\text{R}} \cdot \upsilon_{\text{rw}} + \vartheta_{\text{REW}} \cdot \upsilon_{\text{rew}} \tag{5.26}$$



(a) Speed profile



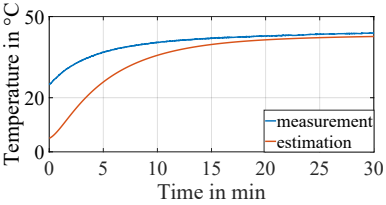
(b) Torque profile

Figure 5.8: Thermal cycle for testing of Kalman filter concept A and concept B

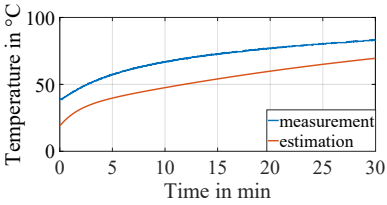
For better Comparison, both Kalman concepts were validated through a identical thermal cycle, whose torque and speed profiles are shown in Fig. 5.8. The entire test lasted for three hours, with the operating point changed every half hour. The primary objective of the experiments was to validate the effectiveness of the Kalman filters in estimating node temperatures. To this end, an initial deviation $\varepsilon_{\mathrm{k}} = 20K$ between the thermal network and the real motor was intentionally introduced. The model's convergence speed toward the real machine behavior was then monitored. By comparing the temperature estimations with and without Kalman filter, the effectiveness of each Kalman filter concept was studied.

Kalman filter concept A

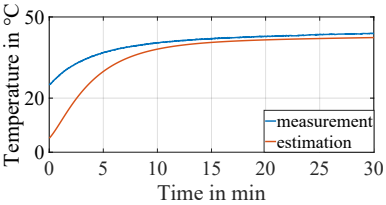
In Kalman filter concept A, the stator end winding temperature is utilised as the reference signal of the state observer. To better compare the model convergence with and without the Kalman filter feedback, the test results for the first half hour are presented in Fig. 5.9, while the full test results can be found in Fig. A.1 in the appendix.
Fig. 5.9 shows the temperatures of the stator active winding and the rotor end winding. For comparison, Fig. 5.9 (a) - (b) present the estimated temperature without Kalman filter feedback, while Fig. 5.9 (c) - (d) show the estimations with Kalman filter feedback. Fig. 5.9 (e) - (f) show the deviation of estimated temperatures from the stator and rotor sides, respectively. Comparing Fig. 5.9 (a), Fig. 5.9 (c) and Fig. 5.9 (e) from the stator side, it is evident that the model estimation converges toward real motor over time, regardless of presence of Kalman feedback. However, Fig. 5.9 (e) shows that the Kalman filter significantly accelerates this convergence.
On the rotor side, comparison of Fig. 5.9 (b), Fig. 5.9 (d) and Fig. 5.9 (f) reveals that the convergence speed is nearly identical, with or without Kalman filter feedback. Thus, Kalman filter concept A does not significantly enhance convergence on the rotor side.
This observation can be explained by analyzing the node loss sensitivity, as illustrated in Fig. 5.10 and Fig. 5.11. Both figures present sensitivity analysis for the stator end winding loss (P_3) and rotor winding loss ($P_5 + P_6$), respectively (refer to Fig. 2.10 for loss and node definitions). Sensitivity analysis quantifies the impact of variations in specific node losses on the overall thermal network, thus assessing the effectiveness of Kalman filter feedback.
Fig. 5.10 compares the influence of halved, normal and doubled losses of the stator end winding on the node temperatures. It is evident that variations in stator end winding losses significantly affect the stator-side nodes but have minimal impact on rotor node temperatures. Conversely, Fig. 5.11 shows that rotor winding losses predominantly influence rotor-side nodes, with negligible effects on the stator side.
Combining Fig. 5.10 and Fig. 5.11, it can be concluded that the high thermal resistance of the air gap results in a weak thermal coupling between the stator and the rotor. Consequently, losses variations on one side of the machine have minimal influence on the other side. This weak coupling limits the ability of the Kalman filter to correlate stator and rotor temperatures effectively. Therefore, to achieve more accurate motor temperature observation, feedback signals from both the stator and rotor sides are necessary.



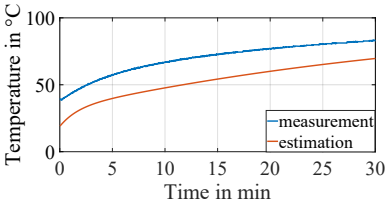
(a) Stator active winding temperature estimation without Kalman filter



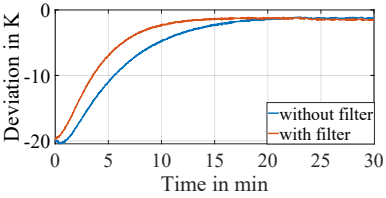
(b) Rotor end winding temperature estimation without Kalman filter



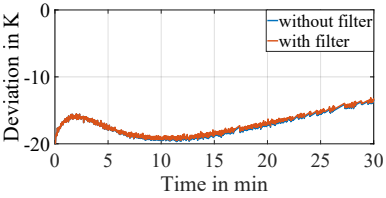
(c) Stator active winding temperature estimation with Kalman filter



(d) Rotor end winding temperature estimation with Kalman filter



(e) Deviation comparison of stator active winding



(f) Deviation comparison of rotor end winding

Figure 5.9: Comparison of the model estimation with and without Kalman filter concept A with assumed initial deviation $\varepsilon_k = 20K$. Measurement in solid blue line and Model estimation in solid red line.

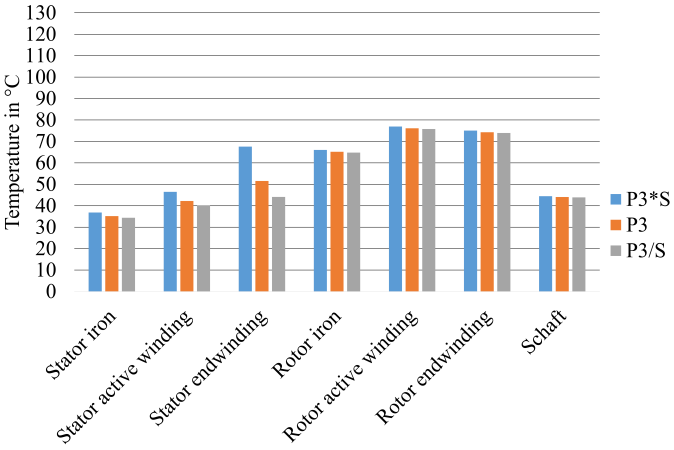


Figure 5.10: Sensitivity analysis of the stator end winding power losses with $S = 2$ based on the steady temperatures at 3000 1/min and 70 Nm

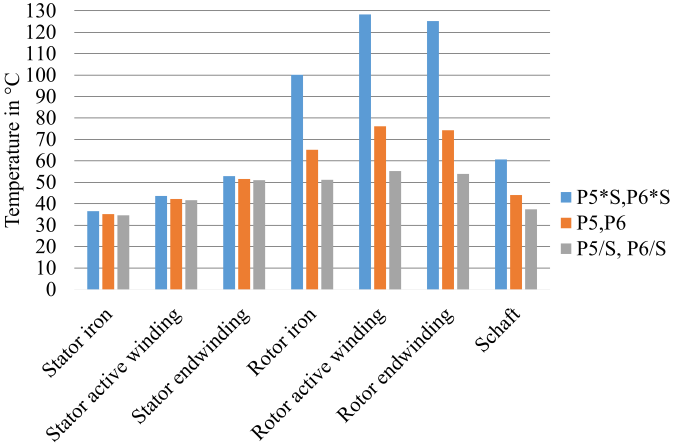


Figure 5.11: Sensitivity analysis of the rotor winding power losses with $S = 2$ based on the steady temperatures at 3000 1/min and 70 Nm

Kalman filter concept B

In Kalman filter concept B, the Kalman filter utilizes the reference signals from the stator end winding temperature and the rotor winding current and voltage, as illustrated in Fig. 5.7 (b). The feasibility of the Kalman filter concept B is first derived mathematically.
Under electrical steady-state conditions, where the stator and rotor winding currents remain constant, the electrical resistance of the motor can be calculated as:

$$u_{\mathrm{r}} = R_{\mathrm{e,r}} \cdot i_{\mathrm{r}} \tag{5.27}$$

where u_{r} and i_{r} denote the rotor winding voltage and the current in steady-state, respectively, and $R_{\mathrm{e,r}}$ denotes the rotor winding electrical resistance. Based on the electrical resistance, the average rotor winding temperature can be estimated as:

$$R_{\mathrm{e,r}} = R_{\mathrm{e,r0}} \cdot [1 + \alpha \cdot (\vartheta_{\mathrm{r,avg}} - \vartheta_{\mathrm{r,avg,0}})] \tag{5.28}$$

where $R_{\mathrm{e,r0}}$ is the rotor resistance at the pre-defined reference temperature, α is the copper temperature-dependent coefficient, $\vartheta_{\mathrm{r,avg}}$ is the average rotor winding temperature and $\vartheta_{\mathrm{r,avg,0}}$ is the reference temperature. Thus, by using (5.27) and (5.28), the rotor average winding temperature can be estimated and incorporated into the Kalman filter. However, this estimation is only valid under electrical steady-state conditions. Under transient conditions, an additional voltage component is induced, which can be mathematically expressed as:

$$u_{\mathrm{r}} = R_{\mathrm{e,r}} \cdot i_{\mathrm{r}} + \frac{d}{dt}\Psi_{\mathrm{r}} \tag{5.29}$$

where Ψ_{r} represents the rotor flux linkage, which can be calculated as:

$$\Psi_{\mathrm{r}} = M_{\mathrm{dr}} \cdot i_{\mathrm{d}} + L_{\mathrm{r}} \cdot i_{\mathrm{r}} \tag{5.30}$$

where M_{dr} is the mutual inductance between the stator d-axis and the rotor, i_{d} is the stator current in the d-axis of the d/q coordinate system, L_{r} is the rotor inductance, and i_{r} is the rotor winding current.
Equation (5.29) indicates that rotor winding temperature estimation based on electrical resistance can not be reliably during transient conditions due to the additional induced voltage $\frac{d}{dt}\Psi_{\mathrm{r}}$.

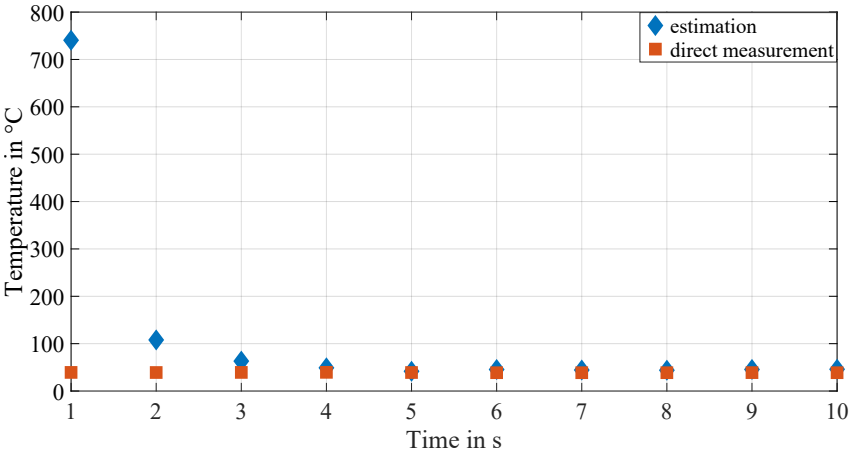


Figure 5.12: Distortion of rotor winding temperature estimation based on the rotor winding voltage and current in the first 10s of the thermal cycle in Fig. 5.8 (a) and Fig. 5.8 (b)

Fig. 5.12 presents the first 10 seconds of the rotor average winding temperature estimation during the thermal cycle. The entire test lasted three hours, with the torque and speed profiles summarized in Fig. 5.8. During the first five seconds, the winding currents ramped up to the target values to achieve the required torque. In the figure, red points indicate direct measurements of the rotor active winding temperature, while blue points represent the estimated temperatures. Significant distortion in the estimation can be observed during the initial 5 seconds.
To mitigate this distortion during transient states, a pre-processing algorithm was integrated into Kalman filter concept B:

$$\begin{aligned} |i_\mathrm{d}[t] - i_\mathrm{d}[t-1]| &> 1 \\ |i_\mathrm{r}[t] - i_\mathrm{r}[t-1]| &> 0.1 \end{aligned} \tag{5.31}$$

$$C_t = \begin{bmatrix} 0 \\ 0 \\ 1 \\ 0 \\ 0 \\ 0 \\ 0 \end{bmatrix} \; or \; C_s = \begin{bmatrix} 0 \\ 0 \\ 1 \\ 0 \\ \upsilon_{\mathrm{rw}} \\ \upsilon_{\mathrm{rew}} \\ 0 \end{bmatrix} \tag{5.32}$$

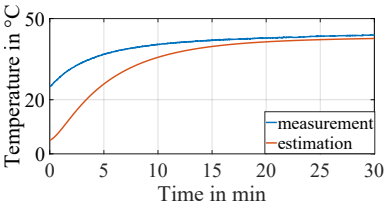
In (5.31), by comparing the differences between i_{d} and i_{r} with the previous time step, transient changes of these currents can be detected. If either condition in (5.31) is satisfied, it is deduced that the rotor winding temperature estimation is distorted. Consequently, the transient output matrix C_{t} is employed in the Kalman filter instead of the steady-state output matrix C_{s}, thereby excluding distorted rotor-side signals during transient periods.

For better Comparison, Kalman concept B was validated using identical thermal cycle as concept A, whose speed and torque profiles are provided in Fig. 5.8. The three-hour test included operating point changes every half hour. An initial temperature deviation of $\varepsilon_{\mathrm{k}} = 20K$ was introduced between the model and the real motor.

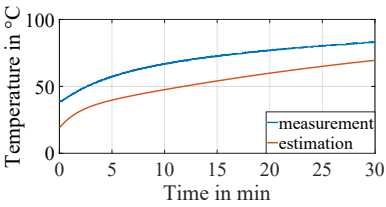
Fig. 5.13 illustrates the convergence of the model to the real motor during the first 30 minutes. Stator active winding and rotor end winding temperatures are compared in the figures. As comparison, Fig. 5.13 (a) - (b) show the temperature estimation without Kalman filter feedback, while Fig. 5.13 (c) -(d) depict the estimation with Kalman filter feedback. In each figure, blue solid lines represent measured temperatures, and red dashed lines represent estimated temperatures. Fig. 5.13 (e) - (f) show the corresponding estimation deviations for the stator and rotor sides, respectively.

By comparing Fig. 5.13 (a), Fig. 5.13 (c) and Fig. 5.13 (e) for the stator side, and Fig. 5.13 (b), Fig. 5.13 (d) and Fig. 5.13 (f) for the rotor side, it is evident that Kalman filter concept B significantly accelerates model convergence on both the stator and rotor sides.

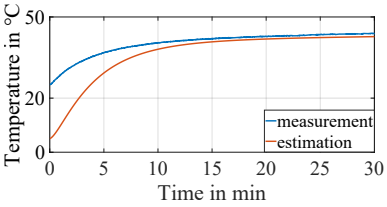
Thus, it can be concluded that using Kalman filter concept B enables more accurate and faster observation of the motor's thermal state, and that deviations between model and measurements can be compensated more rapidly through Kalman feedback signals.



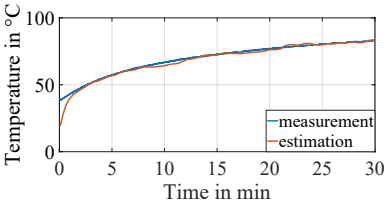
(a) Stator active winding temperature estimation without Kalman filter



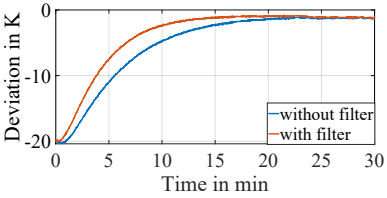
(b) Rotor end winding temperature estimation without Kalman filter



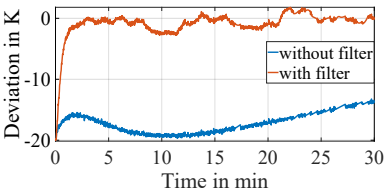
(c) Stator active winding temperature estimation with Kalman filter



(d) Rotor end winding temperature estimation with Kalman filter



(e) Deviation comparison of stator active winding



(f) Deviation comparison of rotor end winding

Figure 5.13: Comparison of the model estimation with and without Kalman filter concept B with assumed initial deviation $\varepsilon_k = 20K$ in the first half hour. Measurement in solid blue line and Model estimation in solid red line.

Chapter 6

Model-based thermal management for EESM

Motor control algorithms embedded within the control unit are responsible for determining the operating point of the motor. A critical aspect of these algorithms is thermal management, which continuously monitors the motor temperature to ensure optimal performance and prevent overheating. Thermal management strategies are typically categorized into passive and active methods.

Passive thermal management approaches [47, 48] apply torque derating only after critical temperature thresholds are reached. For instance, in [48], a simplified thermal network functions is built as a relay to estimate the motor temperatures. Once the temperature exceeds the maximum allowable limit, the motor is shut down. In [47], instead of the maximum allowable temperature, an overload duration is predefined for each operating point. If the overload persists beyond the allowed time, torque derating is triggered.

In contrast to passive thermal management, active thermal management reduces torque in advance to prevent the motor from reaching critical temperatures. Model Predictive Control (MPC), integrated with a thermal network, has been employed to estimate future thermal behavior and apply advance derating strategies accordingly [37, 51].

To augment existing active thermal management approaches, this work proposes a novel algorithm that reduces hot-spot temperatures without compromising torque output. Utilizing estimated temperatures from the thermal network, a thermal balance is achieved among various motor components, thereby mitigat-

ing localized overheating. This allows torque derating to be postponed or even avoided, depending on the thermal conditions of the electrical machine.

6.1 EESM control theory

The torque control of the EESM is implemented based on Field-Oriented Control (FOC) theory, which fundamentally relies on coordinate system transformations. These transformations simplify the representation of motor variables such as voltages and currents in the time domain, enabling more intuitive and decoupled control.

6.1.1 Coordinate system transformation

The motor variables can be expressed in three primary coordinate systems, as illustrated in Fig. 6.1:

- abc coordinate system: a stator-fixed coordinate system frame comprising three axes shifted by $120°$, directly corresponding to the motor's three-phase winding configuration. This system provides the foundational basis for analyzing time-domain behavior of motor variables.
- $\alpha\beta$ coordinate system: a two-axis orthogonal stator-fixed system obtained from the abc system via the Clarke transformation. It reduces dimensional complexity and facilitates easier analysis of three-phase systems.
- dq coordinate system: a rotating orthogonal coordinate system aligned with the rotor's magnetic field, derived from the $\alpha\beta$ system using the Park transformation. This system decouples the control of torque and flux, thereby enabling efficient FOC implementation.

abc coordinate system

In the abc coordinate system, the three-phase stator currents can be described as:

$$\begin{aligned} i_{\mathrm{a}}(t) &= \hat{i}_{\mathrm{s}} \cdot \sin(\omega t) \\ i_{\mathrm{b}}(t) &= \hat{i}_{\mathrm{s}} \cdot \sin(\omega t - 2\pi/3) \\ i_{\mathrm{c}}(t) &= \hat{i}_{\mathrm{s}} \cdot \sin(\omega t - 4\pi/3) \end{aligned} \tag{6.1}$$

where $\hat{i}_{\mathrm{s}}$ is the peak stator current, ω is the stator electrical angular frequency.

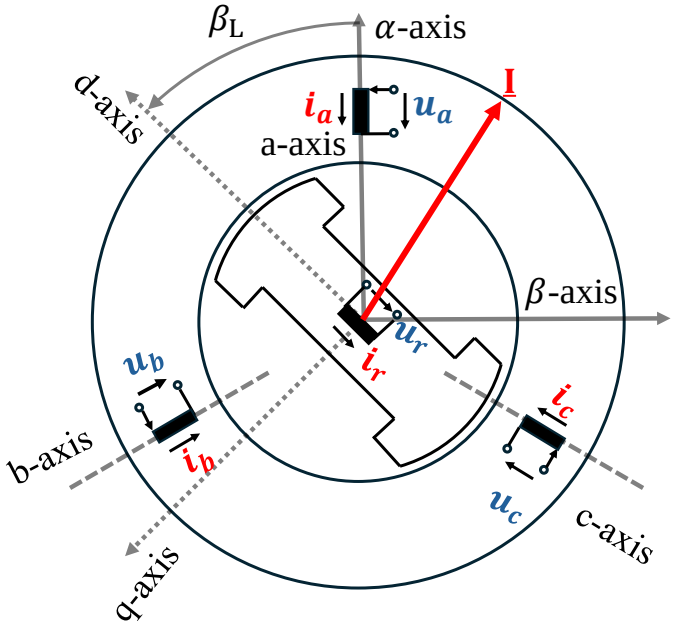


Figure 6.1: Winding system of the EESM [97]

The corresponding phase voltages are given by:

$$\begin{aligned} u_{\mathrm{a}}(t) &= R_{\mathrm{e,s}} \cdot i_{\mathrm{a}} + \frac{d\Psi_{\mathrm{a}}}{dt} \\ u_{\mathrm{b}}(t) &= R_{\mathrm{e,s}} \cdot i_{\mathrm{b}} + \frac{d\Psi_{\mathrm{b}}}{dt} \\ u_{\mathrm{c}}(t) &= R_{\mathrm{e,s}} \cdot i_{\mathrm{c}} + \frac{d\Psi_{\mathrm{c}}}{dt} \end{aligned} \tag{6.2}$$

where $R_{\mathrm{e,s}}$ is the stator resistance. Ψ_{a}, Ψ_{b} and Ψ_{c} are the flux linkages of the motor phases.

$\alpha\beta$ coordinate system

In the $\alpha\beta$ coordinate system, the stator current is represented as the vector combination of the phase currents along the a, b and c axes as shown in (6.3). The geometric phase shifts among these currents are captured using the complex exponential factors $e^{j\frac{2}{3}\pi}$ and $e^{j\frac{4}{3}\pi}$, which facilitates the transformation from the abc to the $\alpha\beta$ coordinate system.

$$\begin{aligned} \underline{a} &= e^{j\frac{2}{3}\pi} = -\frac{1}{2} + j\frac{\sqrt{3}}{2} \\ \underline{a}^2 &= e^{j\frac{4}{3}\pi} = -\frac{1}{2} - j\frac{\sqrt{3}}{2} \\ \underline{I} &= \frac{2}{3} \cdot (i_{\mathrm{a}}(t) + \underline{a} \cdot i_{\mathrm{b}}(t) + \underline{a}^2 \cdot i_{\mathrm{c}}(t)) \end{aligned} \tag{6.3}$$

In matrix form, the transformation becomes:

$$\begin{bmatrix} i_\alpha \\ i_\beta \end{bmatrix} = \frac{2}{3} \cdot \begin{bmatrix} 1 & -\frac{1}{2} & -\frac{1}{2} \\ 0 & \frac{\sqrt{3}}{2} & -\frac{\sqrt{3}}{2} \end{bmatrix} \cdot \begin{bmatrix} i_{\mathrm{a}} \\ i_{\mathrm{b}} \\ i_{\mathrm{c}} \end{bmatrix} \tag{6.4}$$

The corresponding voltage equations are:

$$\begin{aligned} u_\alpha &= R_{\mathrm{e,s}} \cdot i_\alpha + \frac{d\Psi_\alpha}{dt} \\ u_\beta &= R_{\mathrm{e,s}} \cdot i_\beta + \frac{d\Psi_\beta}{dt} \end{aligned} \tag{6.5}$$

dq coordinate system

Based on the $\alpha\beta$ coordinate system, the Park transformation is applied to convert the stationary $\alpha\beta$ coordinate system into a rotating dq coordinate system aligned with the rotor flux:

$$\begin{bmatrix} i_{\mathrm{d}} \\ i_{\mathrm{q}} \end{bmatrix} = \begin{bmatrix} \cos\beta_{\mathrm{L}} & \sin\beta_{\mathrm{L}} \\ -\sin\beta_{\mathrm{L}} & \cos\beta_{\mathrm{L}} \end{bmatrix} \cdot \begin{bmatrix} i_\alpha \\ i_\beta \end{bmatrix} \tag{6.6}$$

Within the rotating dq coordinate system, the d-axis aligned with the rotor flux, while the q-axis is orthogonal to the d-axis. As the dq coordinate system coordinate system rotates synchronously with the rotor, its angular speed is given by:

$$\omega = z_{\mathrm{p}} \cdot \Omega \tag{6.7}$$

where Ω is the mechanical angular speed, and z_{p} is the motor pol pairs. The rotor electrical angle β_L is expressed as:

$$\beta_{\mathrm{L}} = \beta_{\mathrm{L},0} + \int_0^t \omega(\beta_{\mathrm{L}}) d\beta_{\mathrm{L}} \tag{6.8}$$

The voltage equations of the EESM in the dq coordinate system are:

$$\begin{aligned} u_{\mathrm{d}} &= R_{\mathrm{e,s}} \cdot i_{\mathrm{d}} + \frac{d\Psi_{\mathrm{d}}}{dt} - \omega \cdot \Psi_{\mathrm{q}} \\ u_{\mathrm{q}} &= R_{\mathrm{e,s}} \cdot i_{\mathrm{q}} + \frac{d\Psi_{\mathrm{q}}}{dt} + \omega \cdot \Psi_{\mathrm{d}} \\ u_{\mathrm{r}} &= R_{\mathrm{e,r}} \cdot i_{\mathrm{r}} + \frac{d\Psi_{\mathrm{r}}}{dt} \end{aligned} \tag{6.9}$$

under electrical steady-state conditions, time derivatives of the flux linkage can be neglected, (6.9) is simplified as:

$$\begin{aligned} u_{\mathrm{d}s} &= R_{\mathrm{e,s}} \cdot i_{\mathrm{d}} - \omega \cdot \Psi_{\mathrm{q}} \\ u_{\mathrm{q}s} &= R_{\mathrm{e,s}} \cdot i_{\mathrm{q}} + \omega \cdot \Psi_{\mathrm{d}} \\ u_{\mathrm{r}s} &= R_{\mathrm{e,r}} \cdot i_{\mathrm{r}} \end{aligned} \tag{6.10}$$

In (6.10), the flux linkage can be defined as:

$$\begin{aligned} \Psi_{\mathrm{d}} &= L_{\mathrm{d}} \cdot i_{\mathrm{d}} + M_{\mathrm{dr}} \cdot i_{\mathrm{r}} \\ \Psi_{\mathrm{q}} &= L_{\mathrm{q}} \cdot i_{\mathrm{q}} \\ \Psi_{\mathrm{r}} &= L_{\mathrm{r}} \cdot i_{\mathrm{r}} + M_{\mathrm{dr}} \cdot i_{\mathrm{d}} \end{aligned} \tag{6.11}$$

where L_{d}, L_{q} are self-inductances and L_{r} is the mutual inductance between the stator d-axis and rotor. Self-inductances can be further decomposed into leakage and main inductances:

$$\begin{aligned} L_{\mathrm{d}} &= L_{\sigma} + L_{\mathrm{hd}} = L_{\sigma} + M_{\mathrm{dr}} \\ L_{\mathrm{q}} &= L_{\sigma} + L_{\mathrm{hq}} \end{aligned} \tag{6.12}$$

The main inductances represent the primary magnetic coupling between windings, while the stray inductances account for leakage paths. Based on the

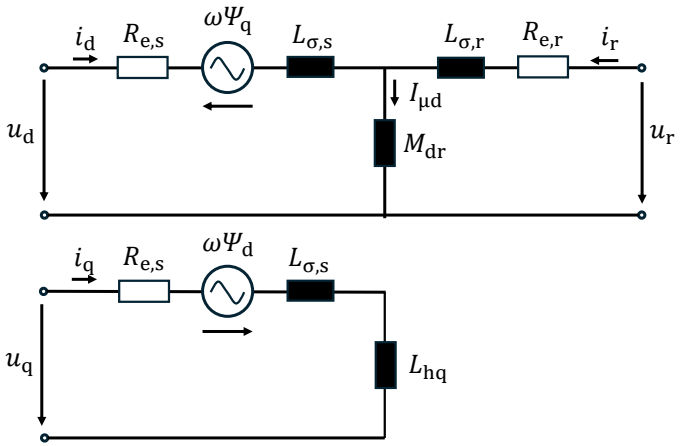


Figure 6.2: Equivalent circuit diagram of the EESM [97]

preceding analytical equations, an equivalent circuit is represented for the d- and q-axes, as illustrated in Fig. 6.2.
Finally, the electromagnetic torque is expressed as:

$$T = \frac{3}{2} z_p \cdot (M_{dr} \cdot i_r \cdot i_q + (L_d - L_q) \cdot i_d \cdot i_q) \tag{6.13}$$

6.1.2 EESM torque control

Fig. 6.3 illustrates the EESM torque control architecture using a block diagram, which highlights the control structure and signal flow. The reference currents $i_{d,ref}$, $i_{q,ref}$ and $i_{r,ref}$ stored in a LUT within the control unit, define the desired operating point. These reference currents are used as inputs to Proportional-Integral (PI) controllers, which compute the corresponding voltage references $u_{d,ref}$ and $u_{q,ref}$. Using the measured rotor position β_L, the inverse Park and Clarke transformations are applied to convert the voltages references $u_{d,ref}$, $u_{q,ref}$ from the rotating dq coordinate system to phase voltages u_a, u_b and u_c in the abc coordinate system. The rotor voltage reference $u_{r,ref}$ is separately computed via a PI controller based on $i_{r,ref}$. These stator and rotor voltages are then applied through the power electronics by controlling the IGBT switching signals. In the

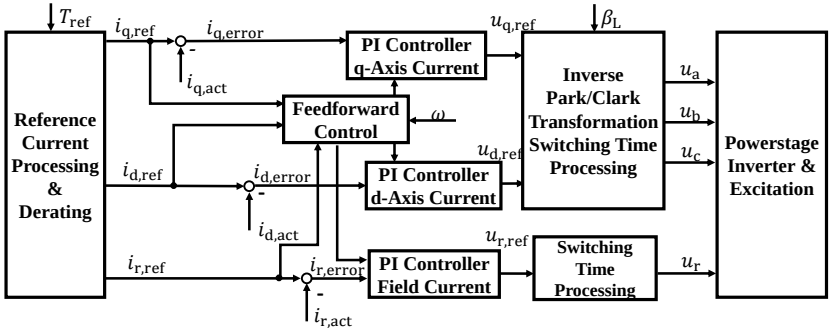


Figure 6.3: Torque control of the EESM [46]

Power stage, the actual phase currents $i_{a,act}$, $i_{b,act}$, $i_{c,act}$ and rotor field current $i_{r,act}$ are measured using current sensors. The stator currents are subsequently transformed using Park and Clarke transformations to obtain the actual dq currents $i_{d,act}$ and $i_{q,act}$. These measured currents are compared with the respective reference currents, and the current errors $i_{d,error}$, $i_{q,error}$ and $i_{r,error}$ are fed back to the PI controllers to regulate the system. The field-oriented control strategy simplifies the control of the EESM, making it functionally similar to the control of a DC motor [98].

6.2 Thermal management for EESM to avoid overheating

The method of determining the optimal current references for FOC varies depending on the type of motor. For PMSM, only stator current components i_d and i_q are required. Due to their relatively low computational complexity, these optimal currents can be computed online using analytical motor models. In [99], the stator currents were optimized online in real-time based on the Maximum Torque Per Ampere (MTPA) and Maximum Torque Per Voltage (MTPV) principles. Similarly, in [100], an online MTPA strategy with reduced torque ripple was implemented. In contrast, EESM requires the optimization of three current components: i_d, i_q and i_r. This increased number of degrees of freedom enables improved performance, but also results in significantly higher computa-

tional requirements. Consequently, real-time optimization becomes impractical for EESMs. As a result, current reference sets are computed offline and stored in LUT for real-time use. In [46, 101], the optimization target was to minimize total losses, which serves as the theory basis for the method proposed in this work. While previous studies performed loss minimization globally at each operating point, they did not consider the real-time thermal state of the motor. Under thermally critical temperatures, minimizing overall losses may not be sufficient to reduce peak hotspot temperatures. Because due to high thermal resistance between the internal motor components (e.g. across the air gap), significant temperature gradients can exist. For a "cold" motor, global loss minimization provides optimal efficiency. However, when the motor operates under thermal stress, a thermal balancing strategy can be more beneficial. For instance, if the stator exhibits higher temperatures, the same torque can be produced by increasing rotor excitation current i_r and reducing stator currents i_d and i_q. Conversely, if the rotor is thermally stressed, the stator currents can be increased while reducing rotor excitation. Although this approach may not yield the best efficiency, it effectively reduce hotspot temperatures under thermal critical conditions. As a result, torque derating can be delayed during sustained overloads or entirely avoided in short-term thermal events.

6.2.1 Generation of currents LUTs with different weighting

The determination of the optimal current set (i_d, i_q i_r) at each operating point constitutes a constrained optimization problem, aimed at maximizing efficiency by minimizing total losses [101]:

$$f_\mathrm{obj} : \min_{i_\mathrm{d}, i_\mathrm{q}, i_\mathrm{r}} P_\mathrm{loss} = \min_{i_\mathrm{d}, i_\mathrm{q}, i_\mathrm{r}} P_\mathrm{stator} + P_\mathrm{rotor} \tag{6.14}$$

where P_stator and P_rotor denote the losses in the stator and rotor windings, respectively. The objective function f_obj minimizes these losses to achieve optimal efficiency, subject to the following constraints:

- Torque constraint

$$f_\mathrm{eq} : \frac{3}{2} z_\mathrm{p} \cdot (M_\mathrm{dr} \cdot i_\mathrm{r} \cdot i_\mathrm{q} + (L_\mathrm{d} - L_\mathrm{q}) \cdot i_\mathrm{d} \cdot i_\mathrm{q}) - T_{set} = 0 \tag{6.15}$$

- Current limits

$$f_{\text{cons1}} : {i_{\text{d}}}^2 + {i_{\text{q}}}^2 \leq {i_{\text{s,max}}}^2 \tag{6.16}$$

$$f_{\text{cons2}} : i_{\text{r}} \leq i_{\text{r,max}} \tag{6.17}$$

- Voltage limit

$$f_{\text{cons3}} : {u_{\text{d}}}^2 + {u_{\text{q}}}^2 \leq {u_{\text{s,max}}}^2 \tag{6.18}$$

In (6.15), z_{p} is the number of pole pairs, L_{d} and L_{q} are the d- and q- axis inductances, and M_{dr} is the mutual inductance between stator and rotor. These constraints ensure that the required torque is delivered without exceeding current or voltage limits.
In (6.14), the stator losses P_{stator} and P_{rotor} has the same weighting during the optimization, so that the best efficiency can be ensured. To further explore trade-offs between stator and rotor losses, weighting factors w are introduced in the objective functions:

$$\text{LUT1 with } f_{\text{obj,1}} : \min_{i_{\text{d}}, i_{\text{q}}, i_{\text{r}}} P_{\text{loss,1}} = \min_{i_{\text{d}}, i_{\text{q}}, i_{\text{r}}} 1 \cdot P_{\text{stator,1}} + 1 \cdot P_{\text{rotor,1}} \tag{6.19}$$

$$\text{LUT2 with } f_{\text{obj,2}} : \min_{i_{\text{d}}, i_{\text{q}}, i_{\text{r}}} P_{\text{loss,2}} = \min_{i_{\text{d}}, i_{\text{q}}, i_{\text{r}}} 1 \cdot P_{\text{stator,2}} + w \cdot P_{\text{rotor,2}} \tag{6.20}$$

$$\text{LUT3 with } f_{\text{obj,3}} : \min_{i_{\text{d}}, i_{\text{q}}, i_{\text{r}}} P_{\text{loss,3}} = \min_{i_{\text{d}}, i_{\text{q}}, i_{\text{r}}} w \cdot P_{\text{stator,3}} + 1 \cdot P_{\text{rotor,3}} \tag{6.21}$$

$$0 \leq w < 1 \tag{6.22}$$

Based on the value of the weighting factor w, three types of LUTs are generated. LUT1 corresponds to $w = 1$, resulting in equal weighting of stator and rotor losses and thus global efficiency optimization. By adjusting weighting factor w, LUT2 assigns greater importance to minimizing stator losses, while LUT3 prioritizes rotor loss minimization.
Utilizing the equations from (6.14) to (6.22), various optimization problems were solved to generate different current LUTs. It is important to note that the motor inductances in (6.15) vary with operating points due to magnetic saturation. To address this nonlinearity, FEA simulations were used with Ansys Maxwell.
Fig. 6.4 illustrates the workflow for LUT generation. The optimization process combines FEA and analytical computation. Ansys Maxwell is used to simulate motor performance (torque, inductance, and losses) under various current combinations. MATLAB performs the constrained optimization based on simulation

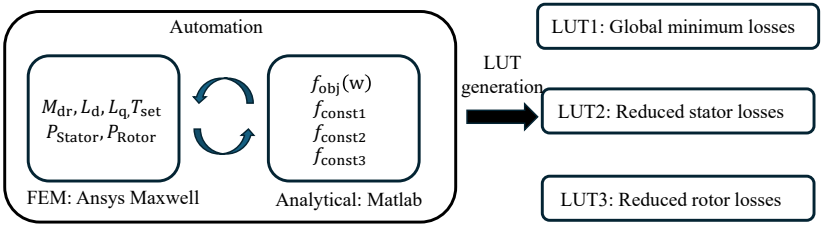


Figure 6.4: LUT generation automation with different weighting factors w

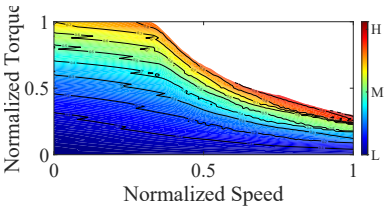
results, automatically generating LUTs for different w values. The resulting current sets ensure minimum total loss (LUT1), reduced stator losses (LUT2), or reduced rotor losses (LUT3).
Fig. 6.5 visualizes the corresponding loss maps with extreme case $w = 0$. Fig. 6.5 (a) - (b) show the stator and rotor losses for $f_{\text{obj},1}$; Fig. 6.5 (c) - (d) for $f_{\text{obj},2}$; and Fig. 6.5 (e) - (f) for $f_{\text{obj},3}$. As expected, stator losses in LUT3 are highest (Fig. 6.5 (e)), since they ate not considered in the optimization with $w = 0$. Rotor losses peak in LUT2 (Fig. 6.5 (d)), where they are similarly unweighted with $w = 0$. Comparing to LUT1, LUT3 yields visibly lower rotor losses (less red area in Fig. 6.5 (f)), while LUT2 yields slightly lower stator losses (Fig. 6.5 (c)), with contours shifting towards higher torque.

6.2.2 Control strategy with integrated thermal network

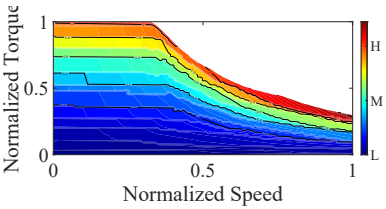
Different LUTs are employed to accommodate various thermal states of the motor:

- LUT 1 is used when the motor operates at low temperatures to maximize efficiency.
- LUT 2 is activated when critical stator temperatures are detected to reduce stator heating.
- LUT 3 is applied when rotor temperatures reach critical levels, aiming to lower rotor thermal stress.

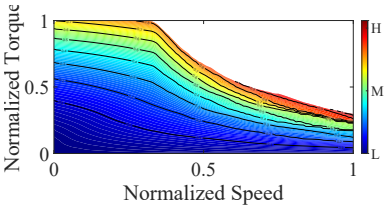
These control principles are illustrated in the control flow diagram shown in Fig. 6.6. At each time step, the node temperatures of the EESM are estimated



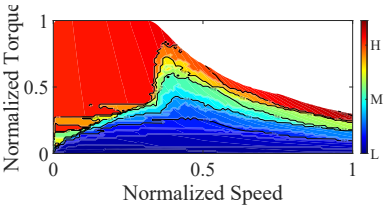
(a) Stator losses with LUT 1 with $w = 0$



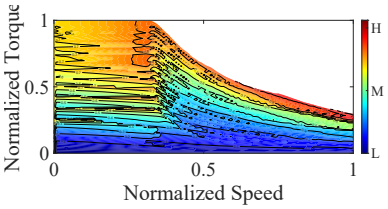
(b) Rotor losses with LUT 1 with $w = 0$



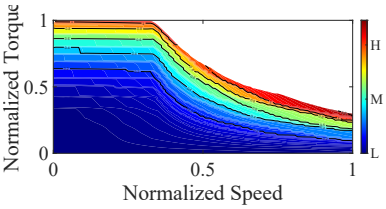
(c) Stator losses with LUT 2 with $w = 0$



(d) Rotor losses with LUT 2 with $w = 0$



(e) Stator losses with LUT 3 with $w = 0$



(f) Rotor losses with LUT 3 with $w = 0$

Figure 6.5: Qualitative compare between the stator and rotor losses for extreme case of weighting factor $w = 0$ in equation (6.22) [E3]

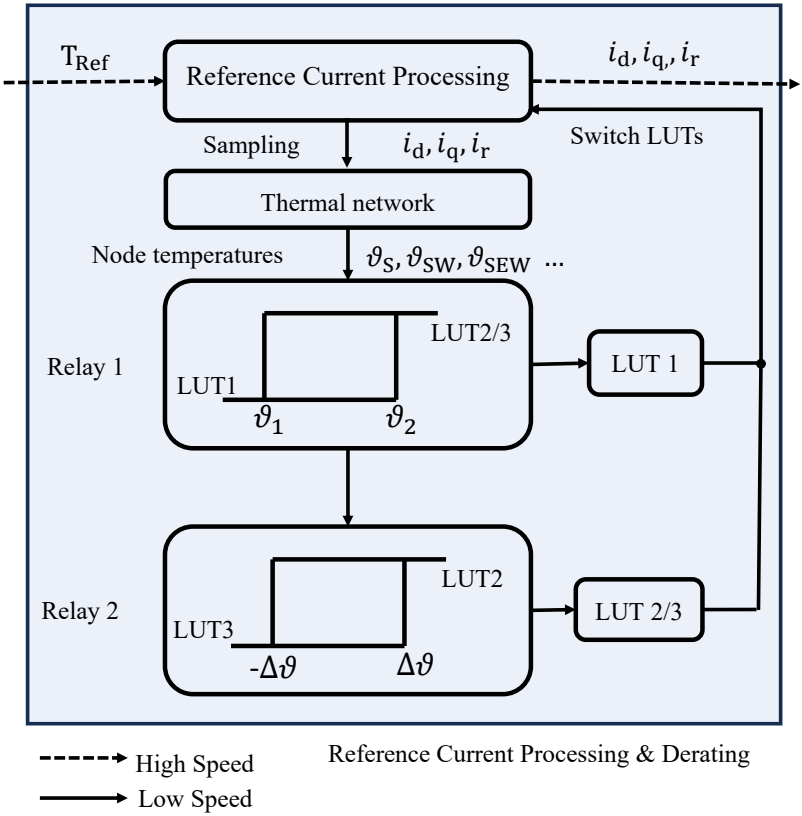


Figure 6.6: Novel control strategy with integrated thermal network [E3]

using the integrated thermal network based on measured currents. Depending on the estimated temperatures, a two-stage relay-based evaluation mechanism is applied to determine the appropriate thermal state and select the corresponding LUT.

- Relay 1 assesses whether the EESM is operating under elevated temperatures. If all node temperatures are below a defined threshold ϑ_1, LUT 1 is selected to ensure optimal efficiency.
- Relay 2 is triggered when node temperatures exceed a higher threshold ϑ_2. It calculates the temperature difference $\Delta\vartheta$ between the stator and rotor peak temperatures. Based on this difference, the system determines the location of the thermal hotspot:
  - If the stator temperature is dominant, LUT 2 is selected.
  - If the rotor temperature is dominant, LUT 3 is selected.

In Fig. 6.6, two signal paths with different update rates are distinguished. The dashed line represents the fast control loop used for FOC control of the motor torque. In contrast, the solid line represents the slower thermal control loop, which reflects the relatively slower thermal dynamics of the electric machine. A sampling period of 1 second is recommended for thermal management, and this value is implemented in the subsequent system simulations.

6.3 Validation with system simulation

To validate the proposed control strategy, system simulations are carried out using two test cycles: the US06 Supplemental FederalT Test Procedure (SFTP-US06) and the Renault Test Standard 1995 (RTS-95). Both cycles are characterized by aggressive driving behavior, including high speed and high acceleration. To allow the motor to reach a thermally critical state more quickly, the initial and boundary motor temperatures are set to $90\,^{\circ}\mathrm{C}$. A simulation time step of 1 second is used to observer the thermal dynamics of the electric machine. As illustrated in the block diagram in Fig. 6.7, the drive cycle block provides the reference vehicle speed v_{ref}, which is compared with the actual vehicle speed v_{veh}. The resulting speed difference, v_{diff}, serves as input to the driver model block, where the driver behavior is modeled. Based on v_{diff}, the corresponding torque command T_{ref} is generated and passed to the control strategy block. The control strategy block is the core of the entire system simulation. It implements the thermal management control logic described in Fig. 6.6. Given the torque demand T_{ref}, the block selects the corresponding current values i_{d}, i_{q} and i_{r} from the precomputed LUTs. These currents are then passed to the electric motor block, where the electric dynamics of the motor are simulated. The block outputs the mechanical torque T_{mot}, which is fed into the vehicle model block to

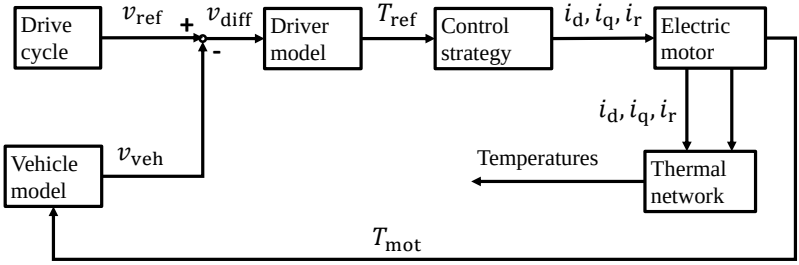


Figure 6.7: System simulation block diagram [E3]

determine the vehicle speed. Simultaneously, the currents are forwarded to the thermal network block, where the motor temperatures are estimated. This thermal feedback is essential for adjusting the control strategy under varying thermal conditions. Finally, the calculated vehicle speed is compared again with v_{ref} to complete the control loop. The structure and function of each simulation block shown in Fig. 6.7 are described in detail below.

Drive cycle block

In the drive cycle block, the SFTP-US06 drive cycle is employed in the system simulation. This cycle characterizes dynamic drive behaviour with highspeed and high-acceleration, which can result in critical thermal conditions for the electric machine [102]. As illustrated in Fig. 6.8, the simulation includes 10 consecutive repetitions of the SFTP-US06 drive cycle to achieve the thermal critical state. Since each cycle spans 600 seconds, the total system simulation time amounts to 6000 seconds. In Fig. 6.8, the blue curve shows the reference speed v_{ref} defined by the SFTP-US06 drive cycle, while the red curve represents the simulated vehicle speed v_{veh}. Due to the designed dynamics of the driver model, a strong correlation between v_{veh} and v_{ref} in Fig. 6.8 is observed, indicating that the driver model effectively tracks the target speed profile under dynamic conditions.

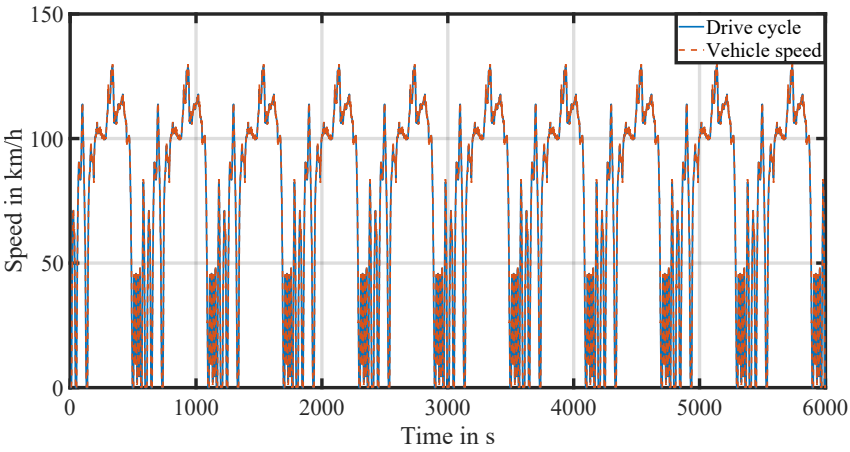


Figure 6.8: Repetitive SFTP-US06 drive cycle [E3]

Driver model block

In the driver model block, the driving behavior is modeled as a First-order Lag (PT1) system. The input to this block is the speed error v_{diff}, representing the difference between the reference speed and the actual vehicle speed. By tuning the proportional (P) and integral (I) parameters, different driving styles—such as aggressive or conservative—can be emulated. The output of the driver model block is the requested torque T_{ref}, as illustrated in Fig. 6.9.

Control strategy block

In the system simulation, the proposed control strategy is implemented as shown in Fig. 6.6. The following parameters are defined in the control strategy block [E3]:

$$\vartheta_1 = 120°C \tag{6.23}$$

$$\vartheta_2 = 125°C \tag{6.24}$$

$$\Delta\vartheta = 5K \tag{6.25}$$

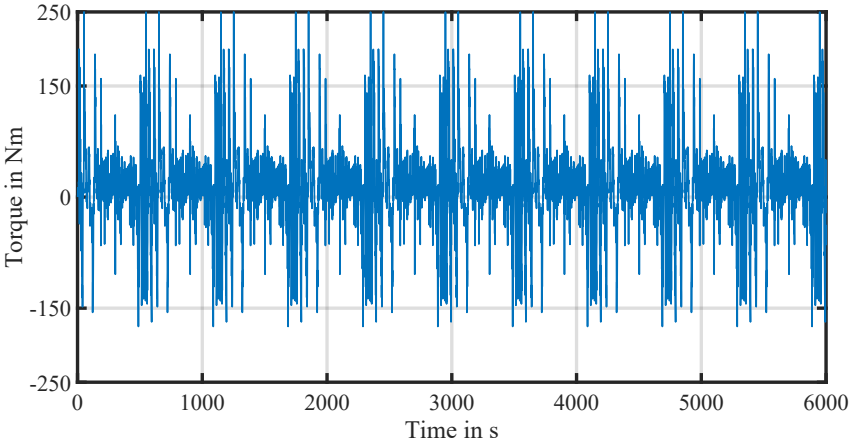


Figure 6.9: Motor torque profile with repetitive SFTP-US06 drive cycles [E3]

where ϑ_1 and ϑ_2 represent the lower and upper temperatures in relay 1, while $\Delta\vartheta$ denotes the temperature difference criterion employed in relay 2.

Electric motor block

In the electric motor block, the electromagnetic behavior of the EESM is considered. Due to the significantly slower thermal dynamics compared to the electrical dynamics, the EESM is assumed to operate in electrical steady-state at each thermal time step (1 second). As a result, the motor's transient electrical dynamics are neglected in the system simulation to simplify computation.

Thermal network block

In the thermal network block, the node temperatures of the electrical machine are computed. The mathematical representation of the thermal network is given by [13]:

$$C_i \cdot \frac{d\vartheta_i}{dt} = \frac{1}{R_{ji}}(\vartheta_j - \vartheta_i) + P_i \quad i,j = 1,2,...,7 \tag{6.26}$$

where C_i denotes the thermal capacity of the node i. ϑ_i is the node temperature, and P_i represents the power loss at node i. R_{ji} indicate the thermal resistance between two neighbouring nodes j and i.

Vehicle model block

In the vehicle model block, the vehicle dynamics are computed using a simplified vehicle model as follows:

$$m_{\text{veh}} \cdot \frac{dv_{\text{veh}}}{dt} = F_{\text{a}} - F_{\text{d}} - F_{\text{r}} - F_{\text{g}} \tag{6.27}$$

where m_{veh} is the vehicle mass, v_{veh} is the vehicle speed, F_{a} is the driving force, F_{d} is the air drag force, F_{r} is the rolling resistance, and F_{g} is the gravitational force. The driving force is calculated as:

$$F_{\text{a}} = \frac{T_{\text{mot}} \cdot j}{r_{\text{w}}} \tag{6.28}$$

where T_{mot} is the motor torque, j is the gear ratio, r_{w} is the dynamic wheel radius. The aerodynamic drag force is given by:

$$F_{\text{d}} = \frac{1}{2} \cdot \rho_{\text{a}} \cdot C_{\text{d}} \cdot A_{\text{c}} \cdot {v_{\text{veh}}}^2 \tag{6.29}$$

where ρ_{a} is the air density, C_{d} is the air drag coefficient, and A_{c} is the frontal cross-section area of the vehicle. The rolling resistance force is calculated as:

$$F_{\text{r}} = C_{\text{r}} \cdot g \cdot m_{\text{veh}} \cdot cos(\gamma) \tag{6.30}$$

where C_{r} is the rolling resistance coefficient, g is the gravitational acceleration, and γ is the road slope angle. The gravitational force is:

$$F_{\text{g}} = g \cdot m_{\text{veh}} \cdot sin(\gamma) \tag{6.31}$$

since the simulation assumes a flat road surface, the gravitational force F_{g} is considered to be zero. The vehicle parameters used in the system simulation are summarized in Tab. 6.1.

6.3.1 Validation results with SFTP-US06 drive cycle

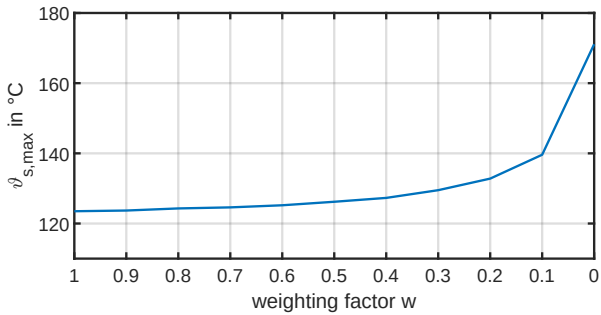
System simulations were carried out by varying the weighting factor w from 0 to 1 in increments of 0.1 in the control strategy block. This factor w, used in the LUT generation in (6.22), determines the relative weighting of stator and rotor losses in the optimization process. It effectively reflects the control intensity of the proposed thermal management strategy, aiming to minimize the internal

Table 6.1: Vehicle parameters in the system simulation [E3]

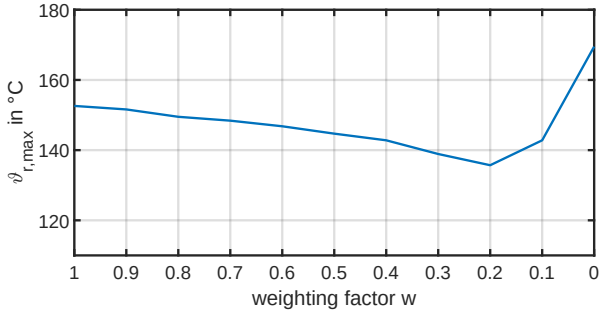
Parameter	Symbol	Value
Vehicle Mass	m_{veh}	$1700kg$
Vehicle cross-section area	A_{c}	$2.3m^2$
Air drag coefficient	C_{d}	0.23
Rolling resistance coefficient	C_{r}	0.01
Dynamic wheel radius	r_{w}	$0.32m$
Gear ratio between motor and wheels	j	9.5
Road slope angle	γ	0

Table 6.2: Maximum stator/rotor temperatures in °C and average losses in W with repetitive SFTP-US06 drive cycles

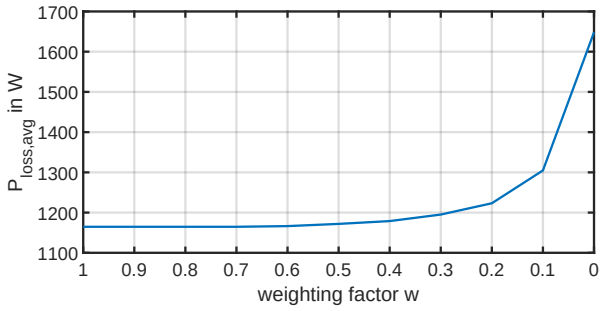
w	$\vartheta_{\text{sta,max}}$	$\vartheta_{\text{rot,max}}$	$P_{\text{loss,avg}}$
1	123.5	152.6	1164.7
0.9	123.7	151.6	1164.7
0.8	124.3	149.5	1164.7
0.7	124.6	148.4	1164.7
0.6	125.2	146.8	1166.4
0.5	126.2	144.7	1171.9
0.4	127.3	142.8	1178.9
0.3	129.5	138.9	1195.1
0.2	132.8	135.7	1223.2
0.1	139.6	142.8	1304.8
0	171.1	169.5	1648.2



(a) Compare of maximal stator temperatures $\vartheta_{\text{sta,max}}$



(b) Compare of maximal rotor temperatures $\vartheta_{\text{rot,max}}$



(c) Compare of average motor losses $P_{\text{loss,avg}}$

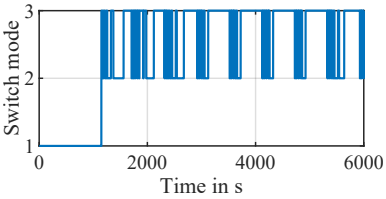
Figure 6.10: Comparison between the stator/rotor maximal temperatures and average losses at different w factors by repetitive SFTP-US06 drive cycles [E3]

temperature differences within the motor. A higher w (approaching 1) indicates weaker thermal management control, resulting in slower temperature balancing between components. Conversely, a lower w (approaching 0) indicates stronger control intensity and more rapid balancing of internal temperatures.
The simulation results for different values of w are summarized qualitative in Fig. 6.10 and quantitatively in Tab. 6.2. In Fig. 6.10, the x-axis represents the applied weighting factor w. Fig. 6.10 (a) - (b) represent the maximum stator and rotor node temperatures, respectively, while Fig. 6.10 (c) presents the corresponding average power loss $P_{\text{loss,avg}}$.
As shown in Fig. 6.10 (c), as w decreases from 1 to 0, the average loss $P_{\text{loss,avg}}$ initially remains constant at 1164.7 W, then increases gradually to 1223.2 W, and finally rises rapidly to 1648.2 W. This trend indicates that the average power loss $P_{\text{loss,avg}}$ does not scale linearly with w, but instead increases at an accelerating rate as the control intensity becomes stronger.
Given that the rotor typically exhibits a higher maximum temperature than the stator with the housing water jacket cooling concept, the thermal management strategy primarily targets rotor temperature reduction while maintaining constant torque. This requires increased stator current, which consequently raises stator temperatures.
As illustrated in Fig. 6.10 (b), for w values ranging between 1 and 0.2: the rotor maximum temperature decreases significantly from $152.6\,^{\circ}$C to $135.7\,^{\circ}$C, while the stator maximum temperature increases moderately from $123.5\,^{\circ}$C to $132.8\,^{\circ}$C. This trade-off results in an overall reduction of the motor's peak temperature. However, when w falls below 0.2, both stator and rotor max temperatures rise significantly. This is due to overcompensation in the optimization process: the excessive focus on minimizing losses in one component leads to increased losses in the other, which, coupled with thermal coupling via the thermal resistance, results in overall higher losses.
These results demonstrate that the proposed strategy is effective in reducing hot spot temperatures and mitigating performance derating. An optimal control performance is observed at $w = 0.2$, where the average power loss is still acceptable, rotor maximum temperature reaches its minimum of $135.7\,^{\circ}$C, and the stator temperature increases only slightly.
To further examine the control strategy, three representative cases were analyzed: $w = 0, 0.2, 1$:

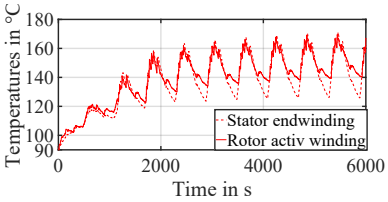
- $w = 0$: in this case, LUT1 is not influenced, ensuring the maximum efficiency. In LUT2, only stator losses are considered during optimization, while LUT3 considers only rotor losses. This results in the highest average power losses.

- $w = 0.2$: LUT1 remains the same, while LUT2 prioritizes stator losses (weight = 1) and LUT3 prioritizes rotor losses. As Fig. 6.10 shows, this configuration effectively reduces hot spot temperatures with only a moderate increase in motor losses.
- $w = 1$: LUT1, LUT2 and LUT3 are identical, optimized solely for maximum global efficiency. While global motor losses are minimized, this leads to large temperature difference between stator and rotor, resulting in high overall hot spot temperatures.

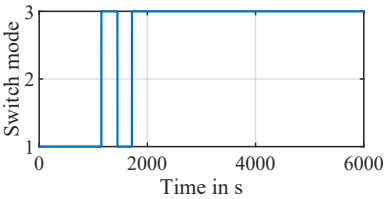
In Fig. 6.11, The thermal behavior of the control strategy during repeated SFTP-US06 drive cycles is illustrated. Fig. 6.11 (a) - (b) show the case with $w = 0$, where high losses cause frequent switching within the control unit between LUT2 and LUT3. Despite a reduction in temperature difference between stator and rotor, the overall motor temperature rises. Fig. 6.11 (c) - (d) show the balanced scenario at $w = 0.2$. The control algorithm successfully balances the stator and rotor maximum temperatures, reducing the hot spot temperature. Fig. 6.11 (e) - (f) display results for $w = 1$. In this case, the motor operates solely with LUT 1 to ensure the maximum efficiency. However, the temperature difference between stator and rotor remains large, keeping the global hot spot temperature increased. Fig. 6.12 presents the power loss maps for LUT1, LUT2 and LUT3 generated with $w = 0.2$. Comparing the stator losses map in the first column, Fig. 6.5 (c) shows the least red area and the most blue area, indication the lowest stator power losses. This results from the higher weighting applied to stator loss during LUT2 optimization. Similarly, Fig. 6.5 (f) in the second column shows minimized rotor losses due to higher weighting applied to rotor loss in LUT3. Thus, it can be observed that the weighting factor w influence the control intensity by defining the loss prioritization during LUT optimization.



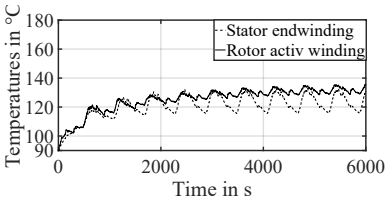
(a) Mode swich with $w = 0$



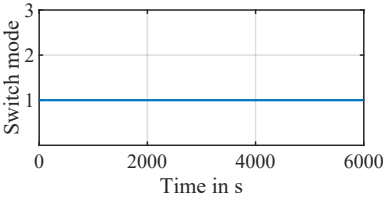
(b) Maximal stator/rotor temperatures with $w = 0$



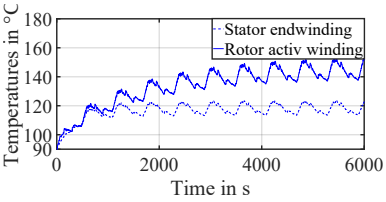
(c) Mode swich with $w = 0.2$



(d) Maximal stator/rotor temperatures with $w = 0.2$

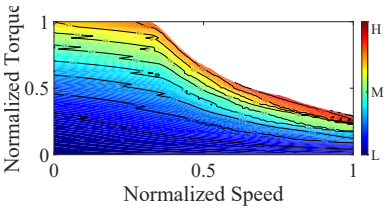


(e) Mode swich with $w = 1$

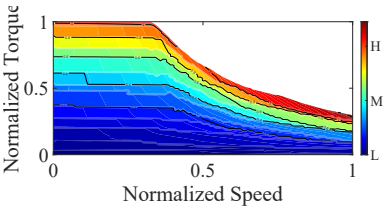


(f) Maximal stator/rotor temperatures with $w = 1$

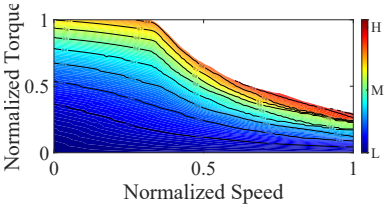
Figure 6.11: Mode switch and maximal stator and rotor temperatures profiles with $w = 0$, 0.2 and 1 by repetitive SFTP-US06 drive cycles [E3]



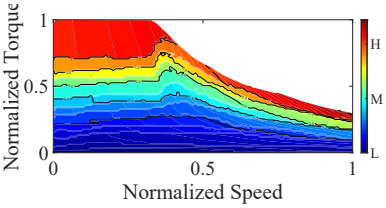
(a) Stator losses with LUT 1 with w = 0.2



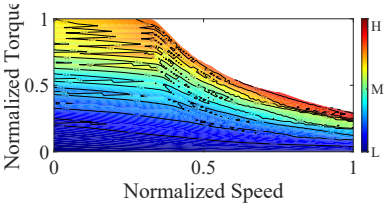
(b) Rotor losses with LUT 1 with w = 0.2



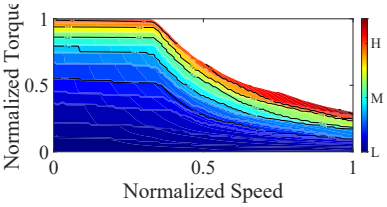
(c) Stator losses with LUT 2 with w = 0.2



(d) Rotor losses with LUT 2 with w = 0.2



(e) Stator losses with LUT 3 with w = 0.2



(f) Rotor losses with LUT 3 with w = 0.2

Figure 6.12: Qualitative compare between the stator and rotor losses for weighting factor $w = 0.2$ in equation (6.22) [E3]

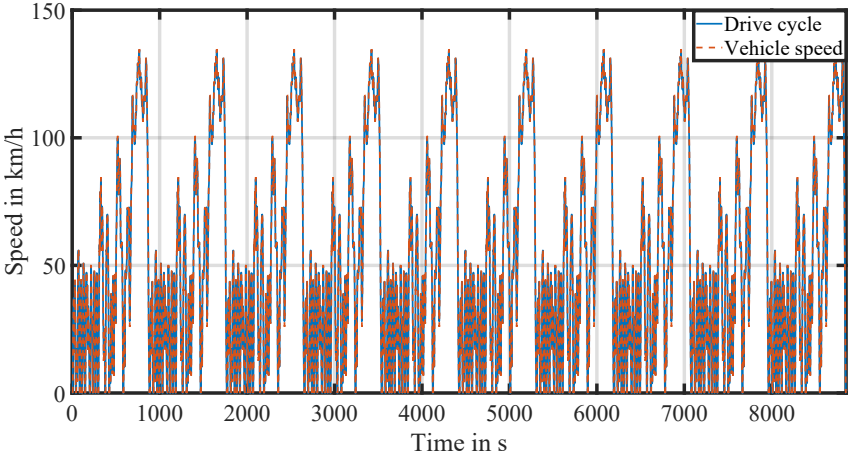


Figure 6.13: Repetitive RTS-95 drive cycle [E3]

6.3.2 Validation results with RTS-95 drive cycle

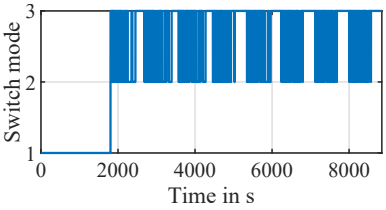
To further validate the effectiveness of the control strategy with $w = 0.2$, a second test cycle, RTS-95, was employed. RTS-95 represent also aggressive driving behavior and includes urban, rural and motorway segments [103]. The speed profile of this cycle is shown in Fig. 6.13. The cycle was developed using a subset of the Worldwide Harmonized Light Vehicles Test Procedure (WLTP) database, emphasizing high-speed and high-load engine operating points [103]. Fig. 6.14 compares the maximum stator and rotor temperatures as well as the mode switching behavior for three control intensities $w = 0$, $w = 0.2$, and $w = 1$:

- first row (Fig. 6.14 (a) and Fig. 6.14 (b)): at $w = 0$, frequent switching between LUT2 and LUT3 minimizes the temperature difference between the stator and rotor. However, this results in excessive total power loss, leading to increased temperatures in both components.
- second row (Fig. 6.14 (c) and Fig. 6.14 (d)): at $w = 0.2$, mode switching between LUT1 and LUT3 effectively reduces the rotor's maximum temperature, while the stator temperature increases slightly. As a result, the overall

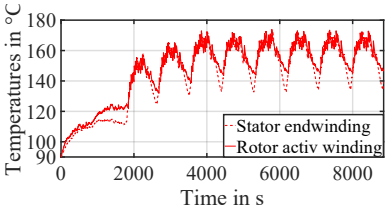
motor hotspot temperature is significantly reduced. These findings are consistent with the results obtained from the SFTP-US06 test cycle.

- third row (Fig. 6.14 (e) and Fig. 6.14 (f)): at $w = 1$, when no thermal management is applied (i.e., only LUT1 is used), a significant temperature imbalance is observed between stator and rotor, due to the lack of control in terms of thermal balancing.

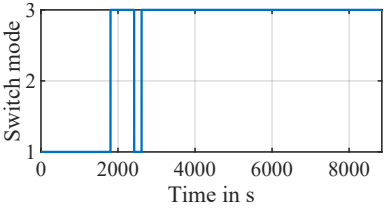
These results are consistent with the simulation results under the SFTP-US06 drive cycle.
In summary, simulations under both aggressive drive cycles (SFTP-US06 and RTS95) demonstrate that the proposed thermal management strategy effectively reduce the motor's hotspot temperature. The study of the control intensity parameter w reveals the dual nature of the strategy: a high control intensity (w = 0) can rapidly balance the temperature difference between the stator and rotor, but leads to excessive overall losses; conversely, a low control intensity ($w \to 1$) reduces losses but fails to eliminate internal temperature imbalances, especially under critical thermal conditions, resulting in an inability to suppress hotspot temperatures. Through the investigation of different values of control intensity w, it was found that $w = 0.2$ offers an effective trade-off between average loss and hotspot temperature under aggressive driving conditions.
It is worth noting that although the proposed strategy has been validated through system simulations to be effective in reducing hotspot temperatures under aggressive drive cycles, the selection of the control intensity w in this study is based on representative thermal cycles and remains constant throughout operation. This makes the strategy both effective and easy to implement.
As outlook, a more general and adaptive control strategy, where w is dynamically adjusted in real time based on the thermal state of the motor to select the appropriate LUT holds promise for further optimizing the thermal performance of electrical machines.



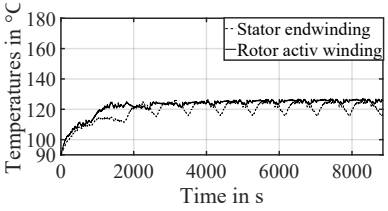
(a) Mode swich with $w = 0$



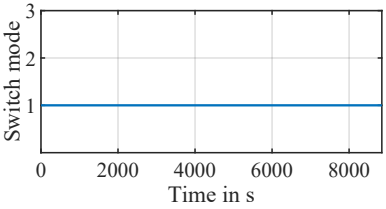
(b) Maximal stator/rotor temperatures with $w = 0$



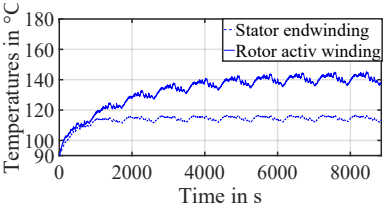
(c) Mode swich with $w = 0.2$



(d) Maximal stator/rotor temperatures with $w = 0.2$



(e) Mode swich with $w = 1$



(f) Maximal stator/rotor temperatures with $w = 1$

Figure 6.14: Mode switch and maximal stator/rotor temperatures profiles with $w = 0$, 0.2 and 1 by repetitive RTS-95 drive cycles

Chapter 7

Summary and outlook

7.1 Summary

Electric vehicles have revolutionized the automotive industry, driving significant advancements in electric motors, electronic controls and battery technologies. Opportunities are accompanied by challenges. In the field of electric vehicles, numerous technical hurdles remain. For instance, in battery technology, there is a growing demand for higher energy density to extend driving range and enable faster charging. In the field of power electronics, significant research has focused on Gallium Nitride (GaN) inverters for high-frequency and high-efficiency wireless power transfer, as well as on the exploration of Multilevel Converter (MLC) topologies for inverter applications. In electric motor development, the focus lies on achieving smaller and lighter designs with higher rotational speeds, greater torque, and increased power density. Effective thermal management is crucial for high-power density motors, including both the cooling concept and the thermal control strategy of the motor. This thesis focuses on online temperature monitoring and thermal management of an 6-pole EESM equipped with a water jacket cooling system. The research is structured into three levels: development of a low-order thermal network at the component level; investigation of system-level thermal behavior and state observation; thermal management strategy design at the application level.

At the component level, a topology of the thermal network topology for the EESM is proposed. Based on this topology, components in this thermal network are analytically calculated, including the power loss, thermal capacities and thermal resistances. A hybrid parameter identification method combining static and

dynamic identification is developed. Using experimental data from a test bench, thermal resistances are identified under steady-state conditions, while thermal capacities are identified from the transient conditions. This approach effectively reduces parameter coupling during the identification process and thus enhances identification accuracy. After parameter identification, the accuracy of the model is verified by cross-validation.
At the system level, the thermal network's dynamic is analyzed with a focus on error sources including process noise, measurement noise and initial deviation. The continuous-time thermal model is discretized for implementation as a state observer, with attention to preserving model accuracy and system stability. Based on the discretized system, two concepts of Karman filter were introduced. In concept A, temperature feedback from the stator end winding is used — a method previously applied to PMSM [11, 104], and here extended to EESM. concept B, proposed for the first time, fuses stator temperature and rotor voltage and current signals. Experimental validation reveals that concept A is inadequate for estimating rotor temperatures due to weak thermal coupling across the air gap. In contrast, concept B achieves accurate rotor temperature estimation through sensor fusion, demonstrating superior observability.
At the application level, thermal management strategy based on the thermal network is proposed. As state of the art, torque derating is employed to protect the motor under critical thermal conditions [46]. This study introduces a new control approach that initially avoids torque derating. Before torque derating, this strategy actively balances internal temperature gradients to reduce peak temperatures, at the cost of sightly increased overall energy losses. Simulation results under two aggressive driving cycles, SFTP-US06 and RTS-95, validate the effectiveness of the approach. By varying the optimization weighting factor w, the impact of control intensity on motor performance is systematically evaluated. Notably, this approach can delay or even prevent overheating during short-term overloads, it cannot eliminate the need for torque derating under sustained overload.

7.2 Outlook

The thermal network model and Kalman filter proposed in this study aim to enable temperature monitoring and facilitate effective thermal management of the EESM. The current thermal management strategy is based on a constant control gain w, which regulates the thermal state of the motor. This approach offers the advantages of simplicity and low computational overhead.

Future work will focus on enhancing the control strategy by dynamically estimating the motor's thermal state in real time and selecting an optimal thermal management gain w accordingly. This Predictive approach, which estimates future thermal behavior and adjusts control effort correspondingly, could be implemented using an MPC. However, since the computational complexity of MPC is challenging, the real-time performance of the overall thermal management system remains an important direction for future research.
With respect to validation, the results presented in this study are based on experimental data from test bench using an reference EESM. A logical next step is to integrate the thermal network model, Kalman filter algorithm, and adaptive thermal management strategy into the embedded controller of a real EV under real driving conditions. Such integration would enable real-time implementation and allow more accurate evaluation of thermal performance under real driving conditions. Furthermore, it would facilitate deeper investigation into the effects of process noise, measurement noise, and initial deviation on the system's thermal estimation accuracy in real-world scenarios.

Chapter A

Appendix

$$
\begin{aligned}
R_{\mathrm{T,1r}} &= \frac{1}{4\pi\lambda_{\mathrm{r}}L}[1-\frac{2{r_2}^2\ln(\frac{r_1}{r_2})}{{r_1}^2-{r_2}^2}] \\
R_{\mathrm{T,2r}} &= \frac{1}{4\pi\lambda_{\mathrm{r}}L}[\frac{2{r_1}^2\ln(\frac{r_1}{r_2})}{{r_1}^2-{r_2}^2}-1] \\
R_{\mathrm{T,3r}} &= \frac{1}{8\pi({r_1}^2-{r_2}^2)\lambda_{\mathrm{r}}L}[{r_1}^2+{r_2}^2-\frac{4{r_1}^2{r_2}^2\ln(\frac{r_1}{r_2})}{{r_1}^2-{r_2}^2}]
\end{aligned}
\tag{A.1}
$$

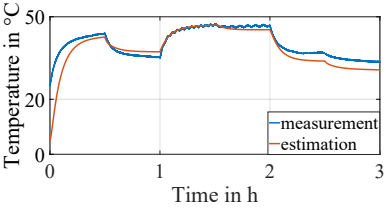
$$
\begin{aligned}
r_{\mathrm{m}} &= \frac{r_1+r_2}{2} \\
R_{\mathrm{I,1r}} &= \frac{1}{2\pi\lambda_{\mathrm{r}}}\ln(\frac{r_1}{r_{\mathrm{m}}}) \\
R_{\mathrm{I,2r}} &= \frac{1}{2\pi\lambda_{\mathrm{r}}}\ln(\frac{r_{\mathrm{m}}}{r_2})
\end{aligned}
\tag{A.2}
$$

$$
\begin{aligned}
R_{\mathrm{T,1a}} &= \frac{L}{2\pi\lambda_{\mathrm{a}}({r_1}^2-{r_2}^2)} \\
R_{\mathrm{T,2a}} &= \frac{L}{2\pi\lambda_{\mathrm{a}}({r_1}^2-{r_2}^2)} \\
R_{\mathrm{T,3a}} &= -\frac{L}{6\pi\lambda_{\mathrm{a}}\pi({r_1}^2-{r_2}^2)}
\end{aligned}
\tag{A.3}
$$

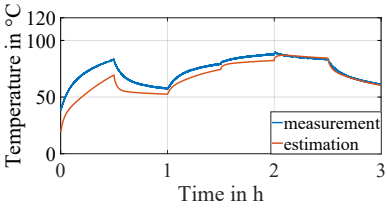
$$R_{\mathrm{I,1a}} = \frac{L}{2\pi\lambda_{\mathrm{a}}({r_1}^2 - {r_2}^2)}$$
$$R_{\mathrm{I,2a}} = \frac{L}{2\pi\lambda_{\mathrm{a}}({r_1}^2 - {r_2}^2)} \tag{A.4}$$

$$
A(:,1:4) = \begin{bmatrix}
-(\frac{1}{R_1}+\frac{1}{R_2}+\frac{1}{R_5})/C_S & \frac{1}{R_2}/C_S & 0 & \frac{1}{R_5}/C_S \\
\frac{1}{R_2}/C_{SW} & -(\frac{1}{R_2}+\frac{1}{R_3})/C_{SW} & \frac{1}{R_3}/C_{SW} & 0 \\
0 & \frac{1}{R_3}/C_{SEW} & -(\frac{1}{R_3}+\frac{1}{R_4})/C_{SEW} & 0 \\
\frac{1}{R_5}/C_R & 0 & 0 & -(\frac{1}{R_5}+\frac{1}{R_6}+\frac{1}{R_9})/C_R \\
0 & 0 & 0 & \frac{1}{R_6}/C_{RW} \\
0 & 0 & 0 & 0 \\
0 & 0 & 0 & \frac{1}{R_9}/C_{Sh}
\end{bmatrix}
$$

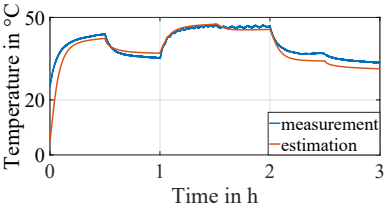
$$
A(:,5:7) = \begin{bmatrix}
0 & 0 & 0 \\
0 & 0 & 0 \\
0 & 0 & 0 \\
\frac{1}{R_6}/C_R & 0 & \frac{1}{R_9}/C_R \\
-(\frac{1}{R_6}+\frac{1}{R_7})/C_{RW} & \frac{1}{R_7}/C_{RW} & 0 \\
\frac{1}{R_7}/C_{REW} & -(\frac{1}{R_7}+\frac{1}{R_8})/C_{REW} & 0 \\
0 & 0 & -(\frac{1}{R_9}+\frac{1}{R_{10}})/C_{Sh}
\end{bmatrix}
\tag{A.5}
$$



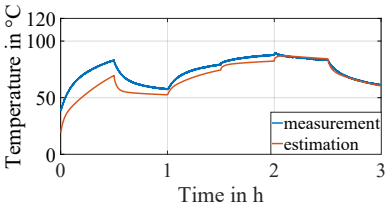
(a) Stator active winding temperature estimation without Kalman filter



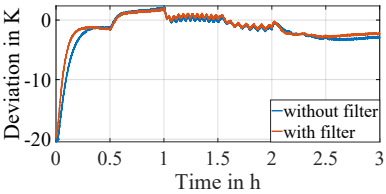
(b) Rotor end winding temperature estimation without Kalman filter



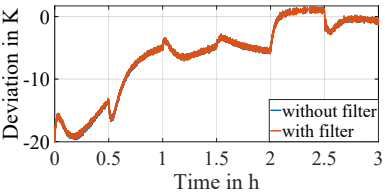
(c) Stator active winding temperature estimation with Kalman filter



(d) Rotor end winding temperature with Kalman filter

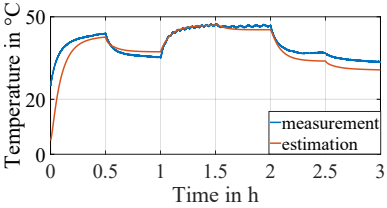


(e) Deviation comparison of stator active winding

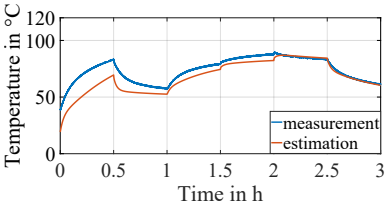


(f) Deviation comparison of rotor end winding

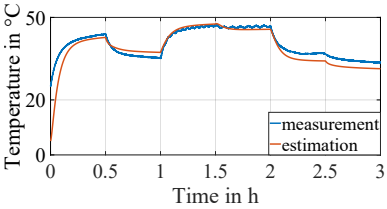
Figure A.1: Comparison of the model temperature estimation with and without Kalman filter concept A with assumed initial deviation $\varepsilon_{\mathrm{k}} = 20K$. Measurement in solid blue line and Model estimation in solid red line.



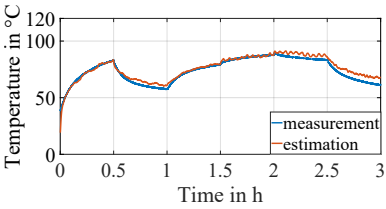
(a) Stator active winding temperature without Kalman filter



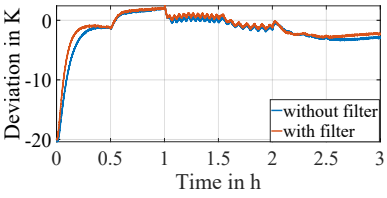
(b) Rotor end winding temperature without Kalman filter



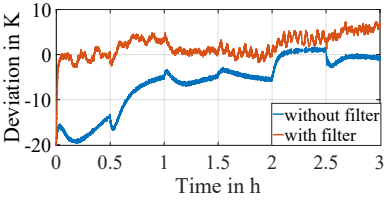
(c) Stator active winding temperature with Kalman filter



(d) Rotor end winding temperature with Kalman filter



(e) Deviation comparison of stator active winding



(f) Deviation comparison of rotor end winding

Figure A.2: Comparison of the model temperature estimation with and without Kalman filter concept b with assumed initial deviation $\varepsilon_{\mathrm{k}} = 20K$. Measurement in solid blue line and Model estimation in solid red line.

List of Figures

1.1 State of the art about torque derating [46] 6
1.2 Outline of the thesis 8

2.1 Types of heat transfer with ϑ_1 higher as ϑ_2 in each subfigures [53] 10
2.2 Major heat transfers in the EESM cross section 13
2.3 Schematic loss diagram for EESM 14
2.4 Current distribution under skin effect [57] 15
2.5 Current distribution under proximity effect [57] 16
2.6 Approximate hysteresis curves of electrical sheets of M400-65A and M800-65A from Surahammars Bruk AB [55] 17
2.7 Schematic illustration of the eddy current in a electrical sheet [55] 18
2.8 Major mechanical losses in the EESM cross section 19
2.9 Schematic EESM cross section 20
2.10 EESM thermal network [E1] 21
2.11 EESM cross section with important thermal paths as overview . 23
2.12 Hollow cylindrical shape as basic thermal unit [13] 24
2.13 Basic thermal network unit in the electrical machine with LPTN approach. Left: T-type thermal network unit according to Mellor and Turner model [13]; Right: I-type thermal network unit according to Bolietti [15, 62] 24
2.14 Skin and proximity effect modelling 28
2.15 Comparison between the analytical and FEM estimation of skin and proximity effect 28
2.16 Iron losses approximation between FEA method and polynomial approximation 31

3.1 EESM test bench 34
3.2 Schematic illustrated sensor locations 35

3.3 Stator phase winding temperature measurements at operating point 70 Nm and 3000 1/min 38
3.4 Motor component temperature measurements at operating point 70 Nm and 3000 1/min 40
3.5 Boundary conditions of the static test at speed 3000 1/min, torque 70 Nm 43
3.6 Summary of the operating points according to test types 44
3.7 Different types of tests with measured motor component temperatures 46

4.1 Direct parameter identification [71] 48
4.2 Indirect parameter identification [71] 48
4.3 Principle of combined static-dynamic identification with particle swarm optimization 50
4.4 Convective thermal resistance 54
4.5 Thermal flow at steady-state by working point 3000 1/min and 70 Nm 56
4.6 Sensitivity analysis of the stator end space resistance with $S = 2$ based on the steady temperatures at 3000 1/min and 70 Nm . . . 57
4.7 Sensitivity analysis of the air gap resistance with $S = 2$ based on the steady temperatures at 3000 1/min and 70 Nm 57
4.8 Temperature profiles in dynamic drive cycles with 20 °C inlet cooling water temperature. Drive cycle profiles of dynamic cycle 1 on the left column, dynamic cycle 2 on the right column. The measured data in solid blue line, the estimation temperature in dotted red line, the temperature deviation in solid black line . . . 59
4.9 Temperature profiles in dynamic drive cycles with 20 °C inlet cooling water temperature. Drive cycle profiles of dynamic cycle 3 on the left column, dynamic cycle 4 on the right column. The measured data in solid blue line, the estimation temperature in dotted red line, the temperature deviation in solid black line . . . 60

5.1 Correlation of the thermal network system to required torque . . 64
5.2 Block diagram of the EESM network 64
5.3 Comparison between thermal network and real motor under process and measurement noise at operating point 3000 rpm and 70 N m 68
5.4 Comparison between thermal network and real motor under initial deviation at operating point 3000 rpm and 70 N m 71

5.5 Comparison between time continuous thermal network with Euler and Runge-Kutta method 4. Order, rotor active winding temperature by the operating point 70 Nm and 3000 1/min as demonstration 73
5.6 Block diagram of classic Kalman filter [83] 75
5.7 Concepts of Kalman filter for EESM [E2] 77
5.8 Thermal cycle for testing of Kalman filter concept A and concept B 78
5.9 Comparison of the model estimation with and without Kalman filter concept A with assumed initial deviation $\varepsilon_{\mathrm{k}} = 20K$. Measurement in solid blue line and Model estimation in solid red line. 80
5.10 Sensitivity analysis of the stator end winding power losses with $S = 2$ based on the steady temperatures at 3000 1/min and 70 Nm 81
5.11 Sensitivity analysis of the rotor winding power losses with $S = 2$ based on the steady temperatures at 3000 1/min and 70 Nm . . . 81
5.12 Distortion of rotor winding temperature estimation based on the rotor winding voltage and current in the first 10s of the thermal cycle in Fig. 5.8 (a) and Fig. 5.8 (b) 83
5.13 Comparison of the model estimation with and without Kalman filter concept B with assumed initial deviation $\varepsilon_{\mathrm{k}} = 20K$ in the first half hour. Measurement in solid blue line and Model estimation in solid red line. 85

6.1 Winding system of the EESM [97] 89
6.2 Equivalent circuit diagram of the EESM [97] 92
6.3 Torque control of the EESM [46] 93
6.4 LUT generation automation with different weighting factors w . 96
6.5 Qualitative compare between the stator and rotor losses for extreme case of weighting factor $w = 0$ in equation (6.22) [E3] . 97
6.6 Novel control strategy with integrated thermal network [E3] . . 98
6.7 System simulation block diagram [E3] 100
6.8 Repetitive SFTP-US06 drive cycle [E3] 101
6.9 Motor torque profile with repetitive SFTP-US06 drive cycles [E3] 102
6.10 Comparison between the stator/rotor maximal temperatures and average losses at different w factors by repetitive SFTP-US06 drive cycles [E3] 105
6.11 Mode switch and maximal stator and rotor temperatures profiles with w = 0, 0.2 and 1 by repetitive SFTP-US06 drive cycles [E3] 108
6.12 Qualitative compare between the stator and rotor losses for weighting factor $w = 0.2$ in equation (6.22) [E3] 109

6.13 Repetitive RTS-95 drive cycle [E3] 110
6.14 Mode switch and maximal stator/rotor temperatures profiles with w = 0, 0.2 and 1 by repetitive RTS-95 drive cycles 112

A.1 Comparison of the model temperature estimation with and without Kalman filter concept A with assumed initial deviation $\varepsilon_{\mathrm{k}} = 20K$. Measurement in solid blue line and Model estimation in solid red line. 120
A.2 Comparison of the model temperature estimation with and without Kalman filter concept b with assumed initial deviation $\varepsilon_{\mathrm{k}} = 20K$. Measurement in solid blue line and Model estimation in solid red line. 121

List of Tables

2.1 Thermal resistances in the network 21

3.1 Technical data of the using thermocouples [70] 34
3.2 Motor temperature sensor locations and types 36

4.1 Operating points used for the model static identification 52
4.2 Conductive thermal resistances and thermal capacities 53

5.1 Eigenvalues of the state-transition matrix Φ at varied speed . . . 70

6.1 Vehicle parameters in the system simulation [E3] 104
6.2 Maximum stator/rotor temperatures in °C and average losses in W with repetitive SFTP-US06 drive cycles 104

Bibliography

Own publications

[E1] E. Wang, P. Grabherr, P. Wieske, and M. Doppelbauer, "A Low-Order Lumped Parameter Thermal Network of Electrically Excited Synchronous Motor for Critical Temperature Estimation," in *2022 International Conference on Electrical Machines (ICEM)*, 2022, pp. 1562–1568.

[E2] E. Wang, P. Grabherr, C. Koolmann, J. Mack, and M. Doppelbauer, "Untersuchung verschiedener Konzepte zur Abweichungsreduzierung bei der Echtzeit-Temperaturüberwachung mittels thermischer Netzwerke," in *Experten-Forum Powertrain: Komponenten und Kompetenzen zukünftiger Antriebe 2022*, Springer, 2022, pp. 54–67.

[E3] E. Wang, C. Schmülling, C. Kürten, P. Grabherr, and M. Doppelbauer, "Thermal management of electrically excited synchronous motor with integrated thermal network in automotive drive system," in *2023 IEEE 14th International Symposium on Diagnostics for Electrical Machines, Power Electronics and Drives (SDEMPED)*, 2023, pp. 479–485.

Supervised students thesis

[S1] J. Bernhard, "Thermische Modellierung von Kugellagern in elektrischen Fahrzeugantrieben," M.S. thesis, Technische Hochschule Ingolstadt, 2022.

Other publications

[1] T. Epskamp, “Steigerung der Leistungsdichte von Traktionsantrieben und Aufbau einer hochdrehenden Asynchronmaschine,” Ph.D. dissertation, Karlsruhe Institut of Technology, 2020.

[2] Kraftfahrt-Bundesamt. “Neuzulassungen von Personenkraftwagen (Pkw) im Jahresverlauf 2024 nach Marken und alternativen Antrieben.” (2025), [Online]. Available: https://www.kba.de/DE/Presse/Pressemitteilungen/AlternativeAntriebe/2025/pm03_2025_Antriebe_12_24_komplett.html?snn=3662144 (visited on 03/10/2025).

[3] J. Edmondson. “How Can Tesla Shift Away from Rare Earths?” (2023), [Online]. Available: https://www.idtechex.com/en/research-article/how-can-tesla-shift-away-from-rare-earths/28820 (visited on 05/25/2023).

[4] O. Wallscheid and J. Böcker, “Derating of automotive drive systems using model predictive control,” in *2017 IEEE International Symposium on Predictive Control of Electrical Drives and Power Electronics (PRECEDE)*, 2017, pp. 31–36.

[5] T. Harth, “Indirekte Temperaturmessung über die Statorspulen eines BLDC-Motors während des Laufenden Betriebs,” M.S. thesis, Hochschule Karlsruhe Technik und Wirtschaft, Gernamny, 2014.

[6] W. Kirchgässner, O. Wallscheid, and J. Böcker, “Estimating Electric Motor Temperatures With Deep Residual Machine Learning,” *IEEE Transactions on Power Electronics*, vol. 36, no. 7, pp. 7480–7488, 2021.

[7] D. Liang, Z. Q. Zhu, Y. Zhang, J. Feng, S. Guo, Y. Li, J. Wu, and A. Zhao, “A Hybrid Lumped-Parameter and Two-Dimensional Analytical Thermal Model for Electrical Machines,” *IEEE Transactions on Industry Applications*, vol. 57, no. 1, pp. 246–258, 2021.

[8] O. Wallscheid and J. Böcker, “Global Identification of a Low-Order Lumped-Parameter Thermal Network for Permanent Magnet Synchronous Motors,” *IEEE Transactions on Energy Conversion*, vol. 31, no. 1, pp. 354–365, 2016.

[9] J. Feng, D. Liang, Z. Q. Zhu, S. Guo, Y. Li, and A. Zhao, “Improved Low-Order Thermal Model for Critical Temperature Estimation of PMSM,” *IEEE Transactions on Energy Conversion*, vol. 37, no. 1, pp. 413–423, 2022.

[10] R. Saheba, M. Rotea, O. Wasynczuk, S. Pekarek, and B. Jordan, "Virtual Themrmal Sensing for Electric Machines," pp. 42–56, 2010.

[11] O. Wallscheid and J. Böcker, "Fusion of direct and indirect temperature estimation techniques for permanent magnet synchronous motors," in *2017 IEEE International Electric Machines and Drives Conference (IEMDC)*, 2017, pp. 1–8.

[12] R. L. Kotnik, "An Equivalent Thermal Circuit for Nonventilated Induction Motors [includes discussion]," *Transactions of the American Institute of Electrical Engineers. Part III: Power Apparatus and Systems*, vol. 73, no. 2, pp. 1604–1609, 1954.

[13] P. Mellor, D. Roberts, and D. Turner, "Lumped parameter thermal model for electrical machines of TEFC design," *IEE Proceedings B Electric Power Applications*, vol. 138, no. 5, p. 205, 1991. [Online]. Available: https://doi.org/10.1049%2Fip-b.1991.0025.

[14] P. H. Mellor and D. R. Turner, "Real Time Prediction of Temperatures in an Induction Motor Using a Microprocessor," *Electric Machines & Power Systems*, vol. 15, no. 4-5, pp. 333–352, 1988. [Online]. Available: https://doi.org/10.1080/07313568808909342.

[15] A. Boglietti, A. Cavagnino, M. Lazzari, and A. Pastorelli, "A simplified thermal model for variable speed self cooled industrial induction motor," in *Conference Record of the 2002 IEEE Industry Applications Conference. 37th IAS Annual Meeting (Cat. No.02CH37344)*, vol. 2, 2002, 723–730 vol.2.

[16] D. Staton, A. Boglietti, and A. Cavagnino, "Solving the more difficult aspects of electric motor thermal analysis in small and medium size industrial induction motors," *IEEE Transactions on Energy Conversion*, vol. 20, no. 3, pp. 620–628, 2005.

[17] E. Schubert, "Heat transfer coefficient at end winding and bearing covers of enclosed asynchronous machines," *Elektrie*, vol. 22, 1968.

[18] Y. Zhu, M. Xiao, K. Lu, Z. Wu, and B. Tao, "A Simplified Thermal Model and Online Temperature Estimation Method of Permanent Magnet Synchronous Motors," *Applied Sciences*, vol. 9, no. 15, 2019, ISSN: 2076-3417. [Online]. Available: https://www.mdpi.com/2076-3417/9/15/3158.

[19] T. Huber, W. Peters, and J. Böcker, "A low-order thermal model for monitoring critical temperatures in permanent magnet synchronous motors," in *7th IET International Conference on Power Electronics, Machines and Drives (PEMD 2014)*, 2014, pp. 1–6.

[20] T. Huber, W. Peters, and J. Böcker, "Monitoring critical temperatures in permanent magnet synchronous motors using low-order thermal models," in *2014 International Power Electronics Conference (IPEC-Hiroshima 2014 - ECCE ASIA)*, 2014, pp. 1508–1515.

[21] C. Kral, A. Haumer, and S. B. Lee, "A Practical Thermal Model for the Estimation of Permanent Magnet and Stator Winding Temperatures," *IEEE Transactions on Power Electronics*, vol. 29, no. 1, pp. 455–464, 2014.

[22] A. Boglietti, E. Carpaneto, M. Cossale, A. Lucco Borlera, D. Staton, and M. Popescu, "Electrical machine first order short-time thermal transients model: Measurements and parameters evaluation," in *IECON 2014 - 40th Annual Conference of the IEEE Industrial Electronics Society*, 2014, pp. 555–561.

[23] A. Boglietti, E. Carpaneto, M. Cossale, A. Lucco Borlera, D. Staton, and M. Popescu, "Electrical machine first order short-time thermal transients model: Measurements and parameters evaluation," in *IECON 2014 - 40th Annual Conference of the IEEE Industrial Electronics Society*, 2014, pp. 555–561.

[24] F. Boseniuk and B. Ponick, "Parameterization of transient thermal models for permanent magnet synchronous machines exclusively based on measurements," in *2014 International Symposium on Power Electronics, Electrical Drives, Automation and Motion*, 2014, pp. 295–301.

[25] N. Jaljal, J.-F. Trigeol, and P. Lagonotte, "Reduced Thermal Model of an Induction Machine for Real-Time Thermal Monitoring," *IEEE Transactions on Industrial Electronics*, vol. 55, no. 10, pp. 3535–3542, 2008.

[26] G. D. Demetriades, H. Z. de la Parra, E. Andersson, and H. Olsson, "A Real-Time Thermal Model of a Permanent-Magnet Synchronous Motor," *IEEE Transactions on Power Electronics*, vol. 25, no. 2, pp. 463–474, 2010.

[27] A. Boglietti, A. Cavagnino, M. Lazzari, and A. Pastorelli, "A simplified thermal model for variable speed self cooled industrial induction motor," in *Conference Record of the 2002 IEEE Industry Applications Conference. 37th IAS Annual Meeting (Cat. No.02CH37344)*, vol. 2, 2002, 723–730 vol.2.

[28] J. Fan, C. Zhang, Z. Wang, Y. Dong, C. E. Nino, A. R. Tariq, and E. G. Strangas, "Thermal Analysis of Permanent Magnet Motor for the Electric Vehicle Application Considering Driving Duty Cycle," *IEEE Transactions on Magnetics*, vol. 46, no. 6, pp. 2493–2496, 2010.

[29] J. Nerg, M. Rilla, and J. Pyrhonen, "Thermal Analysis of Radial-Flux Electrical Machines With a High Power Density," *IEEE Transactions on Industrial Electronics*, vol. 55, no. 10, pp. 3543–3554, 2008.

[30] D. Roberts, "The application of an induction motor thermal model to motor protection and other functions," Ph.D. dissertation, Univ. Liverpool, 1986.

[31] B. Kipp, "Analytische Berechnung thermischer Vorgaenge in permanentmagneterregten Synchronmachinen," Ph.D. dissertation, Helmut Schmidt Universitaet Universitaet der Bundeswehr Hamburg, 2008.

[32] C. Sciascera, P. Giangrande, L. Papini, C. Gerada, and M. Galea, "Analytical Thermal Model for Fast Stator Winding Temperature Prediction," *IEEE Transactions on Industrial Electronics*, vol. 64, no. 8, pp. 6116–6126, 2017.

[33] S. Nategh, O. Wallmark, M. Leksell, and S. Zhao, "Thermal Analysis of a PMaSRM Using Partial FEA and Lumped Parameter Modeling," *IEEE Transactions on Energy Conversion*, vol. 27, no. 2, pp. 477–488, 2012.

[34] S. Nategh, Z. Huang, A. Krings, O. Wallmark, and M. Leksell, "Thermal Modeling of Directly Cooled Electric Machines Using Lumped Parameter and Limited CFD Analysis," *IEEE Transactions on Energy Conversion*, vol. 28, no. 4, pp. 979–990, 2013.

[35] D. Kuehbacher, A. Kelleter, and D. Gerling, "An improved approach for transient thermal modeling using lumped parameter networks," in *2013 International Electric Machines and Drives Conference*, 2013, pp. 824–831.

[36] F. Qi, A. Stippich, M. Guettler, M. Neubert, and R. W. De Doncker, "Methodical considerations for setting up space-resolved lumped-parameter thermal models for electrical machines," in *2014 17th International Conference on Electrical Machines and Systems (ICEMS)*, 2014, pp. 651–657.

[37] F. Qi, "Online Model-predictive Thermal Management of Inverter-fed Electrical Machines," Ph.D. dissertation, RWTH Aachen University, 2019.

[38] P.-O. Gronwald and T. A. Kern, "Traction Motor Cooling Systems: A Literature Review and Comparative Study," *IEEE Transactions on Transportation Electrification*, vol. 7, no. 4, pp. 2892–2913, 2021.

[39] S. Oechslen, *Thermische Modellierung elektrischer Hochleistungsantriebe*. Springer Vieweg, 2018, ISBN: 978-3-658-22631-2.

[40] F. Hoffmann, "Thermische Modellierung permanentmagneterregter Synchronmaschinen mit wellenseitiger oel-Spruehkuehlung," Ph.D. dissertation, Karlsruhe Institut of Technology, 2024.

[41] L. Zhou, J. Wang, L. Wang, S. Yuan, L. Huang, D. Wang, and L. Guo, "A Method for Hot-Spot Temperature Prediction and Thermal Capacity Estimation for Traction Transformers in High-Speed Railway Based on Genetic Programming," *IEEE Transactions on Transportation Electrification*, vol. 5, no. 4, pp. 1319–1328, 2019.

[42] D. Liang, Z. Zhu, Y. Zhang, J. Feng, S. Guo, Y. Li, J. Wu, and A. Zhao, "Combined Lumped-Parameter and Simplified 2-D Analytical Thermal Model of Totally Enclosed Water Cooled PM Machine," in *2019 22nd International Conference on Electrical Machines and Systems ICEMS*, 2019, pp. 1–6.

[43] Newtwen. "A New Paradigm in Digital Twin Technology." (2024), [Online]. Available: `https://www.newtwen.com/technology` (visited on 09/17/2024).

[44] M. Schumann, S. Ebersberger, and K. Graichen, "Improved Nonlinear Estimation in Thermal Networks Using Machine Learning," in *2023 IEEE International Conference on Mechatronics ICM*, 2023, pp. 1–6.

[45] P. N. Phuc, D. Bozalakov, H. Vansompel, K. Stockman, and G. Crevecoeur, "Rotor Temperature Virtual Sensing for Induction Machines Using a Lumped-Parameter Thermal Network and Dual Kalman Filtering," *IEEE Transactions on Energy Conversion*, vol. 36, no. 3, pp. 1688–1699, 2021.

[46] M. Märgner and W. Hackmann, "Control challenges of an externally excited synchronous machine in an automotive traction drive application," in *2010 Emobility - Electrical Power Train*, 2010, pp. 1–6.

[47] "IEEE Guide for the Presentation of Thermal Limit Curves for Squirrel Cage Induction Machines," *IEEE Std 620-2022 (Revision of IEEE Std 620-1996)*, pp. 1–21, 2022.

[48] P. Zhang, B. Lu, and T. G. Habetler, "Active stator winding thermal protection for AC motors," in *Conference Record of 2009 Annual Pulp and Paper Industry Technical Conference*, 2009, pp. 11–19.

[49] F. Qi, A. Stippich, S. Koschik, and R. W. De Doncker, "Model predictive overload control of induction motors," in *2015 IEEE International Electric Machines and Drives Conference*, 2015, pp. 999–1005.

[50] J. Lemmens, P. Vanassche, and J. Driesen, "Optimal Control of Traction Motor Drives Under Electrothermal Constraints," *IEEE Journal of Emerging and Selected Topics in Power Electronics*, vol. 2, no. 2, pp. 249–263, 2014.

[51] O. Wallscheid and J. Böcker, "Derating of automotive drive systems using model predictive control," in *2017 IEEE International Symposium on Predictive Control of Electrical Drives and Power Electronics (PRECEDE)*, 2017, pp. 31–36.

[52] A. Boglietti, A. Cavagnino, D. Staton, M. Shanel, M. Mueller, and C. Mejuto, "Evolution and Modern Approaches for Thermal Analysis of Electrical Machines," *IEEE Transactions on Industrial Electronics*, vol. 56, no. 3, pp. 871–882, 2009.

[53] P. von Boeckh and T. Wetzel, *Waermeuebertragung Grundlage und Praxis*. Springer Vieweg, 2013.

[54] A. Boglietti, A. Cavagnino, M. Parvis, and A. Vallan, "Evaluation of radiation thermal resistances in industrial motors," *IEEE Transactions on Industry Applications*, vol. 42, no. 3, pp. 688–693, 2006.

[55] J. Pyrhoenen, T. Jokinen, and V. Hrabovcova, *Design of rotating electrical machines*. Wiley, 2014.

[56] L. STOYANOV, V. LAZAROV, Z. ZARKOV, and E. POPOV, "Influence of Skin Effect on Stator Windings Resistance of AC Machines for Electric Drives," in *2019 16th Conference on Electrical Machines, Drives and Power Systems (ELMA)*, 2019, pp. 1–6.

[57] J. Biela, *Wirbelstromverluste in Wicklungen induktiver Bauelemente*. ETH Library, 2011.

[58] J. Juergens, B. Ponick, O. Winter, and A. Fricassè, "Influences of iron loss coefficients estimation on the prediction of iron losses for variable speed motors," in *2015 IEEE International Electric Machines and Drives Conference (IEMDC)*, 2015, pp. 1254–1259.

[59] SKF. "Friction." (2024), [Online]. Available: `https://www.skf.com/group/products/plain-bearings/spherical-plain-bearings-rod-ends/principles/friction` (visited on 05/12/2024).

[60] J. Saari, *Thermal Modelling of High-Speed Induction Machines* (Electrical Engineering Series No. 82). Acta Polytechnica Scandinavica, 1995.

[61] F. Hoffmann and M. Doppelbauer, "Determination of Speed-Dependent Thermal Resistance of Ball Bearings," in *Elektromechanische Antriebssysteme 2023; 9. Fachtagung (VDE OVE)*, 2023, pp. 243–249.

[62] F. Qi, M. Schenk, and R. W. De Doncker, "Discussing details of lumped parameter thermal modeling in electrical machines," in *7th IET International Conference on Power Electronics, Machines and Drives (PEMD 2014)*, 2014, pp. 1–6.

[63] N. Simpson, R. Wrobel, and P. H. Mellor, "Estimation of Equivalent Thermal Parameters of Impregnated Electrical Windings," *IEEE Transactions on Industry Applications*, vol. 49, no. 6, pp. 2505–2515, 2013.

[64] D. Liang, Z. Zhu, J. Feng, S. Guo, Y. Li, J. Wu, and A. Zhao, "Influence of Critical Parameters in Lumped-Parameter Thermal Models for Electrical Machines," in *2019 22nd International Conference on Electrical Machines and Systems (ICEMS)*, 2019, pp. 1–6.

[65] G. Kylander, "Thermal modelling of small cage induction motors," Ph.D. dissertation, Chalmers Univ. Technology, 1995.

[66] I. S. Bjorklund and W. M. Kays, "Heat Transfer Between Concentric Rotating Cylinders," *Journal of Heat Transfer*, vol. 81, no. 3, pp. 175–183, Aug. 1959.

[67] K. M. Becker and J. Kaye, "Measurements of Diabatic Flow in an Annulus With an Inner Rotating Cylinder," *Journal of Heat Transfer*, vol. 84, no. 2, pp. 97–104, May 1962.

[68] K. M. Becker and J. Kaye, "The Influence of a Radial Temperature Gradient on the Instability of Fluid Flow in an Annulus With an Inner Rotating Cylinder," *Journal of Heat Transfer*, vol. 84, no. 2, pp. 106–110, May 1962.

[69] G. E. Luke, "The Cooling of Electric Machines," *Transactions of the American Institute of Electrical Engineers*, vol. XLII, pp. 636–652, 1923.

[70] OMEGA. "Thermoelement." (2024), [Online]. Available: `https://www.omega.de/prodinfo/thermoelemente.html`.

[71] D. P. F. Moeller, "Parameter identification of dynamic systems," in *Mathematical and Computational Modeling and Simulation: Fundamentals and Case Studies*. Berlin, Heidelberg: Springer Berlin Heidelberg, 2004, pp. 257–310. [Online]. Available: `https://doi.org/10.1007/978-3-642-18709-4_5`.

[72] K. Godfrey, "Identification of parametric models from experimental data," *IEEE Transactions on Automatic Control*, vol. 44, no. 12, pp. 2321–2322, 1999.

[73] O. Sename, P. Gaspar, and J. Bokor, *Robost Control and Linear Parameter Varying Approaches-Application to Vehicle Dynamics*. Springer-Verlag, Berlin Heidelberg, 2013.

[74] R. Toth, "Modeling and Identification of Linear Parameter-Varying Systems," Ph.D. dissertation, University Delft, 2008.

[75] F. Casella and M. Lovera, "LPV/LFT modelling and identification: overview, synergies and a case study," in *2008 IEEE International Conference on Computer-Aided Control Systems*, 2008, pp. 852–857.

[76] D. A. Howey, P. R. N. Childs, and A. S. Holmes, "Air-Gap Convection in Rotating Electrical Machines," *IEEE Transactions on Industrial Electronics*, vol. 59, no. 3, pp. 1367–1375, 2012.

[77] J. Lunze, *Regelungstechnik 1*. Springer Vieweg, 2020, ISBN: 978-3-662-60745-9.

[78] J. Lunze, *Regelungstechnik 2*. Springer Vieweg, 2020, ISBN: 978-3-662-60759-6.

[79] Mathworks. “Tuning Kalman Filter to Improve State Estimation.” (2024), [Online]. Available: https://de.mathworks.com/help/fusion/ug/tuning-kalman-filter-to-improve-state-estimation.html (visited on 12/30/2024).

[80] A. Becker, *Kalman Filter from de ground up*. Alex Becker, 2023, ISBN: 9789659312009. [Online]. Available: https://books.google.de/books?id=QfCo0AEACAAJ.

[81] J. Hoffman and S. Frankel, *Numerical Methods for Engineers and Scientists*. CRC Press, 2018, ISBN: 9781482270600. [Online]. Available: https://books.google.de/books?id=F5K3DwAAQBAJ.

[82] J. C. Butcher, “The Numerical Analysis of Ordinary Differential Equations. Runge-Kutta and General Linear Methods,” *Wiley-Interscience publication*, 1987.

[83] R. Marchthaler and S. Dingler, *Kalman-Filter Einfuehrung in die Zustandsschaetzung und ihre Anwendung für eingebettete Systeme*. Springer Vieweg, 2024, ISBN: 978-3-658-43216-4.

[84] R. E. Kalman, “A new approach to linear filtering and prediction problems,” 1960.

[85] K. Liu, Q. Zhang, J. Chen, Z. Q. Zhu, and J. Zhang, “Online Multiparameter Estimation of Nonsalient-Pole PM Synchronous Machines With Temperature Variation Tracking,” *IEEE Transactions on Industrial Electronics*, vol. 58, no. 5, pp. 1776–1788, 2011.

[86] K. Liu and Z. Q. Zhu, “Position-Offset-Based Parameter Estimation Using the Adaline NN for Condition Monitoring of Permanent-Magnet Synchronous Machines,” *IEEE Transactions on Industrial Electronics*, vol. 62, no. 4, pp. 2372–2383, 2015.

[87] D. Reigosa, D. Fernández, M. Martínez, J. M. Guerrero, A. B. Diez, and F. Briz, “Magnet Temperature Estimation in Permanent Magnet Synchronous Machines Using the High Frequency Inductance,” in *2018 IEEE Energy Conversion Congress and Exposition (ECCE)*, 2018, pp. 5029–5034.

[88] M. Martinez, D. Reigosa, D. Fernández, J. M. Guerrero, and F. Briz, “Enhancement of Permanent-Magnet Synchronous Machines Torque Estimation Using Pulsating High-Frequency Current Injection,” *IEEE Transactions on Industry Applications*, vol. 56, no. 1, pp. 358–366, 2020.

[89] K. Liu and Z. Q. Zhu, "Position Offset-Based Parameter Estimation for Permanent Magnet Synchronous Machines Under Variable Speed Control," *IEEE Transactions on Power Electronics*, vol. 30, no. 6, pp. 3438–3446, 2015.

[90] Z. Q. Zhu, D. Liang, and K. Liu, "Online Parameter Estimation for Permanent Magnet Synchronous Machines: An Overview," *IEEE Access*, vol. 9, pp. 59 059–59 084, 2021.

[91] R. Saheba, M. Rotea, O. Wasynczuk, S. Pekarek, and B. Jordan, "Virtual Thermal Sensing for Electric Machines," *IEEE Control Systems Magazine*, no. 42-56, 2010.

[92] O. Wallscheid and J. Böcker, "Fusion of direct and indirect temperature estimation techniques for permanent magnet synchronous motors," in *2017 IEEE International Electric Machines and Drives Conference (IEMDC)*, 2017, pp. 1–8.

[93] A. Specht, O. Wallscheid, and J. Böcker, "Determination of rotor temperature for an interior permanent magnet synchronous machine using a precise flux observer," in *2014 International Power Electronics Conference (IPEC-Hiroshima 2014 - ECCE ASIA)*, 2014, pp. 1501–1507.

[94] O. Wallscheid, A. Specht, and J. Böcker, "Observing the Permanent-Magnet Temperature of Synchronous Motors Based on Electrical Fundamental Wave Model Quantities," *IEEE Transactions on Industrial Electronics*, vol. 64, no. 5, pp. 3921–3929, 2017.

[95] A. Specht and J. Böcker, "Observer for the rotor temperature of IPMSM," in *Proceedings of 14th International Power Electronics and Motion Control Conference EPE-PEMC 2010*, 2010, T4-12-T4–15.

[96] A. Specht, S. Ober-Bl öbaum, O. Wallscheid, C. Romaus, and J. Böcker, "Discrete-time model of an IPMSM based on variational integrators," in *2013 International Electric Machines and Drives Conference*, 2013, pp. 1411–1417.

[97] D. Schroeder and J. Boecker, *Elektrische Antrieb - Regelung von Antirebssystem*. Springer Vieweg, 2020, ISBN: 978-3-662-62699-3.

[98] dewetron. "The DQ analysis for rotary field machines." (2022), [Online]. Available: `https://www.dewetron.com/2022/10/the-dq-analysis-for-rotary-field-machines-whitepaper/` (visited on 09/03/2024).

[99] Q. K. Nguyen, M. Petrich, and J. Roth-Stielow, "Implementation of the MTPA and MTPV control with online parameter identification for a high speed IPMSM used as traction drive," in *2014 International Power Electronics Conference (IPEC-Hiroshima 2014 - ECCE ASIA)*, 2014, pp. 318–323.

[100] S. Decker, M. Brodatzki, B. Bachowsky, B. Schmitz-Rode, A. Liske, M. Braun, and M. Hiller, "Predictive Trajectory Control with Online MTPA Calculation and Minimization of the Inner Torque Ripple for Permanent-Magnet Synchronous Machines," *Energies*, vol. 13, no. 20, 2020, ISSN: 1996-1073. [Online]. Available: https://www.mdpi.com/1996-1073/13/20/5327.

[101] Q. K. Nguyen, J. Schuster, and J. Roth-Stielow, "Energy optimal control of an electrically excited synchronous motor used as traction drive," in *2015 9th International Conference on Power Electronics and ECCE Asia (ICPE-ECCE Asia)*, 2015, pp. 2789–2795.

[102] Emission-test-cycles. "Supplemental Federal Test Procedure (SFTP-US 06)." (2008), [Online]. Available: https://dieselnet.com/standards/cycles/ftp_us06.php (visited on 09/09/2024).

[103] Emission-test-cycles. "Supplemental Federal Test Procedure (SFTP-US 06)." (2008), [Online]. Available: https://dieselnet.com/standards/cycles/rts95.php (visited on 04/08/2025).

[104] R. Saheba, M. Rotea, O. Wasynczuk, S. Pekarek, and B. Jordan, "Virtual Thermal Sensing for Electric Machines," *IEEE Control Systems Magazine*, vol. 30, no. 1, pp. 42–56, 2010.